

---

# Ab initio studies on photorelaxation - exploring, altering and crossing the excited state landscape

Sven Oesterling

---



München 2017



Dissertation zur Erlangung des Doktorgrades  
der Fakultät für Chemie und Pharmazie  
der Ludwig–Maximilians–Universität München

---

**Ab initio studies on photorelaxation  
- exploring, altering and crossing the  
excited state landscape**

---

**Sven Oesterling**

aus

Würzburg, Deutschland

2017

Erklärung:

Diese Dissertation wurde im Sinne von §7 der Promotionsordnung vom 28. November 2011 von Frau Prof. Dr. Regina de Vivie-Riedle betreut.

Eidesstattliche Versicherung:

Diese Dissertation wurde eigenständig und ohne unerlaubte Hilfe erarbeitet.

München, den 30.06.2017, Sven Oesterling

Dissertation eingereicht am: 27.04.2017  
1. Gutachterin: Prof. Dr. Regina de Vivie-Riedle  
2. Gutachter: Prof. Dr. Christian Ochsenfeld  
Tag der mündlichen Prüfung: 27.06.2017

# Contents

<b>Abstract</b>	<b>v</b>
<b>List of publications</b>	<b>vii</b>
<b>Introduction</b>	<b>1</b>
<b>1 Semiclassical dynamics - interfacing NewtonX and Molpro</b>	<b>3</b>
1.1 ONIOM in semiclassical dynamics on the Dewar valence isomerization . . . . .	5
1.2 Numeric CASPT2 non-adiabatic coupling for ethylene . . . . .	16
1.2.1 Theoretical and computational background . . . . .	16
1.2.2 Computational details and CASPT2 spectra . . . . .	19
1.2.3 Ethylene CASPT2 on-the-fly dynamics . . . . .	22
<b>2 Substituent effects on the excited state potential surface</b>	<b>25</b>
2.1 The FC point: Tuning the speed of hemithioindigo photoswitches . . . . .	26
2.2 Blocking the passage: Photostability of 4,4'-dihydroxythioindigo . . . . .	36
2.3 The CoIn: Relaxation dynamics of furan, furfural and $\beta$ -furfural . . . . .	41
<b>3 ASRS - passing the conical intersection</b>	<b>53</b>
<b>4 Summary and outlook</b>	<b>71</b>
<b>A NewtonX</b>	<b>73</b>
A.1 Overview of the development and capabilities of the interface . . . . .	74
A.2 Comments on the usage and the source code of the interface and NewtonX . . .	75
<b>B Formulas</b>	<b>79</b>
<b>List of abbreviations</b>	<b>81</b>
<b>Bibliography</b>	<b>83</b>
<b>Danksagung</b>	<b>87</b>



# Abstract

This work addresses relaxation mechanisms of photoexcited organic molecules of small and medium size, up to 62 atoms. For most systems it is investigated theoretically, how modifications, often in the form of substituents, influence the decay processes. The research in large parts is done in close collaboration with groups providing experimental data, which allows to formulate robust hypotheses and models.

Four systems are discussed in this context. We find the formation of the dewar lesion in deoxyribonucleic acid (DNA) to only occur, when the nucleobase is embedded in the DNA backbone, which sterically hinders accessing alternative channels. Substituting hydroxy groups at certain points of thioindigo is shown to open up an efficient deactivation channel via excited state intramolecular proton transfer, and greatly enhance the photostability of the molecule. By substituting electron donating groups to the stilbene moiety of the hemithioindigo photoswitch and correlating their effect to their Hammett parameters, the isomerization speed of hemithioindigo is optimized. And lastly, when adding an aldehyde group to furan, an additional pathway is found for its derivatives furfural and  $\beta$ -furfural. Their relaxation is slowed down regardless.

The effects on the excited state potential energy surfaces are described as general means, by which the surfaces can be influenced, and likely can be translated to other molecules as well. This eventually allows to predict properties and tailor molecules to yield desired behavior. In this context, for example for furan, furfural and  $\beta$ -furfural the structural implications of the aldehyde substituent on one conical intersection are deduced from the extended two-electron two-orbital model prior to any calculations or experiments.

Alongside the system specific investigations, an interface for the on-the-fly dynamics package NewtonX to the quantum chemistry package Molpro was programmed. Non-adiabatic semiclassical on-the-fly dynamics are a powerful tool to simulate complete relaxation processes without constraints in the dimensionality. For the interface, which in its primary setup uses complete active space self consistent field theory calculations, a number of features has been implemented. Most notably, it enables non-adiabatic dynamics on complete active space perturbation and ONIOM level of theory.





# List of publications

The thesis is based on the following five publications listed in chronological order. They are reprinted in the chapters 1 (**1**), 2 (**2-4**) and 3 (**5**).

- 1** B. P. Fingerhut, S. Oesterling, K. Haiser, K. Heil, A. Glas, W. J. Schreier, W. Zinth, T. Carell and R. de Vivie-Riedle.  
ONIOM approach for non-adiabatic on-the-fly molecular dynamics demonstrated for the backbone controlled Dewar valence isomerization.  
*J. Chem. Phys.* **136** (2012), 204307.
- 2** M. Dittmann, F. F. Graupner, B. März, S. Oesterling, R. de Vivie-Riedle, W. Zinth, M. Engelhard and W. Lüttke.  
Photostabilität von 4,4'-Dihydroxythioindigo: ein Mimetikum des Indigo.  
*Angew. Chem.* **126** (2014), 602-605.  
Photostability of 4,4'-Dihydroxythioindigo a mimetic of indigo.  
*Angew. Chem. Int. Ed.* **53** (2014), 591-594.
- 3** B. März, S. Wiedbrauk, S. Oesterling, E. Samoylova, A. Nenov, P. Mayer, R. de Vivie-Riedle, W. Zinth and H. Dube.  
Making fast photoswitches faster – using Hammett analysis to understand the limit of donor-acceptor approaches for faster hemithioindigo photoswitches.  
*Chem. Eur. J.* **19** (2014), 13984-13992.
- 4** W. Hua, S. Oesterling, J. D. Biggs, Y. Zhang, H. Ando, R. de Vivie-Riedle, B. P. Fingerhut and S. Mukamel.  
Monitoring conical intersections in the ring opening of furan by attosecond stimulated X-ray Raman spectroscopy.  
*Struct. Dyn.* **3** (2016), 023601.
- 5** S. Oesterling, O. Schalk, T. Geng, R. D. Thomas, T. Hansson and R. de Vivie-Riedle.  
Substituent effects on the relaxation dynamics of furan, furfural and  $\beta$ -furfural: a combined theoretical and experimental approach.  
*Phys. Chem. Chem. Phys.* **19** (2017), 2025-2035.

Additional publications listed in chronological order:

- 6 B. P. Fingerhut, K. Heil, E. Kaya, S. Oesterling, R. de Vivie-Riedle and T. Carell.  
Mechanism of UV-induced Dewar lesions repair catalysed by DNA (6-4) Photolyase.  
*Chem. Sci.* **3** (2012), 1794-1797.
- 7 E. Samoylova, B. März, S. Wiedbrauk, S. Oesterling, A. Nenov, H. Dube, R. de Vivie-Riedle and W. Zinth.  
Tuning of isomerization rates in indigo-based photoswitches.  
in: Ultrafast Phenomena XIX, K. Yamanouchi, S. Cundiff, R. de Vivie-Riedle, M. Kuwata-Gonokami, L. DiMauro (Eds.), *Springer Proceedings in Physics* **162** (Springer International Publishing, 2015), 391-394.

# Introduction

Many chemical and physical processes taking place around us are induced by light. Photo excited molecules can relax to the electronic ground state (GS) through different mechanisms, and which pathway a system chooses can have decisive consequences for its properties and functions. Nature is fundamentally shaped by this. One criterion for many important molecules is their photostability: The fragments of our deoxyribonucleic acid (DNA) should preferably fall back to their initial structure after excitation reliably, to avoid any damage [1, 2]. Our vision, on the contrary, is only enabled by an isomerization of retinal, which is triggered by visible light [3]. Another example are the molecules forming the light-harvesting complexes of organisms performing photosynthesis. They do not reach the GS themselves, but rather transfer the energy received to the photosynthetic reaction center, where it fuels the light-dependent reactions [4, 5]. In the same way man-made products are influenced. Dyes should not bleach [6], optical storage based on photochromic materials which can be switched between two conformeres is researched [7, 8], and a huge field, where light is used to initiate photophysical processes are solar cells [9, 10, 11]. Naturally, understanding how photorelaxation works and how it can be influenced is desirable.

Considering a single molecule which cannot transfer its energy to the surrounding, it has two basic ways to return to the GS after photoexcitation (fig. 1). Either it fluoresces or phosphoresces, which means it just falls back while emitting a photon, or it decays radiationless by following a pathway which smoothly decreases the electronic energy and passes through all states inbetween the one it is excited to, and the GS. The former is a statistical process which happens on the whole potential energy surface (PES) with a certain lifetime, dependent on the two states involved. The latter is mediated by conical intersections (CoIns) in case of two states of the same spin state, or e.g. singlet-triplet intersections for the respective states crossing. Especially in the case of CoIns, which this work focuses on, the radiationless decay can happen ultrafast and very efficient [12, 13].

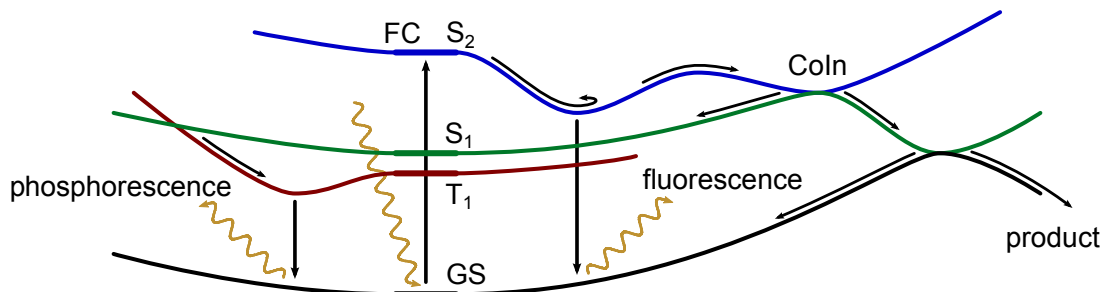


Figure 1: Sketch of a photorelaxation. From the GS minimum of the PES, the system is excited to the FC state, the  $S_2$ . From here different relaxation pathways are indicated: Radiationless decay via CoIns, fluorescence from the singlet states and phosphorescence from the triplet state.

CoIns are the  $(F - 2)$  dimensional hypersurfaces (with  $F$  being the vibrational degrees of freedom) where two adiabatic states, solutions to the electronic Schrödinger equation (eq. B.2),

degenerate. The electronic character of both states is exchanged on two opposite sides of a CoIn very abruptly. When a molecule passes a CoIn, this sudden change breaks the independence of the electronic wavefunction of the motion of the nuclei and thus the condition for the Born-Oppenheimer approximation. In the vicinity of CoIns, now looking at a whole wavepacket rather than a single molecule, population can flow between the involved states, making them the central points for the radiationless decay. For a specific radiationless relaxation pathway to be chosen, however, the mere existence of the respective CoIn is not sufficient. It has to be reachable from the FC point and no significantly better alternatives should exist. Thus, when investigating relaxation processes, the whole passage from the FC point to the GS has to be considered.

This work features three major topics around radiationless relaxation of photoexcited molecules. Firstly, it treats the interfacing of the semiclassical dynamics package NewtonX [14] and the quantum chemistry package Molpro [15]. Non-adiabatic, semiclassical on-the-fly dynamics can be used to simulate the whole relaxation process [16]. Contrary to quantum chemical calculations which mostly focus only on critical points of the PES, they inherently fulfill the requirement to investigate the whole pathway. On the other hand, because of the mere amount of calculations alone, they are much more demanding in terms of computation time, and often tradeoffs with respect to the accuracy of the quantum chemical methods used, have to be done. The our own n-layered integrated molecular orbital and molecular mechanics (ONIOM) method [17, 18], which presents one approach to describe molecules as efficient as possible, was therefor implemented. To, at the same time, meet the accuracy focused requirements of small molecules, which impose less computational restrictions, the interface of NewtonX to Molpro also enables the simulation of complete active space second-order perturbation theory (CASPT2) dynamics.

Secondly, quantum chemical and semiclassical dynamics investigations on the photorelaxation of different molecules will be presented. Here, besides the implications for the systems themselves, ranging from nucleobases forming the dewar lesion in the DNA, dyes based on thioindigo, photoswitches built from the related hemithioindigo, to the smaller molecules ethylene and furan, used as reference systems, it will be shown, how alterations at all parts of the relaxation path, the FC point, the CoIn and the region inbetween can be made, predicted, and how they can influence the relaxation process itself.

Lastly, one study focuses on the passage of a CoIn itself, how it can be experimentally observed using attosecond stimulated X-ray Raman spectroscopy (ASRS), and how the spectra of this method can be computed via semiclassical on-the-fly dynamics, to be able to interpret the experimental results.

# Chapter 1

## Semiclassical dynamics - interfacing NewtonX and Molpro

Predicting the outcome of non-reversible processes generally is challenging, as it is not sufficient to just investigate the possible outcomes and thermodynamically weight them. Evaluating the kinetics of photorelaxation processes using barrier heights of the excited state transition states is more suitable, but still provides no complete description. First of all, also the CoIns on the pathways have to be considered, oftentimes even the direction of the wave packet traversing them can influence the outcome [19]. Generally, when the relaxation is happening on an ultra-fast timescale, the vibrational energy does not necessarily spread equally over all modes and the momentum of the wavepacket has to be considered throughout the processes [20, 21, 22]. Ultimately it can be necessary to simulate the whole dynamics.

Semiclassical on-the-fly dynamics treat the movement of the nuclei classically by solving Newton's equation of motion (eq. B.1). The gradient acting on the nuclei, however, is obtained quantum mechanically by solving the Schrödinger equation for the electrons (eq. B.2). Quantum effects of the nuclei like tunneling or coherence cannot be described this way, but the big advantage compared to quantum dynamics is, that the classical treatment of the nuclei allows to simulate the dynamics of a molecule on-the-fly (fig. 1.2a). This eliminates the need to calculate the complete PES in advance, which leads to substantial constraints for quantum dynamics, where one usually is forced to limit the simulations to a few reactive coordinates. Semiclassical on-the-fly dynamics can without further drawback compute full-dimensional trajectories.

The on-the-fly dynamics package used in this work is NewtonX. It is a modular program which first of all handles the classical evolution of the nuclei using the Velocity-Verlet algorithm (eq. B.3). For the quantum chemical part a set of interfaces is provided, which operate the execution of different third party quantum chemistry packages (fig. 1.1). To emulate a wave packet as far as probabilities are concerned, when simulating the photorelaxation usually a set of trajectories is started from a Wigner distribution [23, 24] over the normal modes of the ground state (fig. 1.2b). The trajectories are set to the desired

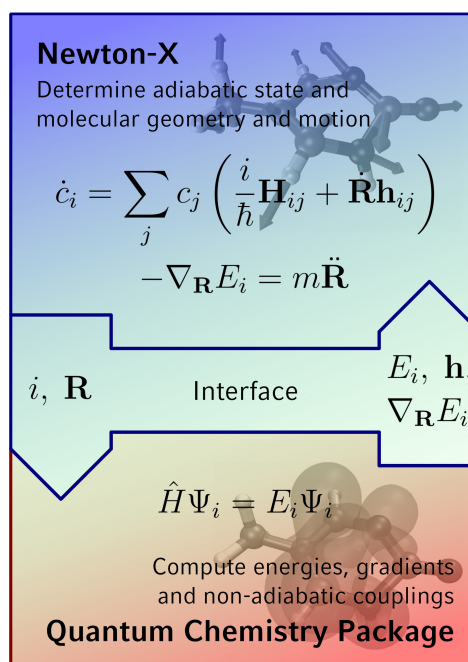


Figure 1.1: Flowchart of NewtonX. See equations 1.4, B.1 and B.2.

excited state, from where they can decay non-adiabatically to the GS via Tully's fewest switches surface hopping [25] (see chapter 1.2.1).

One part of this work has been the implementation of an interface between NewtonX and Molpro. Compared to the quantum chemistry package Gaussian [26], for which an interface is provided, Molpro offers more flexibility for its complete active space self consistent field (CASSCF) routine. A number of other methods and options have been added over time, two of the main ones, the ONIOM and CASPT2 methods are described in chapters 1.1 and 1.2. A full overview about the current functionality and status is given in appendix A. The first version of the interface, a customized version of the template provided by NewtonX, used in chapter 1.1, was adopted from Benjamin P. Fingerhut and was mostly only adjusted to the molecule. With the introduction of CASPT2 however, the code was completely rewritten, to be more universal concerning the investigated systems, as well as providing a structure which permits easier inclusion of further functionality. With the exception of chapter 1.1 all dynamics simulations in this work are based on this second version.

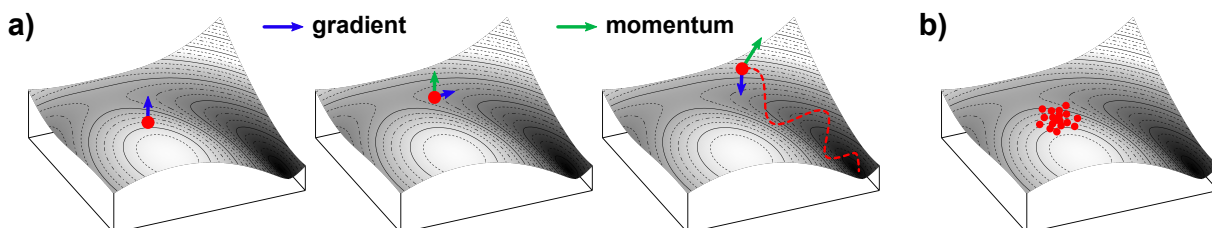


Figure 1.2: a) Schematic course of a classical particle on a PES. The gradient can be calculated in each step, on-the-fly, for the current position. b) To simulate a wavepacket and cover the spread of it, a set of trajectories with different starting conditions is generated.

## 1.1 ONIOM in semiclassical dynamics on the Dewar valence isomerization

Excited states are (for comparable systems and accuracy) much more computationally demanding than GS calculations. Especially for dynamics simulations, which need a large amount of computations to be performed, this makes the treatment of molecules of growing size challenging. Although the excitation oftentimes can be described by orbitals localized at rather small segments of a molecule, inertia and sterical and electronic influences of the complete system can seldom be neglected. Here, the ONIOM method can be used. A molecule is separated into a small fragment which is described by a high level quantum chemical method, to treat excited states, for example, and the other part which can be computed by a less demanding method. This way the whole system can be included in situations where it is impossible to use the method required for the high level region on the complete structure.

Below, non-adiabatic semiclassical on-the-fly dynamics incorporating ONIOM are presented for the formation of the Dewar photolesion in a dinucleotide. When DNA is photoexcited in the ultra violet (UV), two primary lesions can be formed in thymine-thymine and thymine-cytosine dinucleotides, the cyclobutane dimer and the (6-4)-lesion [27]. From the (6-4)-lesion, further irradiation in the visible can lead to formation of the Dewar photolesion. The formation [27], as well as the repair [28] of the the lesion have been investigated based on static calculations. In the present study the influence of the backbone on the mechanism is shown using additionally dynamics simulations.

In the following, the article “ONIOM approach for non-adiabatic on-the-fly molecular dynamics demonstrated for the backbone controlled Dewar valence isomerization”, *J. Chem. Phys.* **136** (2012), 204307, is reprinted with the permission of AIP Publishing. The supplementary information is available at [aip.scitation.org/doi/suppl/10.1063/1.4720090](http://aip.scitation.org/doi/suppl/10.1063/1.4720090). Key points of the article are:

- The integration of ONIOM into the non-adiabatic semiclassical on-the-fly dynamics method is presented.
- The dynamics of the photorelaxation of the (6-4)-lesion of a modified thymine-thymine dinucleotide were simulated on ONIOM(CASSCF:Hartree-Fock (HF)) level of theory and supported by static ONIOM(CASPT2:HF) calculations.
- A CoIn, related to the formation of the Dewar lesion, is found within the trajectories and further investigated via dynamics simulations started in its vicinity. This ultimately yields trajectories forming the Dewar lesion. The quantum yield is, in agreement with experimental observations [27], concluded to be low (< 10%).
- Comparison to the isolated pyrimidinone, which do not show the Dewar formation, demonstrates the strong impact, the DNA backbone has, on which CoIns are accessible. Inclusion of it, e.g. via the ONIOM approach, proves to be a requirement for the correct description of the process.

## ONIOM approach for non-adiabatic on-the-fly molecular dynamics demonstrated for the backbone controlled Dewar valence isomerization

Benjamin P. Fingerhut,<sup>1,a)</sup> Sven Oesterling,<sup>1</sup> Karin Haiser,<sup>2</sup> Korbinian Heil,<sup>3</sup> Andreas Glas,<sup>3</sup> Wolfgang J. Schreier,<sup>2</sup> Wolfgang Zinth,<sup>2</sup> Thomas Carell,<sup>3</sup> and Regina de Vivie-Riedle<sup>1,b)</sup>

<sup>1</sup>Department of Chemistry, Ludwig-Maximilians University Munich, Butenandtstrasse 5-13, 81377 Munich, Germany

<sup>2</sup>Faculty of Physics, Center for Integrative Protein Science Ludwig Maximilians University Munich, Oettingenstrasse 67, 80538 Munich, Germany

<sup>3</sup>Department of Chemistry, Center for Integrative Protein Science Ludwig Maximilians University Munich, Butenandtstrasse 5-13, 81377 Munich, Germany

(Received 13 December 2011; accepted 7 May 2012; published online 25 May 2012)

Non-adiabatic on-the-fly molecular dynamics (NA-O-MD) simulations require the electronic wavefunction, energy gradients, and derivative coupling vectors in every timestep. Thus, they are commonly restricted to the excited state dynamics of molecules with up to  $\approx 20$  atoms. We discuss an approximation that combines the ONIOM(QM:QM) method with NA-O-MD simulations to allow calculations for larger molecules. As a proof of principle we present the excited state dynamics of a (6-4)-lesion containing dinucleotide (63 atoms), and especially the importance to include the confinement effects of the DNA backbone. The method is able to include electron correlation on a high level of theory and offers an attractive alternative to QM:MM approaches for moderate sized systems with unknown force fields. © 2012 American Institute of Physics. [<http://dx.doi.org/10.1063/1.4720090>]

### I. INTRODUCTION

Non-adiabatic on-the-fly molecular dynamic (NA-O-MD) simulations allow to follow the ultrafast excited state dynamics of molecules in the full-dimensional coordinate space and have revealed the mechanistic details of photoreactions in conjunction with time-resolved experiments.<sup>1-4</sup> While in NA-O-MD the motion of the nuclei is treated completely classically, the electrons are treated on a quantum-mechanical level, at the expense of a quantum chemical calculation at every timestep. The non-radiative molecular relaxation of excited electronic states occurs in the vicinity of conical intersection (CoIn) seams,<sup>5-8</sup> which constitute points of degeneracy between different electronic states. Thus, to follow these CoIn mediated relaxation processes the electronic wavefunction has to comprise all relevant states in a balanced fashion. This requirement is fulfilled by the use of *multi-configuration self consistent field* (MCSCF) method or *complete active space self consistent field* (CASSCF) as one popular variant. Furthermore analytic energy gradients of ground and excited states together with derivative coupling vectors are available for MCSCF methods. These first order properties define the forces on the nuclei and the transition probability between electronic states. Additionally, the accuracy of MCSCF calculations can be systematically improved by *multi-reference configuration interaction* (MRCI) (Refs. 9 and 10) or *multi-reference second order perturbation theory* (MRPT2) (Refs. 11 and 12) which both cover the dynamic part of the electron correlation. Due to the computational expense of these high level electronic structure methods NA-

O-MD simulations are restricted to medium sized molecules typically with less than 20 atoms.

In this paper we present the integration of the ONIOM(QM:QM) (*our own N-layered integrated molecular orbital + molecular mechanics*)<sup>13,14</sup> approach into the framework of Tully's surface hopping methodology,<sup>15</sup> as a popular variant of NA-O-MD. Within the ONIOM(QM:QM) method the molecules are partitioned into layers and each layer is treated at an appropriate QM level. The essential reactive part of the molecule is treated on a higher level of theory than unreactive remote parts allowing to reduce the computational effort of the complete molecule.<sup>16</sup> Recently ONIOM(QM:MM) NA-O-MD with mechanical<sup>17</sup> and electrostatic embedding<sup>18-20</sup> allowed to get insight on the molecular level into the primary events of photodynamics of vision and the photoswitching of fluorescent proteins. In the ONIOM(QM:MM) ansatz the careful parametrization of the force fields MM part is a pre-requisite. The treatment of link atoms between the QM and MM regions requires careful consideration,<sup>21</sup> furthermore the convergence of the QM region imposes further difficulties.<sup>22</sup> The ONIOM(QM:QM) variant offers the advantage that the parametrization of non-standard force fields, like in DNA photolesions is not required and in parallel to increase the size of the QM region at a reduced computational cost compared to a high level treatment of the complete system. We make use of the advantages of the ONIOM(QM:QM) methodology and present the successful combination with NA-O-MD allowing for purely QM calculations of the primary events of localized photoreactions in complex molecules, such as photodamaged dinucleotides.

The combination of ONIOM(QM:QM) with NA-O-MD relies on strategies for efficient evaluation of excitation energies and first order properties which define the excited state

<sup>a)</sup>Current address: Department of Chemistry, University of California, Irvine, California 92697-2025, USA. Electronic mail: [bfingerh@uci.edu](mailto:bfingerh@uci.edu).

<sup>b)</sup>Electronic mail: [Regina.de\\_Vivie@cup.uni-muenchen.de](mailto:Regina.de_Vivie@cup.uni-muenchen.de).



relaxation dynamics of the complete molecule. As a proof of principle of the ONIOM NA-O-MD method we present the excited state dynamics of a (6-4)-lesion containing dinucleotide (consisting of 63 atoms) whose mechanism of Dewar valence isomerization was recently revealed in a collaborative approach.<sup>23</sup> Based on the dynamical simulations we could pinpoint the crucial role of the backbone, encompassing both nucleobases, for Dewar formation. Here, we discuss the differences in the dynamics of isolated versus confined nucleobases in detail.

The Dewar valence isomer is the stable product upon continuous irradiation with sunlight of thymine-thymine (TT) and thymine-cytosine (TC) dinucleotides, or TT/TC containing DNA strands.<sup>23–25</sup> Several deactivation mechanisms of DNA nucleobases<sup>26–28</sup> involving the barrier-free access to CoIn seams have been identified by high level quantum chemical calculations,<sup>29–41</sup> NA-O-MD,<sup>42–46</sup> *full-multiple spawning* (FMS) (Refs. 47 and 48) and direct quantum dynamical simulations.<sup>49</sup> These investigations have developed the intriguing idea of the *photostability of life*. First experiments, however, demonstrated that formation of photolesions such as the TT to CPD dimerization proceeds on a comparable ultrafast timescale.<sup>50,51</sup> Support came from mechanistic studies revealing a CoIn mediated process.<sup>52–54</sup> The presented analysis goes beyond the study of isolated DNA bases and incorporates the structural confinement. In the (6-4)-lesion it is the macrocycle of the dinucleotide. We give a microscopic interpretation for a change in reactivity, from photophysical deactivation in the isolated 5-methyl-2-pyrimidinone (5M2P) (Refs. 55 and 56) to a photochemical Dewar valence isomerization in (6-4)-lesion containing dinucleotides.<sup>23</sup> This example demonstrates the importance to include mechanical embedding effects within dinucleotides. The remainder of the paper is outlined as follows: in Sec. II we briefly summarize the concepts of NA-O-MD simulations and present the integration of the ONIOM approach into the framework of NA-O-MD. Section III presents the results of the applied ONIOM NA-O-MD to investigate the valence isomerization of the (6-4)-lesion to the Dewar lesion. Section IV aims at a comprehensive picture of the reaction mechanism. Finally the advantages, possible applications, and limitations of the presented ONIOM NA-O-MD method will be discussed.

## II. THEORY

In the following we present the integration of the ONIOM approach into the framework of NA-O-MD. The implementation relies on Tully’s surface hopping methodology<sup>15</sup> as popular variant of NA-O-MD, straightforward generalization to NA-O-MD variants where the trajectories evolve on a single potential energy surface is possible. We start by briefly summarizing the concepts of NA-O-MD simulations.

### A. Non-adiabatic on-the-fly molecular dynamics

In NA-O-MD simulations the nuclei are treated classically and follow Newton’s equation of motion. The acceleration  $\ddot{R}$  on the nuclei is defined by the gradient of the respective

populated electronic state  $i$

$$\ddot{R} = -\frac{1}{M} \frac{\partial E^{S_i}(R)}{\partial R}. \quad (1)$$

The forces on the nuclei  $\partial E^{S_i}(R)/\partial R$  are evaluated by solving the time-independent Schrödinger equation for the electrons and a subsequent gradient calculation based on the Ehrenfest theorem.<sup>15,57</sup> The time-dependent electronic population is described by the electronic expansion coefficients  $c_{kj}$ , which follow the equation of motion:

$$i\hbar\dot{c}_k = \sum_j c_j (V_{kj} - i\hbar\dot{R} \cdot d_{kj}(R)). \quad (2)$$

Changes in the electronic population are thus defined by the velocity vector  $\dot{R}$ , given by the PES gradient (see Eq. (1)) and the potential energy matrix  $V_{kj}$ . In the adiabatic representation  $V_{kj}$  is diagonal. The derivative coupling vector

$$d_{kj}(R) = \langle \Phi_k(r; R) | \frac{\partial}{\partial R} | \Phi_j(r; R) \rangle, \quad (3)$$

with  $\Phi_k(r; R)$  and  $\Phi_j(r; R)$  being the adiabatic wavefunctions of state  $k$  and  $j$ , depends parametrically on the position of the nuclei  $R$ . The transition probability can be evaluated by the scalar product  $\dot{R} \cdot d_{kj}(R)$ . A balanced description of the gradients  $\partial E^{S_i}(R)/\partial R$  and derivative coupling vectors  $d_{kj}(R)$  for several electronic states is thus the basic requirement of NA-O-MD. An excellent overview over the theoretical methods suitable for NA-O-MD simulations is given in Ref. 58.

### B. ONIOM non-adiabatic on-the-fly molecular dynamics

First we shortly highlight the advantages of the ONIOM+ (Refs. 13 and 14) approach. In an ONIOM(QM:QM) calculation the complete molecule is partitioned into layers and each layer is treated at an appropriate QM level (see Fig. 1 for the example of the (6-4)-lesion containing dinucleotide T(6-4)<sup>C</sup>T). Thus, the method is a hierarchical, but purely QM ansatz.

The ground state potential energy in a two-layer ONIOM calculation (the extension to more layers is straightforward) is obtained by an extrapolation scheme and is defined by

$$E(\text{ONIOM}) = E(\text{high, model}) + E(\text{low, real}) - E(\text{low, model}). \quad (4)$$

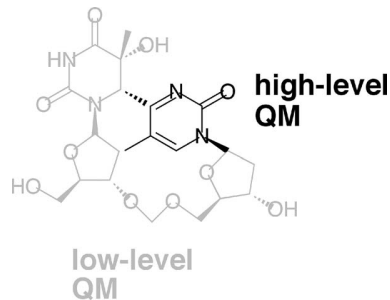


FIG. 1. QM:QM partitioning for ONIOM non-adiabatic on-the-fly molecular dynamic simulations of the (6-4)-lesion containing dinucleotide T(6-4)<sup>C</sup>T.

Here  $E(low, real)$  is the energy of the complete system on a low level of theory,  $E(low, model)$  describes the selected model system on a low, and  $E(high, model)$  on a high level of theory. Thus, the high level calculation on the complete system is avoided. Although the reproduction of absolute energy values is out of scope of the ONIOM approach, relative energy differences (e.g., excitation energies and reaction barriers) can be reliably calculated.<sup>13,59</sup>

In general ONIOM calculations can be interpreted in two different ways: the term  $E(low, real) - E(low, model)$  in Eq. (4) accounts for substituent effects on the model system. Furthermore, calculations on a low level of theory for the complete system can be improved systematically for correlation effects in the model region, reflected in the energy difference  $E(high, model) - E(low, model)$  of Eq. (4).

### 1. Electronic excited state energies with ONIOM(QM:QM)

Electronic excitation energies between different electronic excited states are calculated as relative energy differences in the ONIOM method.<sup>16,60</sup> The excitation energy  $\Delta E(ONIOM)$  of a two-layer ONIOM calculation is given by

$$\begin{aligned} \Delta E(ONIOM) &= E^{S_i}(ONIOM) - E^{S_0}(ONIOM) \\ &= \Delta E(high, model) + \Delta E(low, real) \\ &\quad - \Delta E(low, model), \end{aligned} \quad (5)$$

where  $E^{S_i}(ONIOM)$  describes the energy of the  $i$ th excited state and  $E^{S_0}(ONIOM)$  is the ONIOM energy of the electronic ground state. The rigorous calculation of  $\Delta E(ONIOM)$  thus requires three excited state calculations (e.g., ONIOM(CAS:CIS)). In the case of localized excitations within the model system  $\Delta E(ONIOM)$  can be approximated by<sup>16</sup>

$$\begin{aligned} \Delta E(ONIOM) &= E^{S_i}(ONIOM) - E^{S_0}(ONIOM) \\ &\approx \Delta E(high, model). \end{aligned} \quad (6)$$

Within this constrained low-level state (CLS) approximation only one excited state calculation on the model system is required.

### 2. First order properties: Energy gradients and derivative coupling vector

The combination of ONIOM with NA-O-MD requires the efficient implementation of first order properties defining the dynamics of the complete molecule. The respective properties are the energy gradients  $\partial E^{S_i}/\partial R$  and the derivative coupling vectors  $d_{kj}(R)$  between the considered electronic states  $k$  and  $j$ . Within the ONIOM(QM:QM) ansatz the ground state energy gradients are uniquely defined by

$$\begin{aligned} \frac{\partial E(ONIOM)}{\partial R} &= \frac{\partial E(high, model)}{\partial R} + \frac{\partial E(low, real)}{\partial R} \\ &\quad - \frac{\partial E(low, model)}{\partial R}. \end{aligned} \quad (7)$$

The high- and low-level wavefunctions are not directly coupled, thus  $\partial E(ONIOM)/\partial R$  is efficiently evaluated by the three independent terms. Again substituent and correlation effects are contained in the respective differences  $\partial E(low, real)/\partial R - \partial E(low, model)/\partial R$  and  $\partial E(high, model)/\partial R - \partial E(low, model)/\partial R$ .

Invoking the CLS approximation on the complete system allows to calculate the energy gradients of electronic excited states:

$$\begin{aligned} \frac{\partial E^{S_i}(ONIOM)}{\partial R} &\approx \frac{\partial E^{S_i}(high, model)}{\partial R} + \frac{\partial E(low, real)}{\partial R} \\ &\quad - \frac{\partial E(low, model)}{\partial R}. \end{aligned} \quad (8)$$

The excited state ONIOM gradient  $\partial E^{S_i}(ONIOM)/\partial R$  accounts for substituent effects of the complete system due to the gradient difference term  $\partial E(low, real)/\partial R - \partial E(low, model)/\partial R$ . The derivative coupling vectors (within the CLS approximation) are localized within the high level region

$$d_{kj}(ONIOM) = \langle \Phi_k(high, model) | \frac{\partial}{\partial R} | \Phi_j(high, model) \rangle. \quad (9)$$

The outlined procedure (see Fig. 2) allows to calculate all required quantities for NA-O-MD simulations on ONIOM(QM:QM) level of theory for molecules with localized excited states. Such a situation is found in many bio-molecules such as nucleosides or dinucleotides. The embedding of the high level model system within the complete molecule accounts for sterical and substituent effects by the inherent mechanical embedding scheme of the ONIOM method. An electronic embedding scheme accounting for polarization effects on the high level model by surrounding low-level point charges<sup>61,62</sup> is straightforward. The description of the non-adiabatic dynamics near conical intersections requires a multi-configuration description for several electronic states for the high-level QM part, CASSCF is a possible choice. For the low-level treatment a single determinant method, such as Hartee-Fock (HF), is sufficient to describe

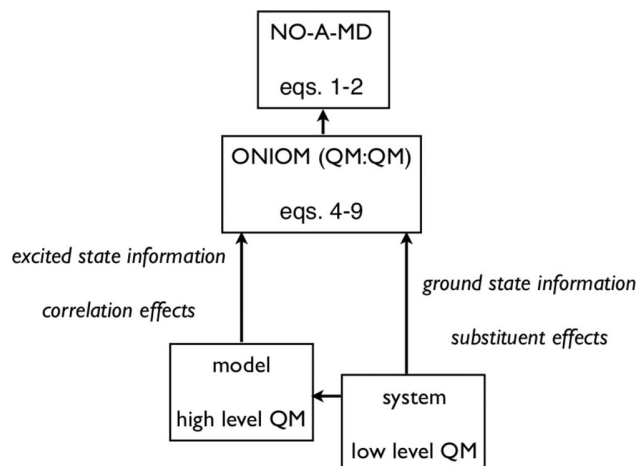


FIG. 2. ONIOM(QM:QM) partitioning for the NA-O-MD simulations.

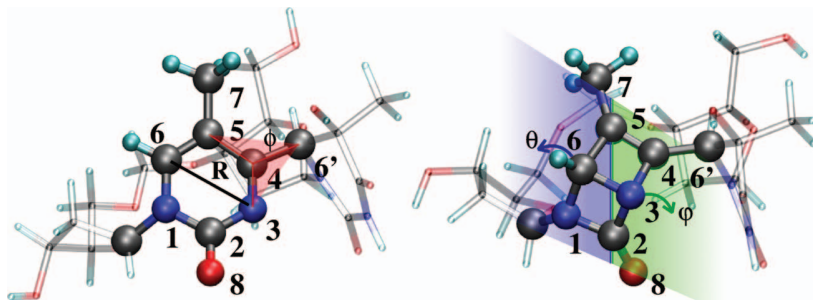


FIG. 3. Reactant (left) and product structure (right) of the (6-4)-lesion containing dinucleotide T(6-4)<sup>CT</sup>: the pyrimidinone core is treated on high level of theory (CAS(12/9)) and mechanically embedded in the complete dinucleotide. The latter one is treated on a lower level of theory (HF). As relevant coordinates in the ONIOM(QM:QM) NA-O-MD simulations the N3–C6 distance  $R$ , the hybridization angle at C4 (defined by the dihedral angle  $\phi = \angle(N3, C4, C6', C5)$  and indicated by the red tetrahedral), the out-of-plane motions of N3 (green plane), and C6 (blue plane, defined by the dihedral angles  $\varphi = \angle(C5, C2, C4, C3)$  and  $\theta = \angle(C2, C5, N1, C6)$ , respectively) emerged.

the dynamics in the complete molecule. The resulting nomenclature of the QM:QM combination is the CASSCF:HF. For the high-level QM part the same challenges arise as in other hybrid approaches. Within our approach a systematic improvement in accuracy using theoretical methods which account for dynamic electron correlation effects (e.g., QM:QM = CASPT2:MP2) is within reach. According to Fig. 2, Eqs. (4), (6), (8), and (9) are used to simulate the non-adiabatic dynamics of a (6-4)-lesion containing dinucleotide according to Eqs. (1) and (2).

### III. NON-ADIABATIC ON-THE FLY MOLECULAR DYNAMICS OF THE DEWAR VALENCE ISOMERIZATION BASED ON THE ONIOM(QM:QM) ANSATZ

The described ONIOM(QM:QM) approach for NA-O-MD simulations is ideally suited for the description of the UV-B induced Dewar valence isomerization of (6-4)-lesions. The formally  $4\pi$  electrocyclic reaction occurs localized within the pyrimidinone entity of the dinucleotide. The localized character of the excitation is extensively tested by quantum chemical calculations which rely on *multi-state multi-reference* second order perturbation theory (*MS-PT2*) (Sec. III A). Based on these investigations the dynamic description of the Dewar valence isomerization demonstrates the essential role of the DNA backbone (Secs. III B and III C).

*Computational details:* The complete system consists of a dinucleotide containing a thymine-thymine (6-4)-lesion (T(6-4)T). Instead of a phosphate bridged DNA backbone a bio-isosteric formacetal backbone is used (T(6-4)<sup>CT</sup>, 63 atoms, see Figs. 1 and 3). The modification in the DNA backbone does not affect the structure of the dinucleotide but allows to synthetically access the T(6-4)<sup>CT</sup> in substantial amounts.<sup>23,63</sup> The photochemical activity to form the Dewar valence isomer is preserved in the artificial (6-4)-lesion T(6-4)<sup>CT</sup>.

The 5M2P pyrimidinone core is the photoreactive unit in the (6-4)-lesion and thus represents the model system (see Fig. 3) which is treated on high level theory (CASSCF). All  $\pi$  orbitals as well as two lone pairs ( $n_N$ ,  $n_O$ ) are included in the active space. The resulting CAS(12/9) wavefunction (CAS( $m/n$ )) with  $m$  being the number of active electrons and

$n$  being the number of active orbitals) allows for a description of the relevant electronic states (Sec. III B), namely, the electronic ground state ( $S_0$ ), the optical accessible  $\pi\pi^*$  state, and two dark states, which correspond to excitations from the  $n_N$  and  $n_O$  lone pairs into anti-bonding  $\pi^*$  orbitals ( $n_N\pi^*$ ,  $n_O\pi^*$ ).<sup>56</sup> The simulations start in the optical bright  $\pi\pi^*$  state ( $S_3$ , see Table I) and include the four electronic states  $S_0$ ,  $\pi\pi^*$  ( $S_3$ ),  $n_N\pi^*$ , and  $n_O\pi^*$  during the dynamics. For additional stability of the electronic wavefunction the doubly excited  $\pi^*2$  state is considered, resulting in a *state average* (*sa*)-CASSCF wavefunction without symmetry restrictions with five equally weighted states (*sa5*-CAS(12/9)) for the high level QM part of the molecule. For the low-level method on the complete system we used the HF method. The ONIOM-wavefunction is thus described by ONIOM(*sa5*-CAS(12/9):HF).

The CASSCF method used for the dynamic simulations leads to an overshooting of the  $\pi\pi^*$  state in the Franck-Condon (FC) region (see Table I, Sec. III A). At the reactive CoIn the ground state and the  $n_N\pi^*$  state intersect (see Figs. 5 and 6), here the state order is properly described on ONIOM(CAS:HF) level of theory. The lack of dynamic electron correlation thus affects the initial relaxation dynamics. Due to the excess in the excitation energy the reaction dynamics speeds up, which leads to shorter excited state lifetimes than in the experiment. Further characteristic features of the excited state potential energy surfaces are reasonably well described (for a schematic of the PES highlighting regions where dynamic electron correlation effects are important, see Fig. S1 of supplementary material<sup>64</sup>) leading to a correct description of minima, conical intersection, and reaction pathways<sup>46</sup> and the relative weight of competing reaction pathways.<sup>45</sup> For all dynamic calculations we employ the 6-31G\* basis set. Basis set effects are checked with the larger *aug-cc-pvdz* basis (see Table I). In all high level calculations on the 5M2P core the free valencies of the carbon and nitrogen atom are saturated with hydrogen atoms. The bond lengths have been rescaled with a constant, atom type dependent factor as described in Ref. 61.

Quantum chemical calculations have been performed to inspect the localized nature of the excited state of the (6-4)-lesion containing dinucleotide. Here we take into account the dynamic part of the electron correlation which has been shown to be important for accurate vertical excitation

TABLE I. Vertical excitation energies (in eV) of 5M2P on *sa5*-CAS(12/9) and *MS*-PT2 level of theory. The excitation energies of T(6-4)<sup>C</sup>T are calculated on ONIOM(*sa5*-CAS(12/9):HF) and ONIOM(*MS*-PT2-CAS:HF) level of theory. Transition moments  $|\langle S_i | \mu_{x,y,z} | S_0 \rangle|^2$  are given in debye, additionally the absolute energy of the electronic ground state  $S_0$  (HF optimized geometry) is presented (in hartree). Changes in the state order are indicated with ( $S_i$ ).

Electronic state Character	$S_0$	$S_1$ $n_N \pi^*$	$S_2$ $\pi \pi^*$	$S_3$ $n_O \pi^*$	$S_4$ $\pi^* 2$
<b>Basis: 6-31G*</b>					
<i>5M2P</i>					
<i>sa5</i> -CAS(12/9)	-376.66290	4.51	4.79	5.01	6.51
<i>MS</i> -PT2- <i>sa5</i> -CAS	-377.71952	4.39 ( $S_2$ )	4.34 ( $S_1$ )	5.05	6.60
$ \langle S_i   \mu_{x,y,z}   S_0 \rangle ^2$		0.0	4.26	0.0	0.52
<i>T(6-4)<sup>C</sup>T</i>					
ONIOM( <i>sa5</i> -CAS(12/9):HF)	-1778.01310	4.56	5.74 ( $S_3$ )	4.86 ( $S_2$ )	6.69
ONIOM( <i>MS</i> -PT2- <i>sa5</i> -CAS:HF)	-1779.05028	3.95	4.48	5.02	6.18
$ \langle S_i   \mu_{x,y,z}   S_0 \rangle ^2$		0.65	3.42	0.52	0.13
<b>Basis: aug-cc-pvdz</b>					
<i>5M2P</i>					
<i>sa5</i> -CAS(12/9)	-376.71370	4.46	4.68	4.98	6.45
<i>MS</i> -PT2- <i>sa5</i> -CAS	-377.86242	4.28 ( $S_2$ )	4.16 ( $S_1$ )	4.95	6.44
$ \langle S_i   \mu_{x,y,z}   S_0 \rangle ^2$		0.0	4.46	0.0	0.39
MRCI $\sigma\pi 2$ (Refs. 55 and 56)	-377.01369	4.37	4.42	5.07	...
Expt. <sup>76</sup>			3.85		
<i>T(6-4)<sup>C</sup>T</i>					
ONIOM( <i>sa5</i> -CAS(12/9):HF)	-1778.06336	4.50	5.63 ( $S_3$ )	4.81 ( $S_2$ )	6.66
ONIOM( <i>MS</i> -PT2- <i>sa5</i> -CAS:HF)	-1779.19855	3.78	4.28	4.93	...
$ \langle S_i   \mu_{x,y,z}   S_0 \rangle ^2$		0.71	3.23	0.58	...
Expt. <sup>23</sup>			3.84		

energies in nucleobases<sup>65</sup> and 5M2P.<sup>55,56</sup> The calculations use *MS*-PT2 (Refs. 11 and 66) for the isolated 5M2P and the ONIOM approach for T(6-4)<sup>C</sup>T (ONIOM(*MS*-PT2-*sa5*-CAS:HF)). The calculations serve as a benchmark for vertical excitation energies, in all *MS*-PT2-*sa5*-CAS calculations a levelshift  $s = 0.3$  (Ref. 67) has been applied. It turns out that the close succession of electronic states (see Table I) requires a *multi-state* treatment of the dynamic electron correlation. *Single state* variants of the MRPT2 method can lead to severe artefacts, resulting in unphysical small excitation energies, as the electronic ground state and excited states are not treated in a balanced fashion. This holds for both considered molecules, 5M2P with  $C_s$  symmetry and the asymmetric T(6-4)<sup>C</sup>T.

Our ONIOM NA-O-MD simulations rely on the *NewtonX* program package,<sup>68</sup> where surface hopping between different electronic states is described by Tully's surface hopping algorithm.<sup>15</sup> For the low-level QM part we used the advantages of the GAUSSIAN 03 program package<sup>69</sup> for the ground state properties of large molecules. Excitation energies, excited state gradients, and derivative coupling vectors for the high level QM part are evaluated with the MOLPRO program package (version 2006.1).<sup>70</sup> The equations of motions of the nuclei are integrated with the Velocity-Verlet algorithm<sup>71</sup> using a timestep  $\Delta t = 0.5$  fs, within this interval a reduced timestep of  $\Delta t/20$  is used to interpolate the energy gradients and derivative coupling vectors for a continuous update of the electronic population.<sup>68,72</sup> For the integration of the electronic Schrödinger equation the 5th-order Butcher algorithm is used.<sup>73</sup> During the dynamics of the in-

dividual trajectories the derivative coupling vectors are evaluated between neighboring electronic states, the phase of the derivative coupling vector is followed to avoid phase jumps during the dynamics. The energy conservation of the trajectories is ensured by using an energy threshold of 0.5 eV for the total energy. After a hopping event between electronic states, the momentum of the nuclei is adjusted along the direction of the derivative coupling vectors to conserve the total energy.

To investigate the dynamics of the Dewar valence isomerization an uncorrelated Wigner distribution of the electronic ground state of the complete system was sampled and 74 trajectories were generated for the NA-O-MD simulations. Fifty additional trajectories were generated at the transition state (TS) towards the Dewar-valence isomerization. The TS and the  $S_1/S_0$  CoIn have been optimized with the GAUSSIAN 03 program package<sup>69</sup> on CAS level of theory. ONIOM(*sa5*-CAS(12/9):HF) optimizations of the  $S_1/S_0$  CoIn have been performed on an energy only level according the algorithm given in Ref. 74. To compare the dynamics of the isolated 5M2P with the respective dynamics of the complete dinucleotide 50 trajectories were generated by sampling the ground state equilibrium Wigner distribution.

### A. Localized excitation in the T(6-4)<sup>C</sup>T dinucleotide

Table I lists the vertical excitation energies of 5M2P and the T(6-4)<sup>C</sup>T dinucleotide on *sa5*-CAS(12/9) and ONIOM(*sa5*-CAS(12/9):HF) level of theory for two basis sets (6-31G\* and *aug-cc-pvdz*). For isolated 5M2P we find

a close succession of three electronic states within an interval of 0.5 eV. The dark state with  $n_N\pi^*$  character<sup>75</sup> is the lowest, followed by a bright  $\pi\pi^*$  and a dark  $n_O\pi^*$  state. By symmetry the  $\pi\pi^*$  state only has a transition dipole moment with the electronic ground state  $S_0$ . In the dinucleotide T(6-4)<sup>C</sup>T the symmetry preserved in 5M2P is broken by geometric deformations induced by the substituents. The energetic position of the dark states ( $n_N\pi^*$  and  $n_O\pi^*$ ) is only slightly affected, but both obtain a weak transition moment (0.52–0.65 D) with the electronic ground state. The bright  $\pi\pi^*$  is still the strongest transition with 3.42 D, however, it is energetically destabilized and now corresponds to the third excited state  $S_3$  (see Table I).

Calculations on *MS-PT2-sa5-CAS* level of theory for the isolated 5M2P show that the dynamic electron correlation substantially stabilizes the bright  $\pi\pi^*$  state by  $\approx 0.50$  eV, which becomes the first excited state. The dark  $n_N\pi^*$  and  $n_O\pi^*$  states are nearly unaffected. The calculated excitation energy is in very good agreement with the experimentally observed excitation energy of 3.85 eV.<sup>76</sup> On ONIOM(*MS-PT2-sa5-CAS:HF*) level of theory the stabilization of the  $\pi\pi^*$  state in T(6-4)<sup>C</sup>T is even more pronounced ( $\Delta\Delta E = 1.35$ – $1.26$  eV depending on the basis set), the dynamic electron correlation compensates for the destabilizing effect on ONIOM(*sa5-CAS(12/9):HF*) level of theory. The vertical excitation energy of 4.28 eV compares well to the experimental value of 3.84 eV.<sup>23</sup> The effect on the dark  $n_N\pi^*$  and  $n_O\pi^*$  states is again minor. The good agreement between the presented calculations and experiment allows to conclude that the optical bright  $\pi\pi^*$  state is a localized excited state within the pyrimidinone core of the T(6-4)<sup>C</sup>T dinucleotide. Further support for the CLS approximation is the nearly identical experimental excitation energies of the 5M2P and T(6-4)<sup>C</sup>T. Test calculations which additionally include the adjacent dihydrothymine unit of the dinucleotide (ONIOM(*sa6-CAS(16/12):HF*), for details see Table SI of supplementary material) show that the higher lying orbitals of the adjacent ring (with broken aromaticity) do not further stabilize the  $\pi\pi^*$  state nor do they mix with the dark states. The additional  $\pi$  and  $n_O$  orbitals of the adjacent ring are orthogonal with respect to the pyrimidinone core (see Fig. 3), as a result no configuration mixing is observed in the *sa6-CAS(16/12)* wavefunction. The excitation of the bright  $\pi\pi^*$  state is completely localized on the pyrimidinone chromophore.

The CLS approximation employed in the simulations neglects coulomb coupling between the high-level and the low-level method. To estimate the accuracy of this approximation we calculated the relative energy differences and excitation energies on *sa5-CAS(12/9)* level of theory for the complete T(6-4)<sup>C</sup>T dinucleotide at selected geometries of the reaction coordinate of the Dewar valence isomerization (see Table SII of supplementary material). The *sa5-CAS(12/9)* results serve as reference, as here polarization of ground and excited states are implicitly included, describing, in ONIOM notation, the coulomb coupling between the chromophore and the residue. The differences found for the *sa5-CAS(12/9)* and the ONIOM(*sa5-CAS(12/9):HF*) results give the error included in the CLS approximation. We find that the relative energy, as well as excitation energies are unaffected (within

0.1 eV) for the  $S_1$  minimum and the TS of the photoreaction which is located on  $S_0$  in close spatial and energetic vicinity to the  $S_0/S_1$  CoIn. The  $S_0/S_1$  CoIn on *sa5-CAS(12/9)* is located slightly above the TS (0.25 eV), whereas on ONIOM(*sa5-CAS(12/9):HF*) level the CoIn is nearly isoenergetic to the TS. The close energetic proximity between the TS and the  $S_0/S_1$  CoIn is preserved on both levels of theory, justifying the CLS approximation and the neglect of the coulomb coupling between the high-level and the low-level method.

Key geometric parameters are compared for the  $S_0$  minimum of T(6-4)<sup>C</sup>T and the  $S_1/S_0$ CoIn as the crucial point of the photoreaction, and the TS (Table SIII of supplementary material). The comparison shows that the bond length and angles show close agreement ( $\langle\delta\Delta_{\text{ONIOM-CAS}} = 0.024$  Å and  $0.014$  Å;  $\langle\delta\Delta_{\text{ONIOM-CAS}} = 1.0^\circ$  and  $1.2^\circ$ ) for the  $S_0$  minimum and the  $S_1/S_0$ CoIn. Especially the bond lengths at the ONIOM boundary (N1–C13 and C4–C6') are reproduced well. At the TS the deviations are somewhat larger ( $\langle\delta\Delta_{\text{ONIOM-CAS}} = 0.041$  Å and  $3.7^\circ$ ) as the N3–C6 bond length is slightly elongated (0.18 Å). The average deviation in the dihedral angles is comparable at all three critical points ( $\langle\delta\Delta_{\text{ONIOM-CAS}} = 3.1^\circ$ ,  $4.2^\circ$ , and  $4.4^\circ$ , respectively). We find that especially at the  $S_1/S_0$ CoIn as key geometry during the non-adiabatic dynamics the error in bond length angles and dihedral angles is similar to the  $S_0$  minimum which indicates that the CLS approximation remains valid over the reaction coordinate. Surprisingly the errors in T(6-4)<sup>C</sup>T are close to the reported deviations on ONIOM(CAS:HF) level of theory for previtamin D (Ref. 16) indicating the general applicability of the ONIOM approach. An elaborate study of various mechanically embedded CoIn on ONIOM(CAS:HF) compared to full CAS level of theory could be an interesting topic for future error estimates and benchmarks but is beyond the scope of the current publication.

In summary we inspected different aspects of the ONIOM(CAS:HF) approach to assure sufficient accuracy for the non-adiabatic dynamics of T(6-4)<sup>C</sup>T: (i) by high-level quantum chemical calculations the effect of the neglected dynamic electron correlation was inspected (Table 1 and Fig. S1 of supplementary material), we find that in the FC region the state ordering is affected but at the reactive  $S_1/S_0$ CoIn the correct state order is already obtained on ONIOM(CAS:HF) level of theory. (ii) Calculations which include the adjacent dihydrothymine unit (Table SI of supplementary material) show that the higher lying orbitals of the adjacent ring do not further stabilize the  $\pi\pi^*$  state and confirm the localized excitation within the pyrimidinone core. (iii) The effect of the neglected coulomb coupling due to the CLS approximation along the reaction coordinate is minor (Table SII of supplementary material). (iv) Reliable geometries can be obtained on ONIOM(CAS:HF) level of theory with high accuracy at the  $S_1/S_0$ CoIn as the crucial point of the photoreaction (Table SIII of supplementary material). (v) The closed shell method HF as low-level method gives reasonable results for the ground state energetics along the reaction coordinate compared to ROHF (Table SI of supplementary material). These results show that the ONIOM(CAS:HF) ansatz together with the applied CLS approximation is an accurate

and efficient method combination for NA-O-MD simulations on  $T(6-4)^{CT}$ .

## B. Non-radiative photophysical deactivation pathways of $T(6-4)^{CT}$

The NA-O-MD simulations start in the optical bright  $\pi\pi^*$  state ( $=S_3$ , see Table I) of the  $T(6-4)^{CT}$  and follow the ultrafast dynamics via different excited states in the full coordinate space. The mean electronic population of all 74 trajectories are shown in the supplementary material (Fig. S3). Population is transferred from  $S_3$  via  $S_2$  to  $S_1$  already in the vicinity of the FC region. The trajectories are temporarily trapped in the minimum of the  $S_1$  state leading of a temporary constant excited state population. After 250 fs several trajectories relax into the ground state. Note that due to the excess in the excitation energy on CASSCF level the reaction dynamics speeds up, which will lead to shortened excited state lifetimes, but the relative importance of the different reaction paths is adequately described.<sup>45</sup>

For a typical trajectory the non-radiative relaxation dynamics is analyzed in detail and depicted in Fig. 4. The temporal evolution of the potential energy  $E$  of the different electronic states is shown in Fig. 4 (top). The actually populated state is highlighted in magenta. Three prominent time periods can be identified. First the ultrafast  $S_3 \rightarrow S_2 \rightarrow S_1$  relaxation (in the time period of 0–50 fs), second the  $S_1$

$\rightarrow S_2 \rightarrow S_1$  population exchange (between 50 and 150 fs). Finally the dinucleotide relaxes into the  $S_0$  state. All hopping events occur in the vicinity of conical intersections. The conical intersection  $S_1/S_0$  crucial for the photoreaction is reached at 207 fs (highlighted by the dashed vertical line).

Additionally we follow the motions in the coordinates  $R$ ,  $\phi$ ,  $\varphi$ , and  $\theta$ .  $R$  (Fig. 4, red line in bottom panel) describes the N3–C6 distance crucial for the Dewar formation and is closely related to the angles  $\varphi$  and  $\theta$  (Fig. 4, green and blue lines in middle), which describe the out of plane deformation of the 5M2P pyrimidinone core.  $\phi$  is the hybridization angle at C4 (Fig. 4, red line in middle panel) and relevant to reach the lowest energy CoIn in the isolated 5M2P.<sup>55,56</sup> All four coordinates are defined in Fig. 3. The initial  $S_3 \rightarrow S_2 \rightarrow S_1$  relaxation occurs in planar reactant like structures. In the second period the  $S_1 \rightarrow S_2 \rightarrow S_1$  population exchange induces an out-of-plane deformation within the 5M2P pyrimidinone core. The N3 atom ( $\varphi$  coordinate) and the C6 atom ( $\theta$  coordinate) move in phase and are displaced out of the pyrimidinone plane, finally reducing the N3–C6 distance  $R$  (bottom). Contrarily to the isolated 5M2P (Refs. 55 and 56) the combination of the out-of-plane motions leads to a minimum-energy  $S_1/S_0$  CoIn. The hybridization angle  $\phi$  is not involved in the relaxation of  $T(6-4)^{CT}$ , the  $sp^2$  hybridization of the C4 atom is preserved. The excited state dynamics passes a Dewar-like structure at the  $S_1/S_0$  CoIn. For the selected trajectory the N3–C6 distance  $R$  increases again on  $S_0$ . As in most of the trajectories the Dewar valence isomer is not formed and photophysical relaxation towards the reactant structure occurs.

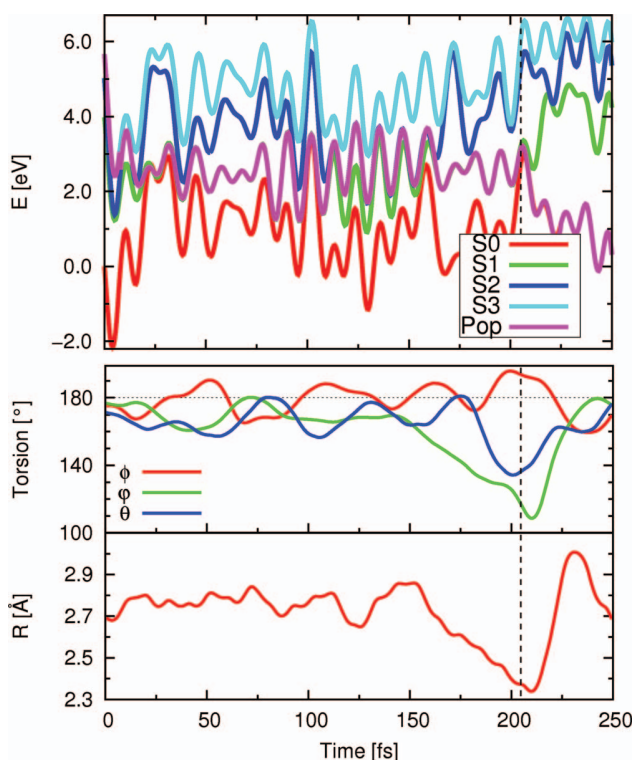


FIG. 4. ONIOM non-adiabatic on-the-fly molecular dynamics of the (6-4)-lesion containing dinucleotide  $T(6-4)^{CT}$ : the progression of the potential energy (in eV) is shown on top, a low-pass filter has been applied to separate the essential dynamics from the superimposed high-frequency C–H modes. Middle panel: time evolution of the re-hybridization coordinate at C4 ( $\phi$ , red line), and the out-of-plane deformations of the pyrimidinone core ( $\varphi$ , green line and  $\theta$ , blue line). Bottom panel: time evolution of the N3–C6 distance  $R$ .

## C. Photochemical Dewar valence isomerization of the $T(6-4)^{CT}$ dinucleotide

To improve the statistics for the branching between photophysical and photochemical pathways we sample the region near the Dewar-like  $S_1/S_0$  CoIn. This avoids the local minimum in the excited  $S_1$  state. The TS shows structural similarity to the minimum-energy conical  $S_1/S_0$  CoIn with Dewar-like bi-radical character (both optimized structures are depicted in the Fig. S4 of supplementary material). Around the TS structure 50 additional trajectories are generated by sampling the Wigner distribution. All trajectories start in the first excited  $S_1$  state and approach the  $S_1/S_0$  CoIn seam within few femtoseconds, they relax ultrafast into the electronic ground state  $S_0$ . Most trajectories (>90%) lead to the  $T(6-4)^{CT}$  reactant structure, in agreement with the typical trajectory depicted in Fig. 4. Directly after the transition through the CoIn the relevant N3–C6 distance is further shortened up to  $R_{min} \approx 2.33$  Å, however, the strong component of the  $S_0$  gradient towards the reactant slows down and reverses the N3–C6 contraction. Re-planarization of the pyrimidinone core results in photophysical deactivation.

The formation of the Dewar valence isomer is only observed in the minority of trajectories. An example of a photoreactive trajectory leading to the Dewar valence isomer is depicted in Fig. 5. The requirement is an appropriate velocity component of the N3 and C6 atom towards the Dewar valence isomer. This velocity component has to be large enough to pass a shallow potential barrier in the  $S_0$  (Fig. 5, snapshot

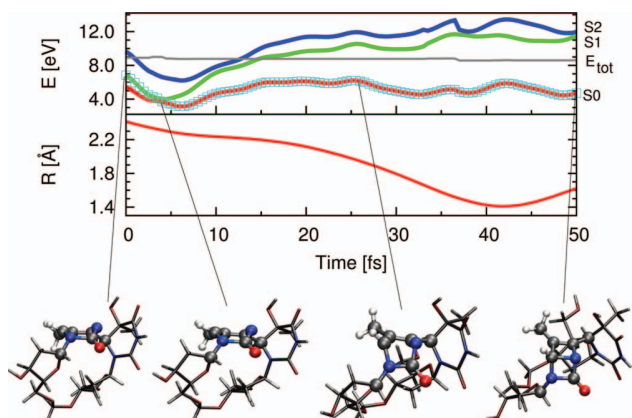


FIG. 5. ONIOM non-adiabatic on-the-fly molecular dynamics of the (6-4)-lesion containing dinucleotide T(6-4)<sup>C</sup>T started in the vicinity of the  $S_1/S_0$  conical intersection. The top panel shows the evolution of the electronic states ( $S_0$ , red;  $S_1$ , green;  $S_2$ , blue). The populated electronic state is highlighted with cyan squares. Additionally the total energy  $E_{tot}$  is depicted in light grey. Bottom panel: N3–C6 distance  $R$ .

two and three). In this case the N3–C6 distance  $R$  is reduced towards the equilibrium value  $R_{equi} = 1.48 \text{ \AA}$  of the Dewar valence isomer.

Figure 6 gives a summary of the ONIOM NA-O-MD simulation results of the Dewar valence isomerization of a (6-4)-lesion containing dinucleotide. The initially excited  $\pi\pi^*$  state ( $=S_3$ ) relaxes ultrafast and nearly quantitatively into the  $S_1$  state. The population is trapped in the  $S_1$  minimum with predominant  $n_O\pi^*$  character (and weak  $\pi\pi^*$  contributions) and geometrically characterized by butterfly distortions of the chromophore planarity. To reach the reactive  $S_1/S_0$  CoIn a  $n_O\pi^* \rightarrow n_N\pi^*$  population exchange is required which induces an out-of-plane deformation within the 5M2P pyrimidinone core and occurs in  $\approx 20\%$  of the trajectories. The ONIOM NA-O-MD calculations show that the branching at  $S_1/S_0$  CoIn between photophysical and photochemical pathways is decided by the reachability of the Dewar-like

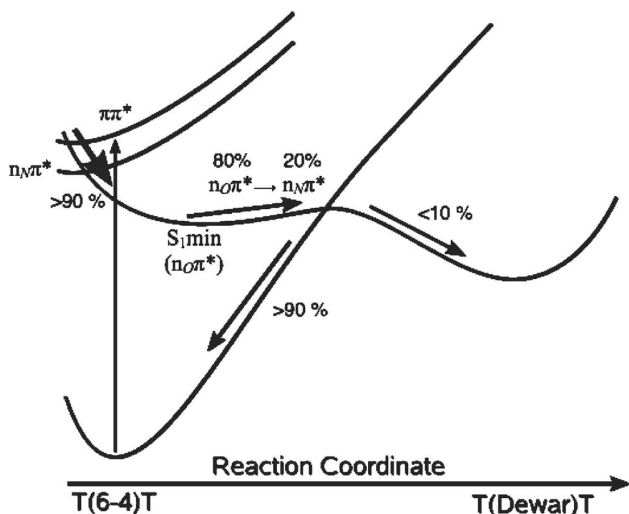


FIG. 6. Scheme summarizing the ONIOM NA-O-MD simulations on the (6-4)-lesion containing dinucleotide. Percentages refer to the consecutive branching events, which involve non-adiabatic transitions.

CoIn seam together with a subsequent ground state control. The assignment of branching ratios is not yet possible. Our simulations suggest a low quantum yield for the photochemical reaction, which is in line with the experimentally observed quantum yield of 5%–7%.<sup>23</sup>

#### IV. CONCLUSION: BACKBONE CONTROLLED REACTION MECHANISM

The final discussion aims at a comprehensive picture summarizing the results from our presented ONIOM NA-O-MD investigations, theoretical work on the isolated 5M2P (Refs. 55 and 56) and investigations on the (6-4)-linked pyrimidinone-dihydrothymidine model system.<sup>77</sup> The theoretical investigations will be set in context to the available experimental results.<sup>23,76,78</sup> We conclude with a brief discussion of the advantages, possible applications, and limitations of the presented ONIOM NA-O-MD method.

Starting with the isolated 5M2P, we observe in the FC region a remarkable close succession of three electronic states ( $n_N\pi^*$ ,  $\pi\pi^*$ ,  $n_O\pi^*$ ) within an interval of 0.5 eV. The state ordering is highly sensitive to the dynamic electron correlation. On the highest *MS-PT2* level of theory the order  $n_N\pi^* = S_1$ ,  $\pi\pi^* = S_2$  is reversed compared to the *sa5-CAS(12/9)* method. The close proximity of states leads to an elaborate  $S_3/S_2/S_1$  CoIn seam in direct vicinity of the FC point (symmetric stretch vibrations act as tuning modes and drive the system towards the CoIn seam<sup>79</sup>) which leads to an ultrafast relaxation into the  $S_1$  state. These results are in full agreement with the results of Refs. 55 and 56 who extensively investigated the CoIn seams in 5M2P by high level MRCI( $\sigma\pi^2$ ) calculations. The structural displacement found at the  $S_1/S_0$  CoIn is an out-of-plane motion of the N3 atom together with a  $sp^2 \rightarrow sp^3$  re-hybridization (highlighted in grey in Fig. 7, bottom). Together with the preserved planarity in the C5–C6–N1 unit a *sofa*-like structure is formed. These deformations are energetically and sterically possible in isolated 5M2P and have proved the recipe for photophysical deactivation. No Dewar formation is observed. The *sofa*-like structure of the  $S_1/S_0$  CoIn is also found in cytosine.<sup>48</sup> The difference in both pyrimidinones is the access to the  $S_1/S_0$  CoIn, which is barrier free in cytosine, but not in 5M2P, explaining the observed fluorescence and long excited state lifetime.<sup>76,80,81</sup>

In (6-4)-lesion containing dinucleotides and DNA strands the pyrimidinone core acts as the light absorbing chromophore and photoreactive unit. The Dewar valence isomer is formed in substantial amounts by the UV/B component of sunlight,<sup>23–25,82</sup> whereas cleavage of the DNA backbone leads to an increase of the fluorescence quantum yield.<sup>83</sup> The presented ONIOM NA-O-MD simulations show that in T(6-4)<sup>C</sup>T different  $S_1/S_0$  CoIn structures are accessible than in the isolated 5M2P (compare Fig. S2 of supplementary material, top and bottom). The dominant motion to reach the  $S_1/S_0$  CoIn seam is now an in-phase out-of-plane displacement of the N3 and C6 atoms. The resulting bi-radical Dewar-like  $S_1/S_0$  CoIn (Fig. 7, top) is similar to the TS of the valence isomerization reaction (Fig. S2 of supplementary material) and the energetic lowest solution. The reason for this significant change is the confinement within the backbone, which sterically

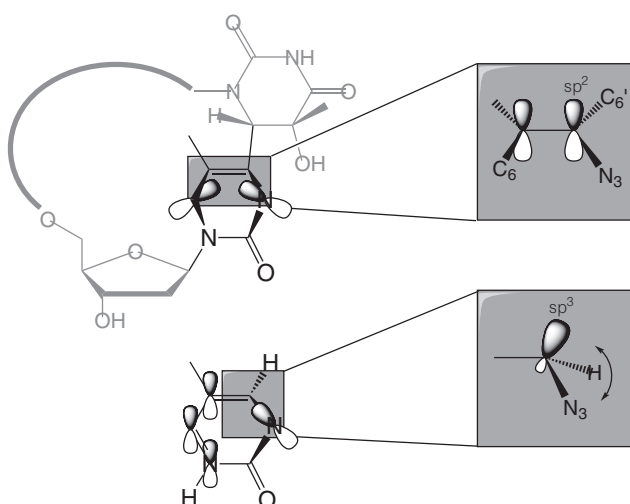


FIG. 7. Decisive hybridization scheme leading to the photochemical Dewar-valence isomerization in (6-4)-lesion containing dinucleotides and photochemical deactivation in isolated 5M2P.

hinders the  $sp^2 \rightarrow sp^3$  re-hybridization motion at C4 (highlighted in grey in Fig. 7, top). As a consequence the photochemical deactivation in T(6-4)C<sup>T</sup> towards the Dewar isomer becomes accessible. The branching between the photophysical and photochemical channels is decided on the  $S_0$  and depends on whether enough kinetic energy is deposited in the N3–C6 motion.

Though helpful to describe the relaxation process in the FC region, investigations on model systems without any DNA backbone-bridge have a limited significance. We showed the important role of the backbone to describe the essential structures and dynamics of the Dewar-valence isomerization. Experimental investigations with backbone opened dinucleotides show no Dewar formation like in isolated 5M2P.<sup>23,77</sup> Our approach allows to go beyond the non-radiative decay mechanism of single DNA bases<sup>46</sup> and incorporates the structural confinement within the complete dinucleotide. The ONIOM NA-O-MD ansatz is a computational efficient scheme, which allows to incorporate relevant structural confinements. The ONIOM(QM:QM) approach has been proven to be computationally stable in the vicinity of CoIn structures. The calculation of CoIns inherently requires a multi-configuration ansatz in the wavefunction. Although the low-level QM part does not fulfill this requirement the evaluated ONIOM energies benefit from systematic error compensation of the two performed low-level calculation ( $E(\text{low}, \text{real}) - E(\text{low}, \text{model})$ ). The essential CoIn structure is accurately described by the localized high-level calculation. A straightforward extension based on an ONIOM(CAS:CIS) combination has been proposed<sup>13,16</sup> and can be used for dynamical investigations of photochemical reactions with delocalized electronic states. The presented ONIOM(QM:QM) NA-O-MD method is very general and broadly applicable. The approach can be easily adopted for the investigations of a broad range of excited state reactions, such as the ultrafast photoreactions leading to primary DNA damage (e.g. CPD (Ref. 50) or (6-4)-lesions). The generality of the

ONIOM(QM:QM) scheme avoids the parametrization of non-standard force fields, which is required in QM/MM methods and is thus flexible to describe different kinds of photolesions. Three layer ONIOM (QM:QM:MM) schemes<sup>59</sup> together with electronic embedding additionally should allow for the embedding in the DNA double strand and to account for polarization effects.

## ACKNOWLEDGMENTS

The authors thank Professor Mike Robb for fruitful discussions. Financial support by the DFG through the Sonderforschungsbereich “Dynamics and intermediates of molecular transformations” (SFB 749) and the Cluster of Excellence “Munich Center for Advanced Photonics” (MAP) is gratefully acknowledged. The authors appreciate the Leibnitz-Rechenzentrum der Bayrischen Akademie der Wissenschaften (LRZ) for allocation of computing time.

- <sup>1</sup>C. Schrieber, M. Barbatti, K. Stock, A. J. Aquino, D. Tunega, S. Lochbrunner, E. Riedle, R. de Vivie-Riedle, and H. Lischka, *Chem. Phys.* **347**, 446 (2008).
- <sup>2</sup>M. Barbatti, A. J. A. Aquino, H. Lischka, C. Schrieber, S. Lochbrunner, and E. Riedle, *Phys. Chem. Chem. Phys.* **11**, 1406 (2009).
- <sup>3</sup>D. Polli, P. Altoè, O. Weingart, K. M. Spillane, C. Manzoni, D. Brida, G. Tomasello, G. Orlandi, P. Kukura, R. A. Mathies, M. Garavelli, and G. Cerullo, *Nature (London)* **467**, 440 (2010).
- <sup>4</sup>J. Petersen, R. Mitrić, V. Bonačić-Koutecký, J.-P. Wolf, J. Roslund, and H. Rabitz, *Phys. Rev. Lett.* **105**, 073003 (2010).
- <sup>5</sup>D. Yarkony, *J. Phys. Chem. A* **105**, 6277 (2001).
- <sup>6</sup>W. Domcke, D. R. Yarkony, and H. Köppel, in *Conical Intersections: Electronic Structure, Dynamics and Spectroscopy*, edited by W. Domcke, D. R. Yarkony, and H. Köppel (World Scientific, Singapore, 2004).
- <sup>7</sup>M. Klessinger and J. Michl, *Excited States and Photochemistry of Organic Molecules* (VCH, New York, 1995).
- <sup>8</sup>J. Michl and V. Bonačić-Koutecký, *Electronic Aspects of Organic Photochemistry* (Wiley, New York, 1990).
- <sup>9</sup>H. Lischka, M. Dallos, P. G. Szalay, D. R. Yarkony, and R. Shepard, *J. Chem. Phys.* **120**, 7322 (2004).
- <sup>10</sup>M. Dallos, H. Lischka, R. Shepard, D. R. Yarkony, and P. G. Szalay, *J. Chem. Phys.* **120**, 7330 (2004).
- <sup>11</sup>P. Celani and H.-J. Werner, *J. Chem. Phys.* **119**, 5044 (2003).
- <sup>12</sup>H. Tao, B. G. Levine, and T. J. Martínez, *J. Phys. Chem. A* **113**, 13656 (2009).
- <sup>13</sup>T. Vreven and K. Morokuma, *J. Chem. Phys.* **113**, 2969 (2000).
- <sup>14</sup>K. Morokuma, D. G. Musaev, T. Vreven, H. Basch, M. Torrent, and D. V. Khoroshun, *IBM J. Res. Dev.* **45**, 367 (2001).
- <sup>15</sup>J. C. Tully, *J. Chem. Phys.* **93**, 1061 (1990).
- <sup>16</sup>M. J. Bearpark, S. M. Larkin, and T. Vreven, *J. Phys. Chem. A* **112**, 7286 (2008).
- <sup>17</sup>S. Hayashi, E. Tajkhorshid, and K. Schulten, *Biophys. J.* **96**, 403 (2009).
- <sup>18</sup>X. Li, L. W. Chung, H. Mizuno, A. Miyawaki, and K. Morokuma, *J. Phys. Chem. Lett.* **1**, 3328 (2010).
- <sup>19</sup>O. Weingart, P. Altoè, M. Stenta, A. Bottoni, G. Orlandi, and M. Garavelli, *Phys. Chem. Chem. Phys.* **13**, 3645 (2011).
- <sup>20</sup>X. Li, L. W. Chung, and K. Morokuma, *J. Chem. Theor. Comput.* **7**, 2694 (2011).
- <sup>21</sup>H. Lin and D. Truhlar, *Theor. Chem. Acc.* **117**, 185 (2007).
- <sup>22</sup>C. V. Sumowski and C. Ochsenfeld, *J. Phys. Chem. A* **113**, 11734 (2009).
- <sup>23</sup>K. Haiser, B. P. Fingerhut, K. Heil, A. Glas, T. Herzog, B. M. Pilles, W. L. Schreiber, W. Zinth, R. de Vivie-Riedle, and T. Carell, *Angew. Chem. Int. Ed.* **51**, 408 (2012).
- <sup>24</sup>J. E. LeClerc, *Proc. Nat. Acad. Sci. U.S.A.* **88**, 9685 (1991).
- <sup>25</sup>J. Taylor, *Acc. Chem. Res.* **27**, 76 (1994); J. Taylor, D. Garrett, and M. Cohrs, *Biochemistry* **27**, 7206 (1988).
- <sup>26</sup>M. Daniels, and W. Hauswirth, *Science* **171**, 675 (1971); C. E. Crespo-Hernández, B. Cohen, P. M. Hare, and B. Kohler, *Chem. Rev.* **614**, 1977 (2004); H. Satzger, D. Townsend, M. Z. Zgierski, S. Patchkovskii, S. Ullrich, and A. Stolow, *Proc. Nat. Acad. Sci. U.S.A.* **103**, 10196 (2006).
- <sup>27</sup>T. Schultz, E. Samoylova, W. Radloff, I. V. Hertel, A. L. Sobolewski, and W. Domcke, *Science* **306**, 1765 (2004).



- <sup>28</sup>S. Matsika and P. Krause, *Ann. Rev. Phys. Chem.* **62**, 621 (2011).
- <sup>29</sup>S. Perun, A. L. Sobolewski, and W. Domcke, *J. Am. Chem. Soc.* **127**, 6257 (2005).
- <sup>30</sup>A. L. Sobolewski, W. Domcke, and C. Hättig, *Proc. Natl. Acad. Sci. U.S.A.* **102**, 17903 (2005).
- <sup>31</sup>L. Serrano-Andrés, M. Merchán, and A. C. Borin, *Chem. Eur. J.* **12**, 6559 (2006).
- <sup>32</sup>S. Yamazaki, W. Domcke, and A. L. Sobolewski, *J. Phys. Chem. A* **112**, 11965 (2008).
- <sup>33</sup>M. Merchán, L. Serrano-Andrés, M. A. Robb, and L. Blancafort, *J. Am. Chem. Soc.* **127**, 1820 (2005).
- <sup>34</sup>K. A. Kistler and S. Matsika, *J. Chem. Phys.* **128**, 215102 (2008).
- <sup>35</sup>M. Z. Zgierski, S. Patchkovskii, T. Fujiwara, and E. C. Lim, *J. Phys. Chem. A* **109**, 9384 (2005).
- <sup>36</sup>M. Z. Zgierski, S. Patchkovskii, and E. C. Lim, *J. Chem. Phys.* **123**, 081101 (2005).
- <sup>37</sup>S. Perun, A. L. Sobolewski, and W. Domcke, *J. Phys. Chem. A* **110**, 13238 (2006).
- <sup>38</sup>T. Gustavsson, A. Bányász, E. Lazzarotto, D. Markovitsi, G. Scalmani, M. J. Frisch, V. Barone, and R. Improta, *J. Am. Chem. Soc.* **128**, 607 (2006).
- <sup>39</sup>V. B. Delchev, A. Sobolewski, and W. Domcke, *Phys. Chem. Chem. Phys.* **12**, 5007 (2010).
- <sup>40</sup>M. Merchán, R. Gonzalez-Luque, T. Climent, L. Serrano-Andrés, E. Rodríguez, M. Reguero, and D. Peláez, *J. Phys. Chem. B* **110**, 26471 (2006).
- <sup>41</sup>P. Hare and C. Crespo-Hernández, *Proc. Natl. Acad. Sci. U.S.A.* **104**, 435 (2007).
- <sup>42</sup>M. Barbatti, J. J. Szymczak, A. J. A. Aquino, D. Nachtigallová, and H. Lischka, *J. Chem. Phys.* **134**, 014304 (2011).
- <sup>43</sup>D. Asturiol, B. Lasorne, M. A. Robb, and L. Blancafort, *J. Phys. Chem. A* **113**, 10211 (2009).
- <sup>44</sup>Z. Lan, E. Fabiano, and W. Thiel, *J. Phys. Chem. B* **113**, 3548 (2009).
- <sup>45</sup>J. J. Szymczak, M. Barbatti, Soo Hoo, T. Jason, J. A. Adkins, T. L. Windus, D. Nachtigallová, and H. Lischka, *J. Phys. Chem. A* **113**, 12686 (2009).
- <sup>46</sup>M. Barbatti, A. J. A. Aquino, J. J. Szymczak, D. Nachtigallová, P. Hobza, and H. Lischka, *Proc. Natl. Acad. Sci. U.S.A.* **107**, 21453 (2010).
- <sup>47</sup>H. R. Hudock, B. G. Levine, A. L. Thompson, H. Satzger, D. Townsend, N. Gador, A. Stolow, and T. J. Martínez, *J. Phys. Chem. A* **111**, 8500 (2007).
- <sup>48</sup>H. R. Hudock and T. J. Martínez, *ChemPhysChem* **9**, 2486 (2008).
- <sup>49</sup>D. Asturiol, B. Lasorne, G. A. Worth, M. A. Robb, and L. Blancafort, *Phys. Chem. Chem. Phys.* **12**, 4949 (2010).
- <sup>50</sup>W. J. Schreier, T. E. Schrader, F. O. Koller, P. Gilch, C. E. Crespo-Hernández, V. N. Swaminathan, T. Carell, W. Zinth, and B. Kohler, *Science* **315**, 625 (2007).
- <sup>51</sup>W. J. Schreier, J. Kubon, N. Regner, K. Haiser, T. E. Schrader, W. Zinth, P. Clivio, and P. Gilch, *J. Am. Chem. Soc.* **131**, 5038 (2009).
- <sup>52</sup>M. Boggio-Pasqua, G. Groenhof, L. V. Schäfer, H. Grubmüller, and M. A. Robb, *J. Am. Chem. Soc.* **129**, 10996 (2007).
- <sup>53</sup>D. Roca-Sanjuán, G. Olaso-González, I. González-Ramírez, L. Serrano-Andrés, and M. Merchán, *J. Am. Chem. Soc.* **130**, 10768 (2008).
- <sup>54</sup>C. T. Middleton, K. de La Harpe, C. Su, Y. K. Law, C. E. Crespo-Hernández, and B. Kohler, *Ann. Rev. Phys. Chem.* **60**, 217 (2009).
- <sup>55</sup>K. A. Kistler and S. Matsika, *Photochem. Photobiol.* **83**, 611 (2007).
- <sup>56</sup>K. A. Kistler and S. Matsika, *J. Phys. Chem. A* **111**, 2650 (2007).
- <sup>57</sup>A. Warshel, *Nature (London)* **260**, 679 (1976).
- <sup>58</sup>M. Barbatti, R. Shepard, and H. Lischka, "Computational and methodological elements for nonadiabatic trajectory dynamics simulations of molecules," in *Conical Intersections: Theory, Computation and Experiment*, edited by W. Domcke, D. R. Yarkony, and H. Koppel (World Scientific, Singapore, 2011), p. 415.
- <sup>59</sup>K. F. Hall, T. Vreven, M. J. Frisch, and M. J. Bearpark, *J. Mol. Biol.* **383**, 106 (2008).
- <sup>60</sup>M. J. Bearpark, F. Ogliaro, T. Vreven, M. Boggio-Pasqua, M. J. Frisch, S. M. Larkin, M. Morrison, and M. A. Robb, *J. Photochem. Photobiol. A* **190**, 207 (2007).
- <sup>61</sup>T. Vreven, K. S. Byun, I. Komáromi, S. Dapprich, J. A. Montgomery, K. Morokuma, and M. J. Frisch, *J. Chem. Theor. Comput.* **2**, 815 (2006).
- <sup>62</sup>W. Xie, L. Song, D. G. Truhlar, and J. Gao, *J. Phys. Chem. B* **112**, 14124 (2008).
- <sup>63</sup>J. Butenandt, A. P. M. Eker, and T. Carell, *Chem. Eur. J.* **4**, 642 (1998).
- <sup>64</sup>See supplementary material at <http://dx.doi.org/10.1063/1.4720090> for Figs. S1–S4 and Tables S1–S11.
- <sup>65</sup>L. Serrano-Andrés and M. Merchán, *J. Photochem. Photobiol. C* **10**, 21 (2009).
- <sup>66</sup>J. Finley, P.-A. Malmqvist, B. O. Roos, and L. Serrano-Andrés, *Chem. Phys. Lett.* **288**, 299 (1998).
- <sup>67</sup>B. O. Roos and K. Andersson, *Chem. Phys. Lett.* **245**, 215 (1995).
- <sup>68</sup>M. Barbatti, G. Granucci, M. Persico, M. Ruckebauer, M. Vazdar, M. Eckert-Maksić, and H. Lischka, *J. Photochem. Photobiol. A* **190**, 228 (2007).
- <sup>69</sup>M. J. Frisch, G. W. Trucks, H. B. Schlegel *et al.*, GAUSSIAN 03, Gaussian, Inc., Wallingford, CT, 2004, Rev D.01.
- <sup>70</sup>H.-J. Werner, P. J. Knowles, R. Lindh, F. R. Manby, M. Schätz *et al.*, MOLPRO, version 2006.1, a package of *ab initio* programs 2006, see <http://www.molpro.net>.
- <sup>71</sup>W. C. Swope, H. C. Andersen, P. H. Berens, and K. R. Wilson, *J. Chem. Phys.* **76**, 637 (1982).
- <sup>72</sup>S. Hammes-Schiffer and J. C. Tully, *J. Chem. Phys.* **101**, 4657 (1994).
- <sup>73</sup>J. C. Butcher, *J. Assoc. Comput. Mach.* **12**, 124 (1965).
- <sup>74</sup>M. J. Bearpark, M. A. Robb, and H. B. Schlegel, *Chem. Phys. Lett.* **223**, 269 (1994).
- <sup>75</sup>For the direct comparison of 5M2P and T(6-4)<sup>C</sup>T only the state character is discussed, the state symmetry present in the C<sub>s</sub> symmetric equilibrium structure of 5M2P is omitted. n<sub>N</sub>π\* correspond to states with <sup>1</sup>A'' symmetry, the ground state and ππ\* states belong to the <sup>1</sup>A' symmetry.
- <sup>76</sup>G. S. Laland and G. Serck-Hanssen, *Biochem. J.* **90**, 76 (1964).
- <sup>77</sup>Y.-J. Ai, R.-Z. Liao, S.-F. Chen, Y. Luo, and W.-H. Fang, *J. Phys. Chem. B* **114**, 14096 (2010).
- <sup>78</sup>T. Takahashi, S. Hirokami, K. Kato, M. Nagata, and T. Yamazaki, *J. Org. Chem.* **48**, 2914 (1983); T. Nishio, A. Katoh, Y. Omote, and C. Kashima, *Tetrahedron Lett.* **18**, 1543 (1978); T. Nishio, A. Kato, C. Kashima, and Y. Ome, *J. Chem. Soc., Perkin Trans. 1*, 607 (1980).
- <sup>79</sup>L. Seidner, G. Stock, A. L. Sobolewski, and W. Domcke, *J. Chem. Phys.* **96**, 5298 (1992); A. Raab, G. A. Worth, and L. S. Cederbaum, *J. Chem. Phys.* **110**, 936 (1999).
- <sup>80</sup>P. Wu and T. M. Nordlund, *Biochemistry* **29**, 6508 (1990).
- <sup>81</sup>The Dewar valence isomerization of substituted, monocyclic 5M2P derivatives (Ref. 78) is initiated by illumination in the deep UV ( $\lambda = 253$  nm), accordingly, the high energy part of the S<sub>1</sub>/S<sub>0</sub> CoIn seam (Ref. 34) with bi-radical character becomes accessible. The valence isomerization does not occur directly from the valence excited ππ\* state investigated in this study.
- <sup>82</sup>A. F. Glas, E. Kaya, S. Schneider, K. Heil, D. Fazio, M. J. Maul, and T. Carell, *J. Am. Chem. Soc.* **132**, 3254 (2010).
- <sup>83</sup>J. Blais, T. Douki, P. Vigny, and J. Cadet, *Photochem. Photobiol.* **59**, 402 (1994).

## 1.2 Numeric CASPT2 non-adiabatic coupling for ethylene

When instead of focusing on the simulation of molecules as large as possible in the previous chapter, the goal is an increased accuracy of the quantum chemical calculations, besides changing basis sets and maybe increasing the active space (AS) used in CASSCF, for static calculations one would resort to methods which are better suited to describe the dynamic electron correlation. At the equilibrium geometry and in regions where single reference methods are sufficient this could be coupled cluster methods. In cases where electronic states couple, multi reference methods like CASPT2 or multi-reference configuration interaction (MRCI) are usually the more reliable choice. For dynamics simulations MRCI will in almost all cases be too time demanding. CASPT2 could be a realistic choice for smaller molecules in this regard. Up to now, however, none of the quantum chemistry program packages known to the author has an analytical calculation of CASPT2 non-adiabatic coupling vectors implemented. When including the capability to perform non-adiabatic CASPT2 dynamics into the interface, one major part therefore was the computation of the required fraction of the non-adiabatic coupling. It was done as suggested by Tao et al. [29]. The implementation was then validated by conducting on-the-fly dynamics for ethylene.

Ethylene is likely one of the molecules studied most thoroughly. As a small molecule, it is well suited as model system to verify and test theoretical methods. Still its photochemistry comprises a long, energetically reachable seam of CoIns which can funnel population to the GS at diverse structures [30]. The two main CoIns are the pyramidalized and an ethylidene like CoIns (see figure 1.3). Furthermore, the  $\pi\pi^*$  transition of ethylene has some diffuse character, which complicates its accurate description, and rather than CASSCF, CASPT2 or other high-level methods should be used, to compute the energies of the diverse valence and Rydberg states in a balanced way [31, 32].

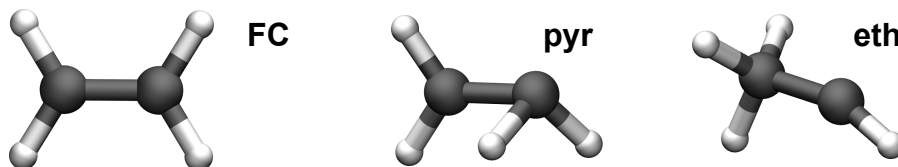


Figure 1.3: FC point, and the pyramidalized (pyr) and ethylidene like (eth) CoIn of ethylene.

### 1.2.1 Theoretical and computational background

Within the separation of the time-dependent Schrödinger equation into an electronic and a nucleic equation and the Born-Oppenheimer approximation, the total electronic wave function  $\Psi$  is split into a linear combination of the eigenfunctions of the electronic Hamilton operator. These are the wave functions  $\psi_j$  of the adiabatic states  $j$ , which are computed by standard quantum chemistry packages, and on which our semiclassical dynamics are conducted,

$$\Psi = \sum_j c_j \psi_j . \quad (1.1)$$

When a system switches its adiabatic state in the vicinity of a CoIn, the coefficients  $c_j$  of the specific adiabatic states in the total wave function change. To follow this change within the trajectories over time, one has to consider the time-dependent Schrödinger equation,

$$i\hbar \frac{\partial}{\partial t} |\Psi\rangle = \hat{H} |\Psi\rangle , \quad (1.2)$$

which, when inserting equation 1.1 multiplying from the left with  $\langle \psi_i |$  and integrating results in:

$$i\hbar \sum_j \left( \left( \frac{\partial}{\partial t} c_j \right) \langle \psi_i | \psi_j \rangle + c_j \langle \psi_i | \frac{\partial}{\partial t} \psi_j \rangle \right) = \sum_j c_j \langle \psi_i | \hat{H} | \psi_j \rangle$$

$$\sum_j \left( \frac{\partial}{\partial t} c_j \right) \langle \psi_i | \psi_j \rangle = - \sum_j c_j \left( \frac{i}{\hbar} \langle \psi_i | \hat{H} | \psi_j \rangle + \langle \psi_i | \frac{\partial}{\partial t} \psi_j \rangle \right). \quad (1.3)$$

Here, only the summand with  $j = i$  remains on the left side, as the functions  $\psi_j$  are orthonormalized. Indicating the derivative of time as a dot, and using  $\dot{\psi}_j = \mathbf{R}\nabla_{\mathbf{R}}\psi_j$  this then writes as,

$$\dot{c}_i = - \sum_j c_j \left( \frac{i}{\hbar} H_{ij} + \mathbf{R}\mathbf{h}_{ij} \right), \quad (1.4)$$

with  $H_{ij} = \langle \psi_i | \hat{H} | \psi_j \rangle$  and the non-adiabatic coupling vectors  $\mathbf{h}_{ij} = \langle \psi_i | \nabla_{\mathbf{R}} \psi_j \rangle$ . Using adiabatic states, the  $H_{ij}$  vanish for  $i \neq j$ .  $H_{ii}$  is responsible for the rotation in phase space.

One way to emulate the non-adiabatic behavior of a wavepacket in semiclassical dynamics is to run a set of trajectories in such a way that the number of trajectories in state  $i$ ,  $N_i$ , resembles the fraction of  $|\psi_i|^2$  in  $|\Psi|^2$ ,  $a_{ii}$ , in each time step. ( $N_i = a_{ii} = c_i c_i^*$ , see eq. 1.1.) This is done by Tully's fewest switches surface hopping algorithm [25] with the additional condition that the number of hops between different states in each step is minimized. This ensures that also the amount of trajectories switching states reflects the derivative of  $a_{ii}$  with respect to time, which means, trajectories switch in regions of significant coupling  $\mathbf{h}_{ij}$  between states and else stick to their respective states. Using equation 1.4,  $\dot{a}_{ii}$  is expressed as:

$$\begin{aligned} \dot{a}_{ii} &= c_i \dot{c}_i^* + \dot{c}_i c_i^* \\ &= - \sum_j c_i c_j^* \left( \frac{-i}{\hbar} H_{ij}^* + \mathbf{R}\mathbf{h}_{ij} \right) - \sum_j c_j c_i^* \left( \frac{i}{\hbar} H_{ij} + \mathbf{R}\mathbf{h}_{ij} \right) \\ &= - \sum_j \left( \frac{-i}{\hbar} (a_{ij} H_{ij}^* - a_{ij}^* H_{ij}) + (a_{ij} \mathbf{R}\mathbf{h}_{ij} + a_{ij}^* \mathbf{R}\mathbf{h}_{ij}) \right) \\ &= - \sum_{j \neq i} \left( \frac{2}{\hbar} \Im(a_{ij} H_{ij}^*) + 2\Re(a_{ij} \mathbf{R}\mathbf{h}_{ij}) \right) \\ &= \sum_{j \neq i} -2\Re(a_{ij} \mathbf{R}\mathbf{h}_{ij}) = \sum_{j \neq i} b_{ij}. \end{aligned} \quad (1.5)$$

Here the summand  $j = i$  vanishes as  $a_{ii}$  is real and because of  $h_{ii} = 0$ . Using adiabatic states, the  $H_{ij}$  elements can be left out completely this way. Equation 1.5 can be understood as separation of the total change of population of state  $i$ ,  $\dot{a}_{ii}$ , into the fractions which flow between  $i$  and all other states  $j$ ,  $b_{ij}$ . To satisfy the condition that the number of hoppings is minimized, in the trajectories only hoppings in the direction of the population flow are allowed. Thus, in the case of population flowing from state  $i$  to state  $j$ , all  $N_i$  trajectories in state  $i$  will have the probability  $P_{ij}$  to jump from  $i$  to  $j$  within a certain time window  $\Delta t$ ,

$$P_{ij} = \frac{\Delta t b_{ij}}{a_{ii}}. \quad (1.6)$$

Within the dynamics, equation 1.6 will be evaluated for all pairs of states including the occupied state in each timestep and for each individual trajectory. A random number will then decide, whether the specific trajectory hops or remains on its current PES.

The population flow between the states does not depend on the whole non-adiabatic coupling vector  $\mathbf{h}_{ij}$ , but only on its dot product with the motion vector of the molecule  $\dot{\mathbf{R}}$ . In cases where  $\mathbf{h}_{ij}$  has to be constructed numerically by finite differences, as is the case for the CASPT2 dynamics, it is sufficient, to only determine its fraction, parallel to  $\dot{\mathbf{R}}$  [29], which greatly reduces the expense of this task with growing molecular size,

$$\begin{aligned} \dot{\mathbf{R}}\mathbf{h}_{ij} = \mathbf{v}\mathbf{h}_{ij} &= \frac{\langle \psi_i(\mathbf{R}) | \psi_j(\mathbf{R} + \epsilon\mathbf{e}^v) \rangle - \langle \psi_i(\mathbf{R}) | \psi_j(\mathbf{R}) \rangle}{\epsilon} |\mathbf{v}| \\ &= \frac{\langle \psi_i(\mathbf{R}) | \psi_j(\mathbf{R} + \epsilon\mathbf{e}^v) \rangle}{\epsilon} |\mathbf{v}| = h_{ij}^v |\mathbf{v}| . \end{aligned} \quad (1.7)$$

Here  $\mathbf{e}^v$  is the unit vector in the direction of motion  $\mathbf{v}$  of the molecule, and  $\epsilon$  is a small, finite number. As NewtonX calculates the dot product  $\mathbf{v}\mathbf{h}_{ij}$  in its surface hopping routine, the value which has to be determined within the quantum chemistry part is  $h_{ij}^v$ , the magnitude of the non-adiabatic coupling vector in direction of  $\dot{\mathbf{R}} = \mathbf{v}$ . In the quantum chemistry package Molcas [33] equation 1.7 can be directly used, but for Molpro the CASPT2 wavefunctions can, to the authors knowledge, not be stored, to calculate the overlap between two different ones. Therefore further transformation and one approximation are necessary. The multi-state (MS)-CASPT2 wave function  $\psi_i^{MSPT2}$  can be written in terms of its single-state (SS) references  $\psi_i^{SSPT2}$  and the mixing coefficients  $C_i$ , which are listed in the program output:

$$\psi_i^{MSPT2} = \sum_j C_{ij} \psi_j^{SSPT2} . \quad (1.8)$$

One now wants to express the SS wavefunction at the displaced geometry  $\psi_i^{SSPT2}(\mathbf{R} + \epsilon\mathbf{e}^v)$  as a linear combination of the wavefunctions at  $\mathbf{R}$ ,  $\psi_j^{SSPT2}(\mathbf{R})$ ,

$$\psi_i^{SSPT2}(\mathbf{R} + \epsilon\mathbf{e}^v) = \sum_j U_{ij} \psi_j^{SSPT2}(\mathbf{R}) . \quad (1.9)$$

Here we assume, that the AS does not significantly change with a small  $\epsilon$ . Using  $S_{ij} = \langle \psi_i^{SSPT2}(\mathbf{R}) | \psi_j^{SSPT2}(\mathbf{R}) \rangle$  and inserting equations 1.8 and 1.9 into 1.7,  $h_{ij}^v$  is then written in matrix notation as:

$$\mathbf{h}^v = \frac{1}{\epsilon} \mathbf{C} \mathbf{R} \mathbf{S} \mathbf{U}^T \mathbf{C}_{\mathbf{R} + \epsilon\mathbf{e}^v}^T , \quad (1.10)$$

only considering the off-diagonal terms. Molpro provides a routine called DDR to calculate the transformation matrix  $\mathbf{U}$ , but only for the CASSCF states, the reference wave functions of the SS-CASPT2 states. This adds up to the approximation made with equation 1.9. It can be justified by writing the SS-CASPT2 wave function as the perturbed CASSCF wave function,  $\psi_i^{SSPT2} = k_i \psi_i^{CAS} + \psi_i^{\delta PT2}$  and inspecting

$$\begin{aligned} &\langle \psi_i^{SSPT2}(\mathbf{R}) | \psi_j^{SSPT2}(\mathbf{R} + \epsilon\mathbf{e}^v) \rangle = \\ &k_i^* k_j \langle \psi_i^{CAS}(\mathbf{R}) | \psi_j^{CAS}(\mathbf{R} + \epsilon\mathbf{e}^v) \rangle + k_i^* \langle \psi_i^{CAS}(\mathbf{R}) | \psi_j^{\delta PT2}(\mathbf{R} + \epsilon\mathbf{e}^v) \rangle + \\ &k_j \langle \psi_i^{\delta PT2}(\mathbf{R}) | \psi_j^{CAS}(\mathbf{R} + \epsilon\mathbf{e}^v) \rangle + \langle \psi_i^{\delta PT2}(\mathbf{R}) | \psi_j^{\delta PT2}(\mathbf{R} + \epsilon\mathbf{e}^v) \rangle . \end{aligned} \quad (1.11)$$

If the description of the states  $i$  and  $j$  is sound, the perturbation part of the wave function,  $\psi^{\delta PT2}$ , has to be small. For the different overlaps in equation 1.11 this means, that especially the last one between both perturbations, is very limited in size, compared to the coupling between the CASSCF wave functions. Furthermore, the perturbation should follow the diabatic

state characters of the CASSCF states and thus mix comparably to their adiabatic references. The configurations which underlie the CASSCF and the perturbation part can be considered orthogonal for a small  $\epsilon$ .<sup>a</sup> The mixed overlap terms thus vanish.

Equation 1.10 was used in early versions of the interface. The assignment of the phase information between the MS coefficient matrices  $\mathbf{C}$  at  $\mathbf{R}$  and the displaced geometry, however, proved troublesome. This is solved by

$$\langle \psi_i | \nabla_{\mathbf{R}} \psi_j \rangle = \frac{\langle \psi_i | \nabla_{\mathbf{R}} \hat{H} | \psi_j \rangle}{E_j - E_i}, \quad (1.12)$$

where  $E_i$  is the energy of state  $i$ , one receives the expression, which is finally used to calculate the non-adiabatic coupling in direction of the movement as antisymmetric matrix:

$$\mathbf{h}^v = \frac{\mathbf{C}_{\mathbf{R}} \mathbf{U}^T \mathbf{H}_{\mathbf{R}+\epsilon\mathbf{e}^v} \mathbf{U} \mathbf{C}_{\mathbf{R}}^T}{\epsilon \Delta \mathbf{E}}. \quad (1.13)$$

Here  $\mathbf{H}$  is the Hamilton matrix of the SS-CASPT2 states,  $\langle \psi^{SSPT2} | \hat{H} | \psi^{SSPT2} \rangle$ , and the transformation matrices  $\mathbf{U}$  are this time used, to transform the wave functions from  $\mathbf{R} + \epsilon\mathbf{e}^v$  back to  $\mathbf{R}$ .  $\Delta \mathbf{E}$  is the energy difference matrix, where  $\Delta E_{ij} = E_j - E_i$ . Only the off-diagonal terms are defined and used.

### 1.2.2 Computational details and CASPT2 spectra

Although ethylene was used to test the implementation of the CASPT2 non-adiabatic coupling first and foremost, because it is small, it was also well suited to test the accuracy, CASPT2 can provide with larger AS' and basis sets than the more usual focus on the  $\pi$  space together with 6-31G\*.<sup>b</sup> It is known for ethylene, that the vertical excitation energy of the  $\pi\pi^*$  state at the FC point is not located in the center of the absorption band, but shifted to the blue [36]. Therefore, to compare the results the Wigner-distribution provided by NewtonX was used to generate a complete spectrum.

For the AS a variety of setups was used. The largest MS-CASPT2 calculation was performed as a single-reference calculation with the (4,9) AS shown in fig. 1.4, considering 12 states. From here the AS was reduced to two versions to calculate the spectra with multi-reference MS-CASPT2. The first, a (2,6) AS, including orbitals 8 to 13, covers the  $\pi\pi^*$  and the four energetically lowest lying, excited Rydberg states. They are  $S_1$  to  $S_4$ ,  $S_6$  and  $S_7$  with the (4,9) AS. The second, a (4,4) AS includes orbitals 7 to 10 and was used, to not only compute excitations from the  $\pi$  orbital, the highest occupied molecular orbital (HOMO), but also from  $\sigma_{CH}$ , the HOMO-1. The respective states are not described by the (2,6) AS. The lowest excitation from the  $\sigma_{CH}$  orbital,  $\sigma_{CH}\pi^*$ , is the  $S_5$  in with the (4,9) AS.

Table 1.1 shows the computed energies of the lowest five states for the (4,4) AS and different basis sets. The number of contracted functions is provided as indicator for the size of the

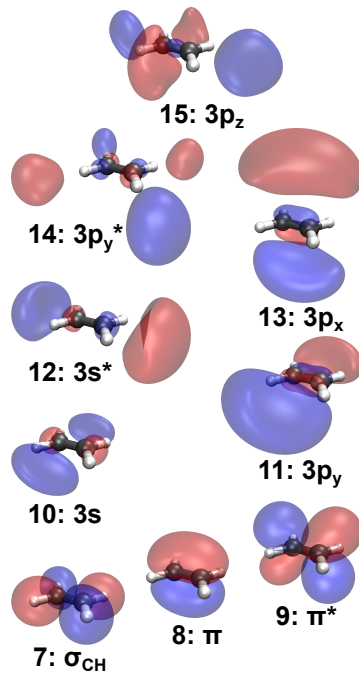


Figure 1.4: Orbitals 7 to 15 of ethylene; 8( $\pi$ ) is the HOMO.

<sup>a</sup>Depending on the implementation, the reference space is either left out of the perturbation calculation completely [34], or is only optionally included and found to only have a minor and indirect influence [35].

<sup>b</sup>The calculations were performed in 2011. Over time, the capabilities here changed considerably, of course.

Table 1.1: Absolute energies on CASSCF and excitation energies on CASPT2 level of theory for the first five states in ethylene, calculated with a (4,4) AS for different basis sets. The number of contracted functions as main indicator for the basis set size, as well as the energy differences of all basis sets to aug-cc-pVQZ are provided. (The calculations were performed with a preliminary geometry and set of options, to evaluate the basis sets.)

	basis set and number of contractions				
	6-31+G*	aug-cc-pVTZ	TZ-ANO	full ANO	aug-cc-pVQZ
	44	184	184	336	344
	<b>CASSCF energy [H] (<math>\Delta E</math> [eV])</b>				
GS	-78.041 (0.83)	-78.067 (0.11)	-78.072 (-0.03)	-78.071 ( 0.02)	-78.071 (0.00)
$\pi 3s$	-77.772 (1.65)	-77.827 (0.15)	-77.831 ( 0.04)	-77.827 ( 0.14)	-77.832 (0.00)
$\pi\pi^*$	-77.712 (1.19)	-77.748 (0.21)	-77.754 ( 0.04)	-77.745 ( 0.28)	-77.756 (0.00)
$\sigma_{CH}\pi^*$	-77.680 (0.97)	-77.713 (0.06)	-77.716 (-0.01)	-77.716 (-0.01)	-77.715 (0.00)
$\sigma_{CH}3s$	-77.645 (1.55)	-77.698 (0.11)	-77.701 ( 0.02)	-77.700 ( 0.06)	-77.702 (0.00)
	<b>CASPT2 excitation energy [eV] (<math>\Delta E</math> [eV])</b>				
$\pi\pi^*$	7.74 (0.27)	7.43 (-0.03)	7.46 ( 0.00)	7.46 (0.00)	7.46 (0.00)
$\pi 3s$	7.96 (0.35)	7.54 (-0.07)	7.57 (-0.04)	7.61 (0.01)	7.61 (0.00)
$\sigma_{CH}\pi^*$	8.90 (0.52)	8.50 ( 0.12)	8.37 (-0.01)	8.50 (0.12)	8.38 (0.00)
$\sigma_{CH}3s$	10.15 (0.56)	9.68 ( 0.09)	9.56 (-0.03)	9.78 (0.18)	9.59 (0.00)

respective basis set.<sup>c</sup> As the higher excited states in ethylene are mostly excitation to Rydberg orbitals, only basis sets with diffuse functions are included. All results are compared to the ones of the biggest basis set, aug-cc-pVQZ.

For the MS-CASPT2 excitation energies, even 6-31+G\*, the smallest basis set provides qualitatively reasonable results, especially as the  $\Delta E$  values to the aug-cc-pVQZ basis set are quite constant. Interestingly the deviation between exciting to the  $\pi^*$  orbital and the Rydberg orbital is significantly smaller, than the deviation between exciting from  $\sigma_{CH}$  and  $\pi$  (e.g. 0.27 and 0.35 eV, vs 0.27 and 0.52 eV). Between the two medium sized basis sets aug-cc-pVTZ and TZ-ANO, the latter results in energies significantly closer to the reference, never being off more than 0.04 eV. The second largest basis set, the full ANO basis, differs much more. At the time the calculations were performed, to evaluate which of the both large basis sets performs better, the absolute CASSCF energies, which are variational values, were also compared. Here the full ANO basis set yields the higher energies and thus performs worse - even compared to TZ-ANO. This was further studied<sup>d</sup>, but likely is due to a mistake by the developers [39], discovered in 2015. In the end TZ-ANO was chosen as basis set for the calculation of the spectra. The dynamics simulations which were primarily performed to test the implementation of CASPT2 into the NewtonX interface were run with 6-31G\* when only using  $\pi$  and  $\pi^*$  in a (2,2) AS. For inclusion of the 3s orbital the 6-31+G\* basis set was used for the (2,3) AS. The qualitative differences are rather small, and the smaller basis sets greatly reduce the computation time, which is crucial for the verification purposes.

Table 1.1 merely serves to help assessing the quality of the basis sets, the calculations were performed with a preliminary geometry and set of options. For the calculation of the spectra it proved important to not use the standard shift (the value used was 0.3) in the CASPT2 routine,

<sup>c</sup>Comparing the calculation speed on the same machine for aug-cc-pVTZ and TZ-ANO, which both have 184 contracted functions in ethylene, but the number of primitive Gaussians is increased by 41% from 242 to 342, respectively, the computation time is only increased by 2% for a state average (SA)8 (4,7) MS-CASPT2 calculation.

<sup>d</sup>The full ANO-RCC basis set, as taken from the EMSL basis set exchange library [37, 38], does not build upon TZ-ANO, but has many values changed slightly. When combining both basis sets, by replacing the functions of the full ANO which also appear in TZ-ANO by the latter, the result outperforms aug-cc-pVQZ in all states but S<sub>2</sub>.

but rather the ionisation energy electron affinity (IPEA) version [40] (here 0.2 was used). This for example results in the correct ordering of the  $\pi\pi^*$  and  $\pi3s$  states at the FC point, which is reversed in table 1.1. The normal modes used for the Wigner distribution for the spectra was computed on coupled cluster singles and doubles (CCSD) level of theory.

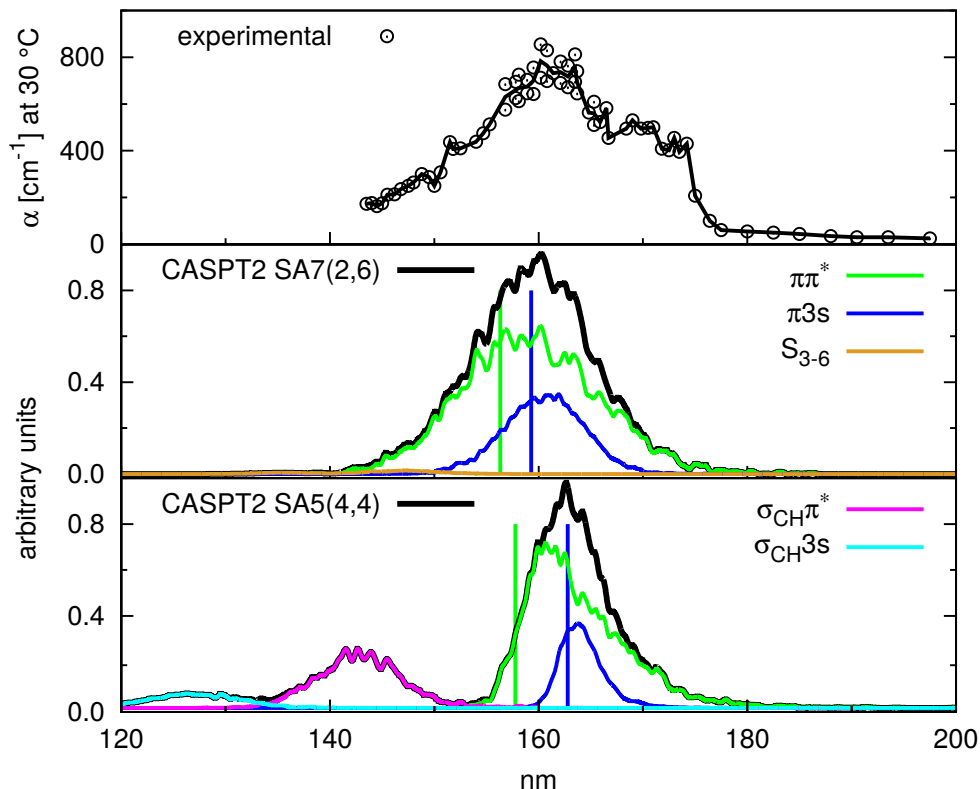


Figure 1.5: Experimental and calculated spectra of ethylene. The experimental spectrum was transferred from the work of Wilkinson et al. [41] as accurately as possible. The absorption coefficient  $\alpha$  should not be off more than  $10 \text{ cm}^{-1}$ . The theoretical spectra are plotted from the Gaussian-broadened CASPT2 excitation energies and transition dipole moments of 5000 points of a Wigner distribution. Two different CASPT2 setups were used, to either describe additional Rydberg states (orange line, CASPT2 SA7 (2,6)), or excitations from  $\sigma_{CH}$  (magenta and cyan lines, CASPT2 SA5 (4,4)). The whole spectra are plotted black and are the sum of the colored, state specific fractions. The vertical excitation energies of the  $\pi\pi^*$  and  $\pi3s$  states at the equilibrium geometry are indicated as green and blue bars.

Figure 1.5 shows the spectra calculated from 5000 points of the Wigner distribution, where each computed excitation energy is broadened by a Gaussian function and multiplied by its Einstein coefficient. Comparing the calculated spectra with the experimental spectrum [41], especially the one using the (2,6) AS resembles the experimental spectrum quite closely. Both spectra are mostly defined by the  $\pi\pi^*$  excitation (green). Looking at the excitation energies at the FC point, the  $\pi3s$  state (blue) is still off. It lies at 159 and 163 nm, but is expected at 174 nm [36] and would be responsible for the shoulder in this region of the experimental spectrum. The Rydberg states  $S_4$  to  $S_6$  (orange) lie within the energy window of the spectra, but have no significant impact due to their low transition dipole moments to the GS.  $S_7$  is the double excitation from  $\pi$  to  $\pi^*$ , which lies at much higher energies and was included for the stability of the AS. The excitations from  $\sigma_{CH}$ , seen in the spectrum of the (4,4) AS, have higher transition dipole moments again, and contribute to the spectrum. The  $\sigma_{CH}\pi^*$  state (magenta) could be responsible for the small kink between 140 and 150 nm of the experimental spectrum.

### 1.2.3 Ethylene CASPT2 on-the-fly dynamics

In addition to verifying the implementation, the non-adiabatic CASPT2 dynamics of ethylene were compared to the CASSCF dynamics, to determine the influence of the higher level quantum chemical method, especially when including the 3s Rydberg state. For this matter, besides the general lifetimes, special attention was given to the CoIn, as the geometries where the trajectories hop, are largely controlled by the newly implemented non-adiabatic couplings. Figure 1.6 shows the comparison of the 6-31G\* dynamics with a (2,2) AS, here still without the Rydberg state. The trajectories all start in the  $S_1$ , the  $\pi\pi^*$  state, from where they usually run into either the pyramidalized, or ethylidene like CoIn (fig. 1.3) and fall back to the GS. The  $S_2$  is only partially and intermediately populated.

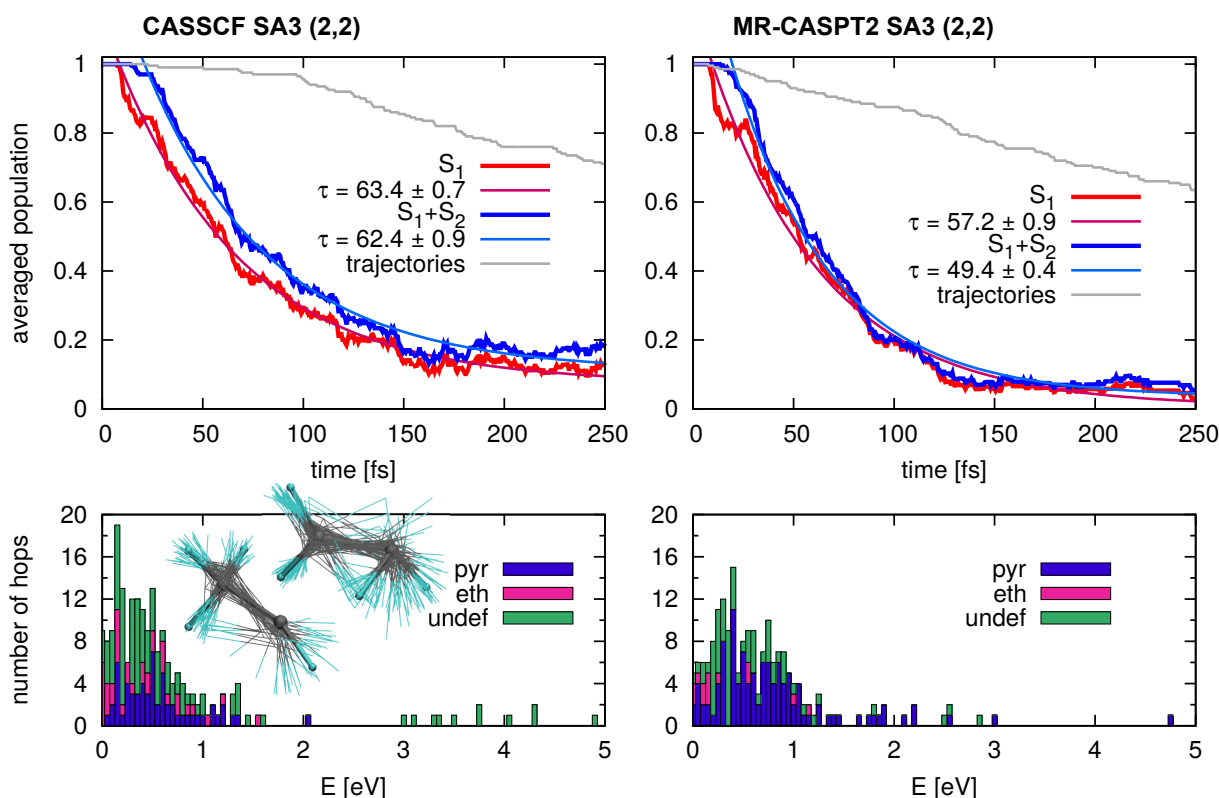


Figure 1.6: Comparison of the CASSCF and MS-CASPT2 non-adiabatic on the fly dynamics with a (2,2) AS, SA3, and 6-31G\* as basis set. Depicted are the populations of  $S_1$  (red), and both excited states together (blue), averaged over the 200 initial trajectories. Both curves are fitted by an exponential function and their lifetimes are provided. The number of trajectories running is indicated by a gray line. (Trajectories at times abort, mainly due to convergence issues.) At the bottom the energy differences of the populated excited state and the GS are shown for all structures where a trajectory hops to the GS for the first time. The structures are assigned to the two minimum energy CoIn, a pyramidalized structure (pyr, red), and a ethylidene like structure (eth, blue). Unassigned structures are labeled undef (green). The aligned structures of the CASSCF trajectories, together with the optimized CoIn are shown in the left plot (pyr on the top right, eth on the bottom left).

The absolute excited state lifetimes ( $\tau$ , blue) of both methods used, are somewhat faster than the results of ab initio multiple spawning dynamics on ethylene, using the same basis set and active space [29] (62 and 49 fs, compared to 111 and 89 fs). They are closer to the experimental values of around 30 fs [42, 43, 44]. The source of the different results of the theoretical methods could be the different dynamics method or starting points, but even changing the exact fitting



procedure can be responsible for this change. We used  $e^{(t-t_0)/\tau} + n_\infty$  as our fitting function, where  $t_0$  accounts for the initial time delay until the decay sets in.  $n_\infty$  is needed because the energy of the molecule is kept constant and thus trajectories can hop back from the GS to excited states. Therefore an equilibrium is reached, rather than a complete depletion of the excited states. When setting both,  $t_0$  and  $n_\infty$ , to zero, our CASSCF dynamics has a lifetime of 106 fs.

Between the two methods, both dynamics simulations show comparable lifetimes, with CASPT2 being 20 % faster. This shows that the common overestimation of the excitation energy of CASSCF does not necessarily increase calculated reaction speeds. The result is in accordance with [29]. We also see the higher portion of pyramidalized CoIns reached in CASPT2, compared to CASSCF. Both, the optimized geometries and structures at which the trajectories reached the GS for the first time in the CASSCF dynamics are depicted in the bottom left section of fig. 1.6. Despite the increased relaxation speed, qualitatively, the amplitudes of all vibrations in the CASPT2 trajectories seem smaller. This is in line with the distribution of CoIns reached. The proportion of ethylidene like CoIns, which need one proton to switch sides, as well as undefined CoIns is higher for CASSCF. Additionally, a small fraction of the propagated molecules dissociate before, or while reaching the GS for the first time. In the CASSCF dynamics 14 molecules break at the CC-bond, and 1 abstracts an H atom. The CASPT2 dynamics exhibits only 3 H- and 2 H<sub>2</sub>-abstractions.

Another source for differing lifetimes can be found in the normal modes, used to generate the Wigner distribution. The comparison to trajectories including the 3s Rydberg state (fig. 1.7) is based on dynamics which were set up using a density functional theory (DFT) frequency analysis calculated with the exchange correlation functional M052X [45], whereas the dynamics presented in figure 1.6 are based on a CCSD frequency analysis. The CASPT2 SA3 (2,2) dynamics, which is, aside from that equal to the CASPT2 dynamics of figure 1.6, is even faster. Looking at effect of the Rydberg orbital (SA6 (2,3)), the dynamics is slowed down slightly, although the Rydberg state itself is only weakly populated (green).

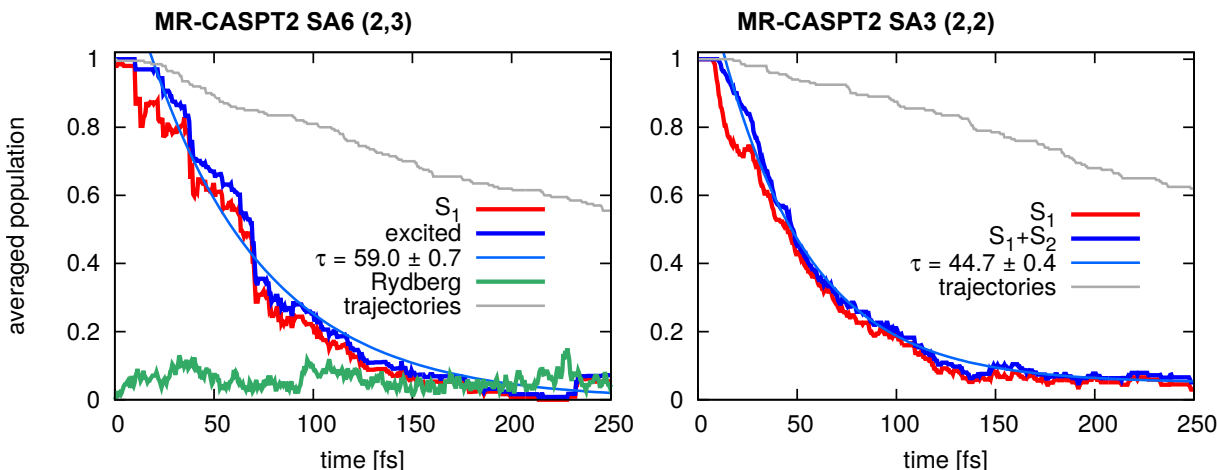


Figure 1.7: Non-adiabatic on-the-fly dynamics of ethylene on MS-CASPT2 level of theory with the (2,2) AS, state averaged over 3 states, and the (2,3) AS including the 3s Rydberg orbital, state averaged over 6 states. Depicted are the populations of S<sub>1</sub> (red), and all populated excited states together (blue), averaged over the 200 initial trajectories. The total excited state curves are fitted by an exponential function and their lifetimes are provided. The number of trajectories running is indicated by a gray line. (Some trajectories abort before reaching 250 fs, mainly due to convergence issues.) In the left picture the number of states which populate the Rydberg state is shown as green curve.

The dynamics simulations accompanied the programming of the CASPT2 part of the interface and were partly performed prior to the spectra. They were not performed with the IPEA shift, which, in retrospect would have been preferable. The non-adiabatic CASPT2 dynamics, in any case, were successfully implemented for the interface between NewtonX and Molpro. The effect of the CASPT2 in comparison to CASSCF is in accordance with Tao et al. [29], who in a later work explains the remaining difference to the experiment with the excited state lifetime not being equal to the photoion yield of the two photon probe of the experiments [46]. This, too, suggests, that the impact of the Rydberg state is likely small.

## Chapter 2

# Substituent effects on the excited state potential surface

Working with a specific class of molecules, oftentimes small changes to the molecular structure in terms of different substituents have large consequences for the physical and chemical properties of the systems. A well known example are mesomeric and inductive effects of substituents influencing the reactivity of benzene derivatives, another one would be steric effects leading to elimination instead of nucleophile substitution. In photochemistry, too, substituents can decisively alter a systems properties [47, 48]. Their influence has to be considered not only at the FC point, where a sometimes instantly visible consequence of substituents is a shifted excitation energy (and accordingly a potentially different color of the compound [49, 50]). Along the whole relaxation pathways the energies of the involved states may be shifted, too, as a result of an altered electronic structure, or because of steric effects. Even new electronic states, interfering with existing decay channels, or introducing new CoIns, can change the course of these reactions.

In most cases, looking at photochemistry, theory is still primarily used to describe and explain experimental findings and the usually fruitful collaboration between different disciplines is highly important. From the theorists perspective, however, one goal of course is to be able to predict the outcome of photochemical reactions, and ultimately be able to tailor molecules to exhibit diverse desired properties.

In this chapter three different sets of molecules will be presented. All sections feature substituents acting on the photorelaxation process of the respective molecules, and in each section the main focus will be on a different part of the respective pathway. Hemithioindigo is analyzed with respect to the FC region, in dihydroxythioindigo the important effect is located upon the pathway, and finally for furan one CoIn is thoroughly analyzed.

## 2.1 The FC point: Tuning the speed of hemithioindigo photoswitches

Hemithioindigos can be used as photoswitches, molecules with different conformers, which can be converted by irradiation with light, at least in one direction. Photoswitches are part of nature - as noted earlier, our vision is based on one - they are researched as medium to store information [7, 8], or can be used to trigger molecular processes [51, 52]. Hemithioindigos combine one thioindigo and one stilbene fragment, which can be rotated between the stable Z and the metastable E conformer around the central double bond. Among the commonly used photoswitches, they most importantly stand out for their absorption in the visible of both conformers, which makes them a potential choice for many biological applications [53].

In the article below, a set of substituents is presented, which systematically reduces the Z to E isomerization time of hemithioindigo. The trend is caused by an increasingly stabilized barrier on the excited state surface, while the FC region is not affected by the substituents at first. At one point, however, the trend is broken by an unexpected change of the electronic character of the state, populated at the FC point.

In the following, the article "Making Fast Photoswitches Faster – Using Hammett Analysis to Understand the Limit of Donor-Acceptor Approaches for Faster Hemithioindigo Photoswitches", *Chem. Eur. J.* **19** (2014), 13984, is reprinted with the permission of John Wiley and Sons. The supplementary information of this article is available under [dx.doi.org/10.1002/chem.201403661](https://dx.doi.org/10.1002/chem.201403661). Key points of the article are:

- The kinetics of the Z/E, as well as the E/Z isomerization of a series of hemithioindigos, substituted differently at the para position of the stilbene moiety, were quantified by ultrafast transient absorption measurements.
- The excited state life times, plotted as function of the Hammett  $\sigma^+$  parameters, exhibit two linear regions - with increasing electron-donor strength of the substituents the isomerization speeds up at first, but at a certain point the trend is reversed and the kinetics slow down again.
- Analysis of excited state calculations explain the findings. Weak electron donators do not significantly affect the FC state, but stabilize the excited state, which leads to the  $S_1/S_0$  CoIn and is populated in the process of the relaxation. Thus the main excited state barrier, located between them, is reduced. At a critical donor strength of the parameter, the energetic order of the excited states at the FC point changes. A formerly higher excited state is stabilized in energy enough, to start interacting with the FC state. Thereby the character of the FC state changes and as outcome it is strongly affected by the electron donating substituent, too.
- Based on the linear regressions, the up to this time fastest hemithioindigo was designed, by substituting two methoxy groups in para- and ortho-position.

## Photochemistry

# Making Fast Photoswitches Faster—Using Hammett Analysis to Understand the Limit of Donor–Acceptor Approaches for Faster Hemithioindigo Photoswitches

Benjamin Maerz,<sup>[b]</sup> Sandra Wiedbrauk,<sup>[a]</sup> Sven Oesterling,<sup>[c]</sup> Elena Samoylova,<sup>[b]</sup> Artur Nenov,<sup>[c]</sup> Peter Mayer,<sup>[d]</sup> Regina de Vivie-Riedle,<sup>[c]</sup> Wolfgang Zinth,<sup>[b]</sup> and Henry Dube<sup>\*[a]</sup>

**Abstract:** Hemithioindigo (HTI) photoswitches have a tremendous potential for biological and supramolecular applications due to their absorptions in the visible-light region in conjunction with ultrafast photoisomerization and high thermal bistability. Rational tailoring of the photophysical properties for a specific application is the key to exploit the full potential of HTIs as photoswitching tools. Herein we use time-resolved absorption spectroscopy and Hammett analysis to discover an unexpected principal limit to the photoisomerization rate for donor-substituted HTIs. By using stationary absorption and fluorescence measurements in combination with theoretical investigations, we offer a detailed mechanistic explanation for the observed rate limit. An alternative way of approaching and possibly even exceeding the maximum rate by multiple donor substitution is demonstrated, which give access to the fastest HTI photoswitch reported to date.

merization rate for donor-substituted HTIs. By using stationary absorption and fluorescence measurements in combination with theoretical investigations, we offer a detailed mechanistic explanation for the observed rate limit. An alternative way of approaching and possibly even exceeding the maximum rate by multiple donor substitution is demonstrated, which give access to the fastest HTI photoswitch reported to date.

## Introduction

### Properties of photoswitches

Hemithioindigos (HTIs)<sup>[1]</sup> are an extraordinary class of photoswitches<sup>[2]</sup> because they offer a combination of advantageous properties not accessible with the most commonly used stilbenes,<sup>[3]</sup> azobenzenes,<sup>[4]</sup> spiropyranes,<sup>[5]</sup> or dithienylethenes.<sup>[6]</sup> HTIs consist of a thioindigo and a stilbene fragment, which are connected through a central, photoisomerizable double bond (Figure 1). The *Z* isomeric form is thermodynamically stable and can be photoisomerized to the metastable *E* isomeric form.<sup>[7]</sup> The back isomerization can be induced either thermally

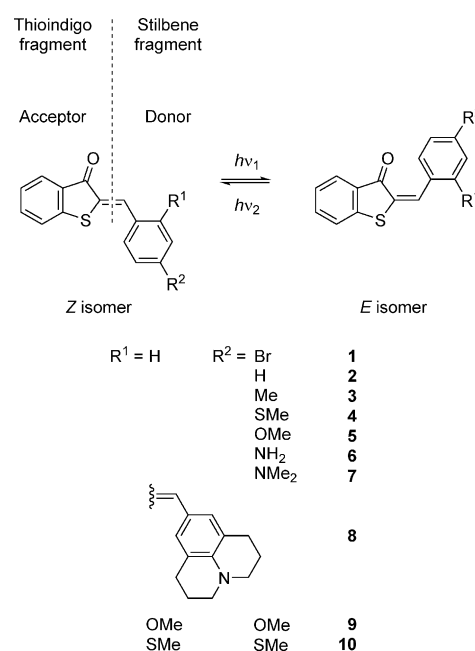


**Figure 1.** Series of HTI derivatives (1–10) analyzed in this work. The central double bond can be described as donor–acceptor substituted. Different substituents at the stilbene fragment of the molecule were chosen to broadly vary the donor strength.

or by irradiation. HTIs show very fast and fatigue resistant<sup>[8]</sup> photoisomerization (ps lifetimes of the excited state), strong absorptions ( $\epsilon = 20\,000\text{--}40\,000\text{ L mol}^{-1}\text{ cm}^{-1}$ ) in the visible region ( $> 400\text{ nm}$ ) for both isomeric forms, they are photochromic, that is, the absorptions for *Z* and *E* isomers are different, and they possess high barriers for the thermal *E/Z* isomeriza-

[a] S. Wiedbrauk,<sup>†</sup> Dr. H. Dube  
Department of Chemistry and Biochemistry  
Ludwig-Maximilians-University Munich  
Butenandtstrasse 5–13, Haus F, 81377 Munich (Germany)  
Fax: (+49) 89-2180-77756  
E-mail: Henry.Dube@cup.uni-muenchen.de

[b] B. Maerz,<sup>†</sup> Dr. E. Samoylova, Prof. Dr. W. Zinth  
Institute for BioMolecular Optics  
Ludwig-Maximilians-University Munich  
Oettingenstr. 67, 80538 Munich (Germany)

[c] S. Oesterling, Dr. A. Nenov, Prof. Dr. R. de Vivie-Riedle  
Department of Chemistry and Biochemistry  
Ludwig-Maximilians-University Munich  
Butenandtstrasse 5–13, Haus E, 81377 Munich (Germany)

[d] Dr. P. Mayer  
Department of Chemistry and Biochemistry  
Ludwig-Maximilians-University Munich  
Butenandtstrasse 5–13, Haus D, 81377 Munich (Germany)

[†] These authors contributed equally to the work

Supporting information for this article is available on the WWW under <http://dx.doi.org/10.1002/chem.201403661>.

tion, i.e.,  $>25$  kcal mol<sup>-1</sup>. Because of these favorable properties, HTIs are of high current interest especially for biology-related applications,<sup>[9]</sup> supramolecular,<sup>[10]</sup> or medicinal chemistry.<sup>[11]</sup> As a result of the growing interest in HTI photoswitches a detailed understanding of their photophysical properties and the possibilities to manipulate them becomes a fundamental necessity. Endowed with such molecular insights, rational tailoring of the properties of HTI photoswitches to a specific application will be possible. Recently, the molecular mechanism of photoisomerization of unsubstituted HTI has been studied theoretically and experimentally,<sup>[12]</sup> allowing to relate photophysical properties to the mechanism of photoisomerization and to extrapolate substitution effects semiquantitatively.

One central property of a photoswitch is the rate of photoisomerization. For most applications it is required to be high, because an instant response to the light signal is desired and competing de-excitation pathways, such as fluorescence, should be suppressed. Moreover, insights into substitution effects<sup>[13]</sup> on the rate of photoswitching allow detailed probing of the excited-state potential energy surface (PES) and advance our understanding of the origins of a variety of photophysical properties, such as absorption, photoisomerization kinetics, or fluorescence output.

The photoisomerization of unsubstituted HTIs takes place at the picosecond timescale<sup>[12]</sup>—a convenient starting point to create ultrafast photoswitching. In general, increasing the photoisomerization rate of a photoswitch can be done by external influences, such as solvent viscosity<sup>[14]</sup> or polarity,<sup>[15]</sup> or internally by substitution. Typically, electronic substitution effects are described within the donor–acceptor or push–pull framework, where faster photoisomerization can be achieved by using stronger donor–acceptor pairs. This approach has been successfully applied to stilbenes<sup>[3c,16]</sup> and azobenzene photoswitches.<sup>[17]</sup> The central double bond of HTI, which inverts its configuration during the photoisomerization process, can also be described as donor–acceptor-substituted double bond. The carbonyl group of the thioindigo fragment serves as acceptor and the substituted phenyl ring of the stilbene fragment as donor (Figure 1). The donor strength can be increased or decreased depending on the specific substitution at the stilbene fragment. Increasing donor strength has been demonstrated to lead to faster photoisomerization kinetics.<sup>[18]</sup>

We will show herein an unexpected limit for the donor–acceptor approach to create

higher photoisomerization rates for HTI photoswitches, how this limit can be explained, and possibly exceeded. We prepared a series of eight HTI derivatives (HTIs **1** to **8** shown in Figure 1) with different substituents at the *para*-position of the stilbene fragment and analyzed the photophysical properties quantitatively. The Hammett parameters ( $\sigma^+$ ) of the substituents used vary broadly between electron acceptors and strong electron donors in the range of 0.15 to  $-2.03$  to cover a wide range of electronic effects. The very strong donor groups NH<sub>2</sub>, NMe<sub>2</sub>, and especially julolidine in HTIs **6** to **8** were expected to lead to strongly accelerated photoisomerization. Additionally, HTIs **9** and **10** were prepared (Figure 1) and the photophysical properties analyzed to illustrate a possible solution for creating faster HTI photoswitches.

## Results and Discussion

### Excited-state dynamics of the Z isomers

We quantified the kinetics of the *Z/E* as well as the *E/Z* photoisomerization processes for the series of substituted HTIs **1–10** by using ultrafast transient absorption measurements and kinetic modeling of the decay.<sup>[19]</sup> For an exemplarily description of the time-resolved data we chose *para*-OMe-substituted HTI **5**. The transient absorption experiment for the *Z/E* isomerization was performed with 400 nm light for the excitation of the *Z* isomer in CH<sub>2</sub>Cl<sub>2</sub> solution. Absorption changes of the *Z* isomer after excitation are presented as a function of time delay and wavelength in Figure 2a. Positive signals are due to excited-state absorption (ESA) with three maxima at 375, 460,

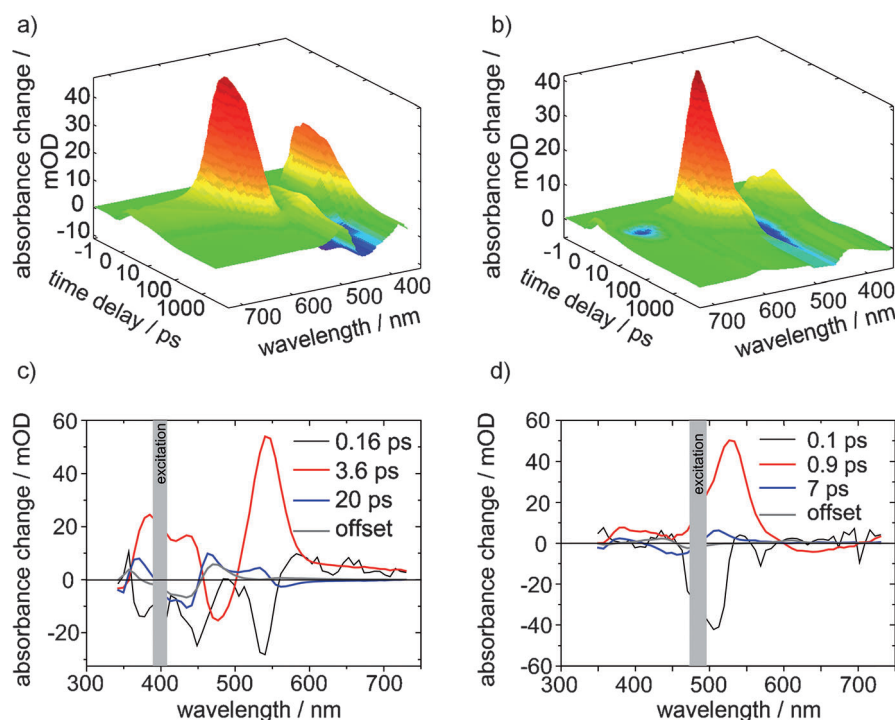


**Figure 2.** a, b) 3D-plots of the transient absorption showing excited-state decay for multiple wavelengths and c, d) decay-associated amplitudes for the fitted lifetimes for HTI **5** in CH<sub>2</sub>Cl<sub>2</sub>. Data for the *Z* isomer are shown in (a) and (c). Data for the *E* isomer are shown in (b) and (d).

and 545 nm. The negative signal observed near 400 nm is a result of ground-state bleaching (GSB). Most of the changes in the transient absorption are observed within the first 10 ps. At longer times, small variations in the amplitude can be seen. The initial fast decay of the maxima can be assigned to the temporal evolution of the excited state. This excited-state decay is followed by a slower process assigned to vibrational cooling in the hot ground state. The remaining signal with sinusoidal amplitude did not decay within the measured time interval (3 ns) and is due to the stationary absorption of the formed *E* isomer. Applying a global fit procedure, the decay dynamics are fitted with the constants  $\tau_1=0.16$  ps,  $\tau_2=3.6$  ps,  $\tau_3=20$  ps, and an offset with a lifetime  $>100$  ns. Each time constant ( $\tau$ ) is characterized by an amplitude that changes with the wavelength (decay-associated spectrum or DAS) as shown in Figure 2b. The time constant  $\tau_1=0.16$  ps is associated with fast nuclear motions and solvent reorganization immediately after the excitation pulse and a relaxation from the initially populated Franck-Condon (FC) region. Further time evolution in the excited state is described with a time constant  $\tau_2=3.6$  ps, after which no more signal from the excited state is observed. For the *Z* isomers,  $\tau_2$  describes the *Z/E* photoisomerization rate and is called  $\tau_{Z/E}$  from here on. The dynamics with the lifetime  $\tau_3$  describe thermal relaxation in the electronic ground state ( $S_0$ ). Depending on the HTI,  $\tau_3$  lifetimes in the range of 12 to 20 ps were found.

The same data-evaluation procedure was applied to all studied compounds to determine the excited-state lifetimes  $\tau_{Z/E}$ . These data are summarized in Table 1 together with stationary absorption and fluorescence data, calculated excitation energies, and the measured quantum yields of the *Z/E* photoisomerization ( $\eta_{Z/E}$ ) and will be discussed below.

Table 1. Summary of measured lifetimes ( $\tau_{Z/E}(R)$ ) associated with the decay of the excited state, stationary absorption and fluorescence maxima, calculated stationary absorption energies (coupled cluster (CCSD) level of theory), quantum yields $\eta_{Z/E}$ , and $\sigma^+$ Hammett parameters of the substituents for the <i>Z</i> isomers of HTI 1–10. The experiments were conducted in $\text{CH}_2\text{Cl}_2$ .							
HTI	R	$\sigma^+$	$\tau_{Z/E}(R)$ [ps]	$S_0-S_1$ trans. max. [nm]	$S_1-S_0$ trans. max. [nm]	$S_0-S_1$ trans. calcd [nm]	$\eta_{Z/E}$ [%]
1	<i>p</i> -Br	0.15	60.0	436	495	–	18
2	<i>p</i> -H	0.00	38.0	433	490	328	23
3	<i>p</i> -Me	-0.31	13.0	436	488	–	14
4	<i>p</i> -SMe	-0.60	4.8	449	495	–	23
5	<i>p</i> -OMe	-0.78	3.6	442	485	331	17
6	<i>p</i> -NH <sub>2</sub>	-1.30	2.4	457	513	336	21
7	<i>p</i> -NMe <sub>2</sub>	-1.70	10.0	484	549	346	16
8	Julolidine	-2.03 <sup>[20]</sup>	29.0	514	584	356	20
9	<i>o,p</i> -OMe	–	2.4	453	509	–	22
10	<i>o,p</i> -SMe	–	5.0	457	514	–	16

### Excited-state dynamics of the *E* isomers

The excited-state dynamics for the *E* isomer of HTI 5 are shown in Figure 2c,d. 480 nm light was used for excitation of the *E* isomer to minimize excitation of residual *Z* isomer (see

Figure 11 in the Supporting Information). As for the *Z* isomer, the positive signals at 530 and 380 nm in the transient absorption spectra correspond to the ESA. The negative signals are due to GSB. The ESA signal decays very rapidly at early time delays (Figure 2c), and no further contributions associated with the excited-state population are observed. At later delay times, only a contribution due to vibrational cooling and a constant offset corresponding to the formed *Z* isomer are present. The fitted time constants and the amplitudes are shown in the DAS in Figure 2d. The time constant  $\tau_1=0.10$  ps was assigned to relaxation from the initially populated FC region and solvent reorganization and is followed by an excited-state decay with a time constant  $\tau_2=0.90$  ps. The vibrational cooling of a hot ground state is described with a time constant  $\tau_3=7$  ps. Depending on the HTI,  $\tau_3$  lifetimes in the range of 4 to 13 ps were found.

The measured lifetimes of the excited state of the *Z* isomers describe directly the *Z/E* photoisomerization kinetics, because this is the main pathway for de-excitation. The corresponding lifetimes of the *E* isomers however, are a composite of two processes leading to de-excitation (see Figure 5 in the Supporting Information).<sup>[12]</sup> The faster process is an internal conversion (IC) leading exclusively to *E* isomer without a significant barrier. The slower process is the photoisomerization pathway that proceeds over a barrier and results in the formation of *Z* and *E* isomers in an approximate ratio of 1:1.<sup>[12]</sup> Because of the fast IC

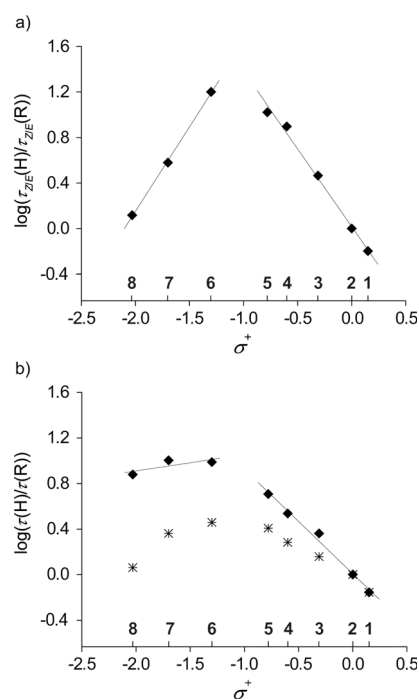


**Figure 3.** Hammett correlations between the  $\sigma^+$  constant of the *para*-substituents of HTIs 1 to 8 (indicated by bold numbers above the x axes) in  $\text{CH}_2\text{Cl}_2$  and the photoisomerization kinetics. a) Correlation between the  $\sigma^+$  constant and the *Z/E* photoisomerization rates obtained from the measured excited-state lifetimes of the *Z* isomer ( $\tau_{Z/E}$ ). b) Correlation between the  $\sigma^+$  constant and the measured excited-state lifetimes of the *E* isomer ( $\tau_E$ , \*), and *E/Z* photoisomerization lifetimes ( $\tau_{E/Z}$ ,  $\blacklozenge$ ) calculated from the measured excited-state lifetimes ( $\tau_E$ ) and the quantum yield of *E/Z* photoisomerization. The data for HTI 2 were taken from the literature.<sup>[18b]</sup>

proceeding without isomerization, the de-excitation kinetics are dominated by this process. The kinetics of the *E/Z* photoisomerization ( $\tau_{E/Z}$ ) were extracted from the de-excitation kinetics by taking into account the quantum yield for the formation of the *Z* isomer (see the Supporting Information for details).

The same data-evaluation procedure was applied to all studied compounds to determine the excited-state lifetimes,  $\tau_E$ . The lifetimes are summarized in Table 2 together with the extracted lifetimes associated with *E/Z* photoisomerization ( $\tau_{E/Z}$ ), stationary absorption data, and the quantum yields of the *E/Z* photoisomerization and will be discussed below.

Table 2. Summary of the measured lifetimes ( $\tau_E(R)$ ) associated with the decay of the excited state, extracted lifetimes associated with <i>E/Z</i> photoisomerization ( $\tau_{E/Z}(R)$ ), stationary absorption maxima, quantum yields $\eta_{E/Z}$ and the $\sigma^+$ parameters for the <i>E</i> isomers of all studied HTI derivatives 1-10. The experiments were conducted in $\text{CH}_2\text{Cl}_2$ .						
HTI	R	$\sigma^+$	$\tau_E(R)$ [ps]	$\tau_{E/Z}(R)$ [ps]	$S_0-S_1$ trans. max. [nm]	$\eta_{E/Z}$ [%]
1	<i>p</i> -Br	0.15	3.3	33.0	454	5
2	<i>p</i> -H	0.00	2.3	23.0	457	5
3	<i>p</i> -Me	-0.31	1.6	10.0	461	8
4	<i>p</i> -SMe	-0.60	1.2	6.7	459	9
5	<i>p</i> -OMe	-0.78	0.9	4.5	467	10
6	<i>p</i> -NH <sub>2</sub>	-1.30	0.8	2.4	488	17
7	<i>p</i> -NMe <sub>2</sub>	-1.70	1.0	2.3	513	22
8	Julolidine	-2.03 <sup>[20]</sup>	2.0	3.0	545 <sup>[a]</sup>	33
9	<i>o,p</i> -OMe	-	0.6	1.4	467	21
10	<i>o,p</i> -SMe	-	0.8	2.7	466	15

[a] The absorption of the *E* isomer of HTI 8 could not be measured directly because of its very fast thermal *E/Z* isomerization in  $\text{CH}_2\text{Cl}_2$  and was estimated from the photostationary state (PSS).

### Hammett analysis of *Z/E* and *E/Z* photoisomerization kinetics

The influence of the different substituents on the excited-state properties of HTIs 1–8 can be analyzed with the help of Hammett correlations. In Figure 3, the excited-state lifetimes are plotted as a function of the Hammett  $\sigma^+$  parameter of the substituents at the stilbene fragment. For comparison we also plotted the dependence of the lifetime on the Hammett  $\sigma$  parameter (Figure 6 in the Supporting Information). A better correlation is found for the  $\sigma^+$ -dependent plots similar to earlier results.<sup>[18a]</sup>

Two sets of linear trends were found in the Hammett correlations of the photoisomerization kinetics. For the series of HTIs 1–5 with substituents at the stilbene fragment that act as acceptors or medium-strong donors, the photoisomerization rate increases with increasing donor strength of the substituent. This trend is observed for both, the *Z/E* as well as the *E/Z* photoisomerization processes. For derivative 6 with a strong NH<sub>2</sub> donor substituent, the fastest photoisomerization was observed with  $\tau_{Z/E} = \tau_{E/Z} = 2.4$  ps. However, the very strong donor substituents NMe<sub>2</sub> and julolidine in HTIs 7 and 8, respectively, do not lead to a further increase of the photoisomerization rate. Instead an abrupt change of the photoisomerization ki-

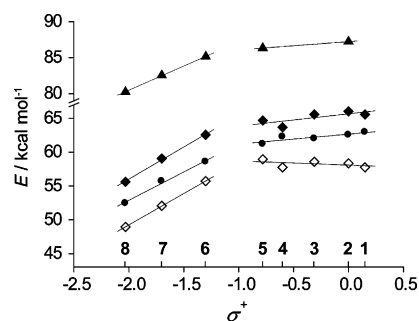


**Figure 4.** Hammett correlation between the  $\sigma^+$  constant of the *para*-substituent of HTIs 1–8 (indicated by bold numbers above the x axis) in  $\text{CH}_2\text{Cl}_2$  and the absorption energy ( $\bullet$ ) or fluorescence energy ( $\diamond$ ) of the *Z* isomers, and the absorption energy ( $\blacktriangle$ ) of the *E* isomers. The fluorescence energies of the *E* isomers could not be measured unambiguously because of spectral overlap with the fluorescence of residual *Z* isomers. The strongly donating substituents NH<sub>2</sub>, NMe<sub>2</sub>, and julolidine (HTIs 6–8) lead to a decrease of the absorption energy and the fluorescence energy. Calculated excitation energies at the FC point for the *Z* isomers of HTIs 2, 5, 6, 7, and 8 ( $\blacktriangle$ ) show very similar behavior.

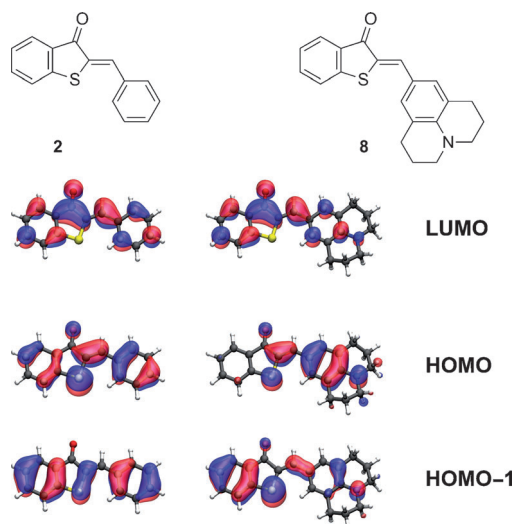


**Figure 5.** HOMO–1, HOMO, and LUMO of the *Z* isomers of HTIs 2 and 8, calculated at the CCSD level of theory.

netics is observed for HTIs 6–8 with a reversed trend, that is, stronger donor character of the substituent leads to slower photoisomerization kinetics.

### Stationary absorption and fluorescence

To aid an explanation of the sudden trend change in the photoisomerization kinetics, we analyzed the stationary absorption and fluorescence characteristics within the series of HTIs 1–8 (Figure 4, Table 1, and Table 2). For HTIs 1–5, with substituents with widely different donor strengths (Br to OMe, that is,  $\sigma^+ = 0.15$ – $-0.78$ ), no significant variation of the absorption energy is seen. Only if the stronger donor substituents NH<sub>2</sub>, NMe<sub>2</sub>, and julolidine are used (HTIs 6–8), a reduction of the absorption energy is observed with increasing donor strength. We also measured the stationary fluorescence of the *Z* isomers of HTIs



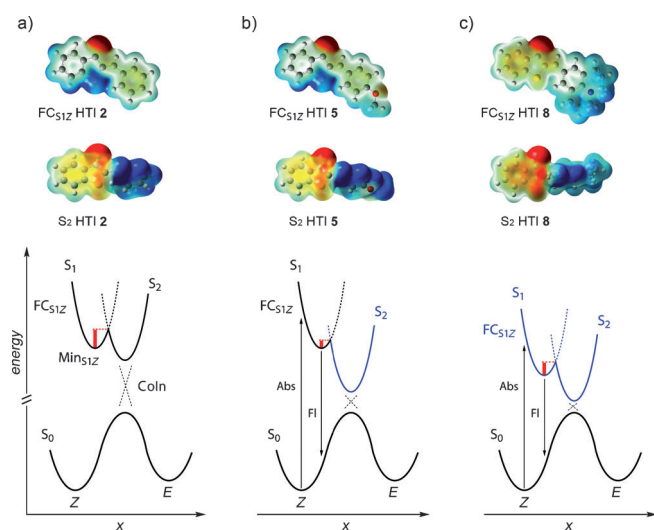


**Figure 6.** Schematic representation of the  $S_1$  PES for the  $Z/E$  photoisomerization of the  $Z$  isomer and ESPs of HTIs **2**, **5**, and **8** with important points indicated. The ESPs are visualized as color code on an electronic density isosurface (blue: positively charged, red: negatively charged). The excited-state barrier is the result of an avoided crossing between  $S_1$  and  $S_2$  potential wells (the barrier height is indicated by the red bars). a) The polarization of HTI **2** at the  $FC_{S1Z}$  structure is depicted together with the polarization of the  $S_2$  structure close to the Coln. The polarization of the  $FC_{S1Z}$  structure is essentially the same as in the  $Min_{S1Z}$  region. b) Electron-donor substituents in the *para*-position of the stilbene fragment (OMe in HTI **5**) only stabilize the polarized structure of the  $S_2$  excited state. The stabilization of  $S_2$  against the unaffected  $S_1$  leads to a smaller barrier (red bar) and therefore faster photoisomerization kinetics. c) The  $FC_{S1Z}$  structure of HTI **8** exhibits a polarization different from HTIs **2** and **5**. The positive charge is now localized at the *para*-substituent of the stilbene fragment and not at the sulfur atom of the thioindigo fragment. For HTI **8**, the  $S_1$  excited state is therefore stabilized (red-shifted stationary absorption and fluorescence) counterbalancing the stabilization of the  $S_2$  excited state. The result is an increase of the barrier for photoisomerization (red bar) if very strong donor substituents are used at the *para*-position of the stilbene fragment. Absorption (Abs) and fluorescence (FI) are depicted by black arrows.

**1–8** and plotted the fluorescence energy against the Hammett  $\sigma^+$  parameters of the different substituents (Figure 4). Again, the strong donor substituted HTIs **6–8** show significantly reduced fluorescence energies in comparison with the small variations found for HTIs **1–5**. A similar Hammett analysis of the absorption properties of the  $E$  isomers reveals the same trend, that is, strong-donor-substituted HTIs **6–8** show significantly diminished absorption energy in comparison with unaffected HTIs **1–5**. The fluorescence properties of the  $E$  isomers could not be established because of spectral overlap with the fluorescence of residual  $Z$  isomer.

Together with the experimental values for stationary absorption, the corresponding calculated excitation energies at the FC point are shown for the  $Z$  isomers of HTIs **2**, **5**, **6**, **7**, and **8** in Figure 4. The theoretically obtained energies are higher than the experimental ones, but show a very similar behavior. For HTIs **6–8**, the excitation energy is dependent on the substituent, whereas no significant dependence was found for HTIs **2** and **5**. Again, a trend is observed where stronger donor substituents lead to smaller excitation energies. The differences between the calculated excitation energies of, for example, HTI

**5** and **7** or **8** are 3.8 and 6.1 kcal mol<sup>-1</sup>, respectively. These values match the measured substituent effects on the absorption energy in CH<sub>2</sub>Cl<sub>2</sub> where the excitation energy is lowered by 5.6 and 9.1 kcal mol<sup>-1</sup> for HTIs **7** and **8**, respectively.

### Theoretical results

Substituent effects on the excited-state properties for the  $Z$  isomers of HTIs **2**, **5**, **6**, **7**, and **8** were compared at the CCSD level of theory. At the FC point, the relative excitation energies (Figure 4) as well as the oscillator strengths (see Table 3 in the Supporting Information) fit well with the experimental data. The characteristic changes in these physical properties for HTIs **6**, **7**, and **8** (with  $\sigma^+$  of  $-1.30$ ,  $-1.70$ , and  $-2.03$ , respectively) are well reproduced in the theoretical description. An explanation for the observed changes can be found by analyzing the character of the first optically accessible excited state ( $S_1$ ), for which the charge distribution is significantly altered for HTIs **7** and **8** compared with HTIs **2** or **5**.

The  $S_1$  state, a  $\pi\pi^*$  excitation, is mainly described by a HOMO–LUMO excitation in all HTIs. For HTI **2** these two orbitals are distributed over the whole molecule (Figure 5). Their distribution mainly differs at the sulfur atom, where the LUMO has no contributions. For HTI **8**, the shape of the LUMO essentially stays the same, whereas the HOMO shows significant differences. For HTI **2**, HOMO and HOMO–1 are both delocalized over the whole molecule, whereas for HTI **8** these orbitals mix and become localized. The HOMO of HTI **8** is mainly located on the stilbene fragment, whereas the HOMO–1 is located on the thioindigo fragment. With both HOMO and HOMO–1 doubly occupied, the charge distribution of the ground state ( $S_0$ ) of HTI **8** is not affected. In the  $S_1$  state however, with an excitation from the localized HOMO to the delocalized LUMO, a charge separation is induced. The electron density is shifted from the stilbene to the thioindigo fragment (see the electrostatic potentials (ESPs) in Figure 6, top). A similar charge separation after excitation is also observed for HTIs **6** and **7**, whereas HTI **5** behaves very similar to HTI **2** (see also Table 3 in the Supporting Information for the corresponding dipole moments of the  $S_0$  and  $S_1$  states). For the strong-donor-substituted HTIs (**6–8**), the excitation energy now depends on the donor strength. A trend is created where stronger donor substituents lead to a stabilization of the  $S_1$  state.

### Explanation for the trend change in $Z/E$ photoisomerization kinetics

To explain the changed trend in photoisomerization kinetics the mechanism of photoisomerization has to be considered more closely (see Figure 5). Upon photoexcitation of the  $Z$  isomer the FC region ( $FC_{S1Z}$ ) is populated. According to the theoretical model,<sup>[12]</sup> the FC transition of the  $Z$  isomer of HTI **2** leads to a strong polarization of the molecule, where positive charge accumulates at the sulfur atom and negative charge at the carbonyl oxygen atom. Effects of substituents at the *para*-position of the stilbene fragment are not expected to be important at this early stage, because they do not affect this ini-

tial polarization. In agreement with that model are the small substituent effects on the absorption energy for HTI **5** versus HTI **2** observed theoretically and the experimentally found weak substitution effects on the absorption energy for HTIs **1** to **5**. Even widely different donor strengths (Br to OMe, that is,  $\sigma^+ = 0.15 - -0.78$ ) do not change the absorption energy as shown in Figure 4. When the excited HTI **2** quickly moves out of the  $FC_{S_{1Z}}$  region, the initial polarization persists until a local minimum ( $Min_{S_{1Z}}$ ) is reached (Figure 6a). Again, substituents at the stilbene fragment should not influence the  $Min_{S_{1Z}}$ , because they do not affect the polarization. The  $Min_{S_{1Z}}$  can be probed directly by measuring stationary fluorescence. Experimentally observed substituent effects on the stationary fluorescence energy are indeed small for HTIs **1–5** (see Figure 4).

Before the molecule can leave the  $Min_{S_{1Z}}$  region and enter the conical intersection (Coln) to reach the ground state ( $S_0$ ), a barrier has to be overcome (red bars indicate the barrier heights in Figure 6). This barrier is the result of a crossing between two excited-potential surfaces: the  $S_1$  state and another excited state ( $S_2$ ) with charge-transfer character. The  $S_2$  excited state is strongly polarized with a positive charge on the stilbene fragment. This polarized structure of the  $S_2$  excited state can be stabilized by donor substituents at the *para*-position of the stilbene fragment leading to a lowering of the energy. In contrast, the  $S_1$  state with the positive charge at the sulfur atom is not affected by these donor substituents. The substituent induced stabilization of the  $S_2$  state versus the unaffected  $S_1$  state reduces the barrier of photoisomerization as shown schematically in Figure 6b for HTI **5**. Thus, the photoisomerization is accelerated with increasing donor strength of the substituent at the stilbene fragment as found experimentally for HTIs **1–5** (Figure 3).

When the very strong donor groups  $NH_2$ ,  $NMe_2$ , and julolidine are used (HTIs **6–8**), a different behavior occurs. Now a significant stabilization of the  $S_1$  state is observed, leading to diminished absorption energies (Figure 4). The stabilization of the  $FC_{S_{1Z}}$  structure in HTIs **6–8** is explained by the change of the electronic character of the  $S_1$  state. The *para*-amine substituents stabilize the positive partial charge generated during photoexcitation in the  $FC_{S_{1Z}}$  region. Similarly, a significant stabilization of the  $Min_{S_{1Z}}$  structure is observed for HTIs **6–8**, as can be seen from the Hammett plots of the stationary fluorescence energy (Figure 4). Again, localization of the partial positive charge at the amine substituent is responsible for the observed stabilization of the  $Min_{S_{1Z}}$ . The effect of  $S_2$  excited-state stabilization on lowering the barrier for photoisomerization is thus counterbalanced by  $S_1$  state stabilization. This leads to an increase of the barrier instead of a further decrease (Figure 6c). The unexpected deceleration of the photoisomerization rate with stronger donor substitution of HTIs **7** and **8** can therefore be explained in terms of concomitant stabilization of the  $S_1$  and the  $S_2$  excited states. Thus, a rate limit for photoisomerization of donor-substituted HTI photoswitches is established.

A similar mechanism is operative for the corresponding  $E/Z$  photoisomerization, leading again to a rate limit for this photoisomerization direction with strong donor substituents at the stilbene fragment.

### Approaching the limit of HTI photoisomerization rate

The limit for the donor–acceptor approach to increase the photoisomerization rate can now be estimated quantitatively by the Hammett  $\sigma^+$  value at which the linear regressions of the two subsets of data (HTIs **1–5** and HTIs **6–8**; Figure 3a,b) meet. A  $\sigma^+$  value of  $-1.1$  was found consistently for both the  $Z/E$  and  $E/Z$  direction. By using an appropriate donor substituent with that  $\sigma^+$  constant it should be possible to achieve the maximum rate of photoisomerization for HTIs with a lifetime of only 1.2 ps for the  $Z/E$  direction and a lifetime of 0.6 ps for the  $E/Z$  direction.

Instead of using a single substituent to approach the limit for HTI photoisomerization rate, it is also possible to use more than one medium strong donor group at the stilbene fragment of the molecule. Thus, HTI **9** was prepared, bearing one *ortho*- and one *para*-OMe group. This substitution leads to a  $Z/E$  photoisomerization time constant of 2.4 ps, which is as fast as for  $NH_2$ -substituted HTI **6**. Similarly, an increase of the  $E/Z$  photoisomerization time constant to 1.4 ps is observed for HTI **9**, already exceeding the  $E/Z$  photoisomerization rate of HTI **6**. Hence, HTI **9** shows the fastest photoisomerization of a HTI reported to date. To approximate the extent of donating ability of the two OMe substituents in HTI **9**, the Hammett  $\sigma^+$  constant of the *para*-OMe substituent was doubled, yielding a  $\sigma^+$  value of  $-1.56$ . This donor strength should already lead to a deceleration of the photoisomerization kinetics and a significant redshift of the absorption and fluorescence; this is not observed in this case. Apparently, multiple weak donor substituents at the stilbene fragment of HTIs can be used to approach and possibly even exceed the rate limit of photoisomerization set by a single strong donor. However, for the analogous double substitution with SMe substituents (HTI **10**), no increase of the photoisomerization rate was detected.

## Conclusion

Rational design of HTI photoswitches to enable the broad applicability in, for example, biology or supramolecular chemistry is still limited by incomplete understanding of the photophysical properties. To gain detailed insight into substitution effects on the photoswitching behavior, we synthesized a series of substituted HTIs and analyzed the photoisomerization rates, absorption and fluorescence profiles, quantum yields, as well as thermal bistability. By increasing the donor strength of the substituents at the stilbene fragment, we were able to significantly increase the photoisomerization rate of the HTI photoswitches. However, we found that there is a limit to the donor–acceptor approach, beyond which an increase in the substituent's donating capacity does not further increase the photoisomerization rate. Instead, HTIs with very strong donor substituents, such as  $NH_2$ ,  $NMe_2$ , or julolidine, at the stilbene fragment follow an opposite trend where stronger donor capacity leads to slower photoisomerization. Taking both trends into account, we were able to identify a principal upper limit of the photoisomerization rate for donor-substituted HTIs. This

maximum photoisomerization rate will be observed for a substituent with a Hammett  $\sigma^+$  constant of  $-1.10$ .

Based on Hammett analyses of stationary absorption and fluorescence energies as well as theoretical investigations of the excited states, we propose a model to explain this behavior. According to our model, the deceleration of the photoisomerization rate is a result of concomitant stabilization of the  $S_1$  and the  $S_2$  excited states, whose crossing point defines the reaction barrier. Our model allows a fundamental understanding of the unusual absorption, fluorescence, and photoisomerization behavior of HTIs and the counterintuitive effects of substitution. It will therefore serve as a solid basis for future rational design of HTI-based molecular devices.

In addition, we established an alternative approach that could potentially overcome the observed rate limit of photoisomerization by using multiple weak donor substituents. With this approach we were able to generate the fastest photoisomerizing HTI reported to date. Future investigations will be aimed at exploiting this substitution pattern to create ultrafast HTI photoswitches, exceeding the established photoisomerization rate limit.

## Materials and Methods

### Chemical synthesis and characterization

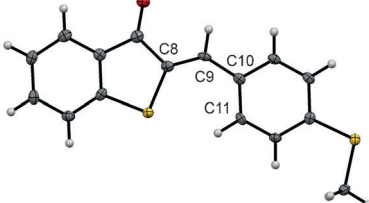
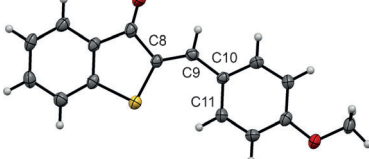
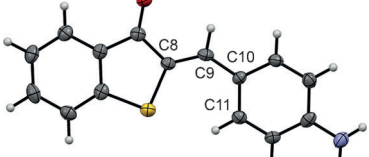
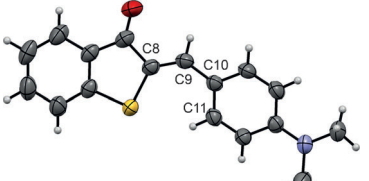
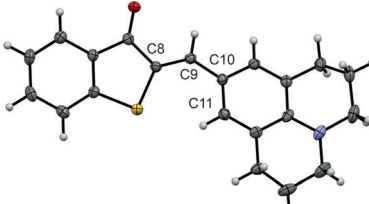
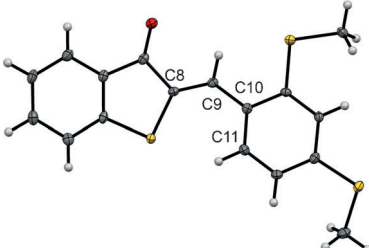
HTIs 1–10 was synthesized following established protocols for HTI synthesis<sup>[8–10]</sup> and is outlined in the Supporting Information. All compounds were fully characterized, including extinction coefficients for both isomeric forms in  $\text{CH}_2\text{Cl}_2$  and thermal stability of the *E* isomeric forms in  $[\text{D}_8]\text{toluene}$ . The kinetic measurements of the thermal *E/Z* isomerization were carried out in toluene, because measurements in  $\text{CD}_2\text{Cl}_2$  gave inconsistent results. For HTI 8 the extinction coefficients of the *E* isomer were measured in toluene, because of the low barrier ( $< 20 \text{ kcal mol}^{-1}$ ) for the thermal *E/Z* isomerization in  $\text{CH}_2\text{Cl}_2$ . For HTIs 4, 5, 6, 7, 8, and 10, X-ray crystallographic analysis confirmed the expected planar structures. Essential structural details are given in Table 3. The bond

lengths of the central double bonds (C8C9) as well as the bond lengths of the neighboring single bonds to the stilbene fragment of the molecule (C9C10) do not show any significant variations.

### Time-resolved absorption measurements

The pump–probe setup for the time-resolved experiments is based on a Ti:Sapphire amplified laser system (Spitfire Pro, Tsunami, Spectra Physics) that delivers pulses at a central wavelength of 800 nm, with a repetition rate of 1 kHz and a pulse duration of 100 fs. The output of the laser is split into a pump and a probe pulses. The pump pulse is frequency doubled ( $\lambda = 400 \text{ nm}$ ) and, if required,

**Table 3.** Selected parameters of the crystal structures of HTIs 4, 5, 6, 7, 8, and 10 in the *Z* isomeric form.

Structure	HTI	CCDC No.	C8–C9 [Å]	C9–C10 [Å]	C8–C9–C10–C11 [°]
	4	CCDC-1004239	1.350	1.448	2.6
	5	CCDC-1004240	1.349	1.450	2.2
	6	CCDC-1004241	1.348	1.437	6.0
	7	CCDC-1004242	1.334, 1.341	1.444, 1.449	12.5, 11.1
	8	CCDC-1004243	1.355	1.442	12.4
	10	CCDC-1004244	1.353	1.452	2.70

converted into light in the visible spectral range by using a home-built two-stage non-collinear optical parametric amplifier (NOPA).<sup>[21]</sup> For the excitation of the HTI-derivatives presented here, the excitation (pump) wavelengths of 400, 480, 500, 530, and 580 nm were used. The NOPA-output was compressed with a prism pair to a pulse duration between 70 and 100 fs and the pump pulses were temporarily delayed with a delay stage before interacting with the sample solution. The white-light pulses ( $\lambda = 350\text{--}700$  nm), used as the probe, are generated by super-continuum generation from the 800 nm light in a rotating CaF<sub>2</sub> plate.<sup>[22]</sup> The pump and the probe laser beams are focused and overlapped on the sample cuvette with polarization at magic angle. The excitation energy per pulse on the sample is 200–300 nJ. A mechanical chopper blocks every second excitation pulse to improve referencing. The transient absorption spectra at each delay time are recorded with a home-built spectrometer. The sample was dissolved in CH<sub>2</sub>Cl<sub>2</sub> and continuously circulated with a peristaltic pump (Ismatec, ISM404B) during a time-resolved measurement to allow the sample solution to exchange between two consequent laser shots. The sample used was returned to a reservoir and photoisomerized back to the initial pure isomeric content by irradiation with suitable wavelengths: 420 or 490 nm light-emitting diodes (LEDs; Roithner Lasertechnik GmbH) were employed to obtain *E* isomers and a white-light source (Schott, KL2500 LCD) with colored glass filters (GG495–OG570 and KG5, Schott) to obtain *Z* isomers. For measurements of the *E* isomers, freshly prepared solutions containing only *Z* isomer were preilluminated to the photostationary state with 420 or 490 nm LEDs. Stationary UV/Vis absorption spectra (Shimadzu, UV1800) were recorded before and after transient measurements to guarantee consistent sample conditions during the transient measurements.

### Quantum-yield measurements

The photochemical quantum-yields of the photoisomerizations ( $\eta_{Z/E}$  or  $\eta_{E/Z}$ ) were calculated as the ratio between the number of isomerized molecules ( $n_z$  or  $n_e$ ) and the number of absorbed photons ( $n_{hv}$ ). HTI samples were dissolved in 3 mL of CH<sub>2</sub>Cl<sub>2</sub> and, for the *E/Z* reaction, preirradiated with suitable wavelengths to obtain high content of the *E* isomer. The absorption of the solution at the irradiation wavelength was adjusted to be 3 OD to guarantee >99% absorption. Irradiation was carried out with a cw laser at 440 nm (RLTMDL-442-10-5, Roithner Lasertechnik GmbH), 472 nm (VA-I-N-473, Viasho) and with a tunable nanosecond laser (NT200, Ekspla) at several wavelengths in the range of 440–570 nm. Irradiation wavelengths were chosen to match the absorption spectra of the *Z* and *E* isomers. To calculate the number of the isomerized molecules, absorption at a suitable read-out wavelength was recorded (Shimadzu, UV1800) as a function of irradiation time. For the quantum yield calculations, only the linear part of the data was used. Absorption changes of HTI **8** were corrected for the fast thermal *E/Z* isomerization.

### Computational details

The theoretical calculations were performed with the program packages Gaussian09<sup>[23]</sup> and Molpro2012.<sup>[24]</sup> A standard basis set 6-31G\* was used. The ground state minimum geometries were located by using density functional theory (DFT) with the B3LYP functional. The selected geometries used for the ESPs of the *S*<sub>2</sub> potential energy surfaces had to be optimized on complete active space self consistent field (CASSCF) level of theory (see the Supporting Information). All physical properties were then calculated by using equation-of-motion coupled cluster (EOM-CCSD) theory. The state

specific wavefunctions needed for the ESPs (*S*<sub>1</sub> and *S*<sub>2</sub>) also stem from CASSCF calculations.

### Acknowledgements

The authors thank O. Brix for help during measurements and evaluation of the data for the photoisomerization quantum yields and T. Herzog for providing transient absorption data of the *E* isomer of HTI **2**. H. Dube thanks the Fonds der Chemischen Industrie for a Liebig fellowship. We thank the collaborative research center SFB749 and the Clusters of Excellence Center for Integrated Protein Science Munich (CiPS<sup>M</sup>) and Munich-Centre for Advanced Photonics (MAP) for financial support.

**Keywords:** ab initio calculations · isomerization · photochemistry · photochromism · time-resolved spectroscopy

- [1] a) P. Friedlaender, *Monatsh. Chem.* **1909**, *30*, 347–354; b) M. A. Mostoslavskii, V. A. Izmail'skii, *J. Gen. Chem. USSR* **1961**, *31*, 21–31; c) M. A. Mostoslavskii, V. A. Izmail'skii, M. M. Shapkina, *J. Gen. Chem. USSR* **1962**, *32*, 1731–1739; d) M. A. Mostoslavskii, V. A. Izmail'skii, *J. Gen. Chem. USSR* **1963**, *33*, 727–731; e) M. A. Mostoslavskii, V. A. Izmail'skii, *J. Gen. Chem. USSR* **1965**, *35*, 519–523.
- [2] a) M. M. Russev, S. Hecht, *Adv. Mater.* **2010**, *22*, 3348–3360; b) M. Natali, S. Giordani, *Chem. Soc. Rev.* **2012**, *41*, 4010–4029; c) T. Fehrentz, M. Schonberger, D. Trauner, *Angew. Chem.* **2011**, *123*, 12362–12390; *Angew. Chem. Int. Ed.* **2011**, *50*, 12156–12182.
- [3] a) J. Saltiel, E. D. Megarity, K. G. Kneipp, *J. Am. Chem. Soc.* **1966**, *88*, 2336–2338; b) D. H. Waldeck, *Chem. Rev.* **1991**, *91*, 415–436; c) V. Papper, G. Likhtenshtein, *J. Photochem. Photobiol. A* **2001**, *140*, 39–52; d) C. A. Stanier, S. J. Alderman, T. D. W. Claridge, H. L. Anderson, *Angew. Chem.* **2002**, *114*, 1847–1850; *Angew. Chem. Int. Ed.* **2002**, *41*, 1769–1772.
- [4] a) H. M. Bandara, S. C. Burdette, *Chem. Soc. Rev.* **2012**, *41*, 1809–1825; b) D. Bléger, J. Schwarz, A. M. Brouwer, S. Hecht, *J. Am. Chem. Soc.* **2012**, *134*, 20597–20600; c) A. A. Beharry, O. Sadovski, G. A. Woolley, *J. Am. Chem. Soc.* **2011**, *133*, 19684–19687; d) M. Banghart, K. Borges, E. Isacoff, D. Trauner, R. H. Kramer, *Nat. Neurosci.* **2004**, *7*, 1381–1386; e) M. Volgraf, P. Gorostiza, R. Numano, R. H. Kramer, E. Y. Isacoff, D. Trauner, *Nat. Chem. Biol.* **2006**, *2*, 47–52; f) S. Venkataramani, U. Jana, M. Dommaschk, F. D. Sonnichsen, F. Tuczek, R. Herges, *Science* **2011**, *331*, 445–448; g) A. Archut, G. C. Azzellini, V. Balzani, L. De Cola, F. Vögtle, *J. Am. Chem. Soc.* **1998**, *120*, 12187–12191.
- [5] a) B. S. Lukyanov, M. B. Lukyanova, *Chem. Heterocycl. Compd.* **2005**, *41*, 281–311; b) A. Kocer, M. Walko, W. Meijberg, B. L. Feringa, *Science* **2005**, *309*, 755–758; c) O. Ivashenko, J. T. van Herpt, B. L. Feringa, P. Rudolf, W. R. Browne, *Langmuir* **2013**, *29*, 4290–4297; d) J. Kohl-Landgraf, M. Braun, C. Ozcoban, D. P. Goncalves, A. Heckel, J. Wachtveitl, *J. Am. Chem. Soc.* **2012**, *134*, 14070–14077.
- [6] a) M. Irie, *Phosphorus Sulfur Silicon Relat. Elem.* **1997**, *120*, 95–106; b) M. F. Budyka, *Russ. Chem. Rev.* **2012**, *81*, 477–493; c) H. Cahová, A. Jäschke, *Angew. Chem.* **2013**, *125*, 3268–3272; *Angew. Chem. Int. Ed.* **2013**, *52*, 3186–3190; d) H. Ohara, M. Morimoto, M. Irie, *Photochem. Photobiol. Sci.* **2010**, *9*, 1079–1081.
- [7] L. S. S. Reamonn, W. I. O'Sullivan, *J. Chem. Soc. Perkin Trans. 1* **1977**, 1009–1012.
- [8] a) T. Yamaguchi, T. Seki, T. Tamaki, K. Ichimura, *Bull. Chem. Soc. Jpn.* **1992**, *65*, 649–656; b) K. Ichimura, T. Seki, T. Tamaki, T. Yamaguchi, *Chem. Lett.* **1990**, *9*, 1645–1646.
- [9] a) T. Loughheed, V. Borisenko, T. Hennig, K. Rück-Braun, G. A. Woolley, *Org. Biomol. Chem.* **2004**, *2*, 2798–2801; b) K. Eggers, T. M. Fyles, P. J. Montoya-Pelaez, *J. Org. Chem.* **2001**, *66*, 2966–2977; c) N. Regner, T. T. Herzog, K. Haiser, C. Hoppmann, M. Beyermann, J. Saueremann, M. Engelhard, T. Cordes, K. Rück-Braun, W. Zinth, *J. Phys. Chem. B* **2012**, *116*,

- 4181–4191; d) T. Cordes, D. Weinrich, S. Kempa, K. Riesselmann, S. Herre, C. Hoppmann, K. Rück-Braun, W. Zinth, *Chem. Phys. Lett.* **2006**, *428*, 167–173; e) T. Cordes, C. Elsner, T. T. Herzog, C. Hoppmann, T. Schadendorf, W. Summerer, K. Rück-Braun, W. Zinth, *Chem. Phys.* **2009**, *358*, 103–110.
- [10] a) K. Tanaka, K. Kohayakawa, S. Iwata, T. Irie, *J. Org. Chem.* **2008**, *73*, 3768–3774; b) H. Dube, J. Rebek, Jr., *Angew. Chem. Int. Ed.* **2012**, *124*, 3261–3264; *Angew. Chem.* **2012**, *124*, 3261–3264; *Angew. Chem. Int. Ed.* **2012**, *51*, 3207–3210; c) K. Tanaka, K. Taguchi, S. Iwata, T. Irie, *Supramol. Chem.* **2005**, *17*, 637–642.
- [11] S. Herre, T. Schadendorf, I. Ivanov, C. Herrberger, W. Steinle, K. Rück-Braun, R. Preissner, H. Kuhn, *ChemBioChem* **2006**, *7*, 1089–1095.
- [12] A. Nenov, T. Cordes, T. T. Herzog, W. Zinth, R. de Vivie-Riedle, *J. Phys. Chem. A* **2010**, *114*, 13016–13030.
- [13] a) A. Nenov, R. de Vivie-Riedle, *J. Chem. Phys.* **2012**, *137*, 074101; b) A. Nenov, R. de Vivie-Riedle, *J. Chem. Phys.* **2011**, *135*, 034304; c) G. Tomasello, M. J. Bearpark, M. A. Robb, G. Orlandi, M. Garavelli, *Angew. Chem.* **2010**, *122*, 2975–2978; *Angew. Chem. Int. Ed.* **2010**, *49*, 2913–2916; d) M. F. Rode, A. L. Sobolewski, *J. Chem. Phys.* **2014**, *140*, 084301.
- [14] J. Saltiel, J. T. D'Agostino, *J. Am. Chem. Soc.* **1972**, *94*, 6445–6456.
- [15] a) D. H. Waldeck, *J. Mol. Liq.* **1993**, *57*, 127–148; b) K. Rechthaler, G. Köhler, *Chem. Phys. Lett.* **1996**, *250*, 152–158.
- [16] a) V. Papper, D. Pines, G. Likhtenshtein, E. Pines, *J. Photochem. Photobiol. A* **1997**, *111*, 87–96; b) I. Gryczynski, A. Kowski, Z. Gryczynski, D. Gloyna, *J. Chem. Soc. Faraday Trans. 2* **1986**, *82*, 1879–1884.
- [17] B. Schmidt, C. Sobotta, S. Malkmus, S. Laimgruber, M. Braun, W. Zinth, P. Gilch, *J. Phys. Chem. A* **2004**, *108*, 4399–4404.
- [18] a) T. Cordes, T. Schadendorf, B. Prieuwisch, K. Rück-Braun, W. Zinth, *J. Phys. Chem. A* **2008**, *112*, 581–588; b) T. Cordes, T. Schadendorf, K. Rück-Braun, W. Zinth, *Chem. Phys. Lett.* **2008**, *455*, 197–201.
- [19] a) W. Holzappel, U. Finkle, W. Kaiser, D. Oesterhelt, H. Scheer, H. U. Stolz, W. Zinth, *Proc. Natl. Acad. Sci. USA* **1990**, *87*, 5168–5172; b) T. Cordes, B. Heinz, N. Regner, C. Hoppmann, T. E. Schrader, W. Summerer, K. Rück-Braun, W. Zinth, *ChemPhysChem* **2007**, *8*, 1713–1721.
- [20] H. Mayr, T. Bug, M. F. Gotta, N. Hering, B. Irrgang, B. Jancker, B. Kempf, R. Loos, A. R. Ofial, G. Remennikov, H. Schimmel, *J. Am. Chem. Soc.* **2001**, *123*, 9500–9512.
- [21] E. Riedle, M. Beutter, S. Lochbrunner, J. Piel, S. Schenkl, S. Spörlein, W. Zinth, *Appl. Phys. B* **2000**, *71*, 457–465.
- [22] R. Huber, H. Satzger, W. Zinth, J. Wachtveitl, *Opt. Commun.* **2001**, *194*, 443–448.
- [23] M. J. Frisch, G. W. Trucks, H. B. Schlegel, G. E. Scuseria, M. A. Robb, J. R. Cheeseman, G. Scalmani, V. Barone, B. Mennucci, G. A. Petersson, H. Nakatsuji, M. Caricato, X. Li, H. P. Hratchian, A. F. Izmaylov, J. Bloino, G. Zheng, J. L. Sonnenberg, M. Hada, M. Ehara, K. Toyota, R. Fukuda, J. Hasegawa, M. Ishida, T. Nakajima, Y. Honda, O. Kitao, H. Nakai, T. Vreven, J. Montgomery, J. A., J. E. Peralta, F. Ogliaro, M. Bearpark, J. J. Heyd, E. Brothers, K. N. Kudin, V. N. Staroverov, R. Kobayashi, J. Normand, K. Raghavachari, A. Rendell, J. C. Burant, S. S. Iyengar, J. Tomasi, M. Cossi, N. Rega, J. M. Millam, M. Klene, J. E. Knox, J. B. Cross, V. Bakken, C. Adamo, J. Jaramillo, R. Gomperts, R. E. Stratmann, O. Yazyev, A. J. Austin, R. Cammi, C. Pomelli, J. W. Ochterski, R. L. Martin, K. Morokuma, V. G. Zakrzewski, G. A. Voth, P. Salvador, J. J. Dannenberg, S. Dapprich, A. D. Daniels, Ö. Farkas, J. B. Foresman, J. V. Ortiz, J. Cioslowski, D. J. Fox, Gaussian, Inc., Wallingford CT, **2009**.
- [24] a) H.-J. Werner, P. J. Knowles, G. Knizia, F. R. Manby, M. Schütz, *WIREs Comput. Mol. Sci.* **2012**, *2*, 242–253; b) H.-J. Werner, P. J. Knowles, G. Knizia, F. R. Manby, M. Schütz, P. Celani, T. Korona, R. Lindh, A. Mitrushenkov, G. Rauhut, K. R. Shamasundar, T. B. Adler, R. D. Amos, A. Bernhardsson, A. Berning, D. L. Cooper, M. J. O. Deegan, A. J. Dobbyn, F. Eckert, E. Goll, C. Hampel, A. Hesselmann, G. Hetzer, T. Hrenar, G. Jansen, C. Köppl, Y. Liu, A. W. Lloyd, R. A. Mata, A. J. May, S. J. McNicholas, W. Meyer, M. E. Mura, A. Nicklass, D. P. O'Neill, P. Palmieri, D. Peng, K. Pflüger, R. Pitzer, M. Reiher, T. Shiozaki, H. Stoll, A. J. Stone, R. Tarroni, T. Thorsteinsson, M. Wang, **2012**.

---

Received: May 23, 2014

Published online on September 11, 2014

## 2.2 Blocking the passage: Photostability of 4,4'-dihydroxythioindigo

Indigo is mostly known for its use as dye. One important property for this purpose, its photostability has been attributed to an excited state intramolecular proton transfer (ESIPT) occurring between the two moieties [54]. The ESIPT opens a channel for an efficient and ultrafast relaxation to the groundstate which leads back to the product structure. Unlike indigo, its derivative thioindigo shows isomerization around the central double bond and strong fluorescence, which is in agreement with this explanation. In the present study, it is shown, that an ESIPT can provide a possible relaxation channel even if it is located on only one of the fragments for 4,4'-dihydroxythioindigo.

Relating to substituent effects on the photorelaxation, it can be seen that, even if both, the electronic situation at the FC does not vary significantly, and the CoIn of a decay channel remains energetically below the FC energy, the passage can be obstructed nonetheless. Replacing the hydrogen atom responsible for the ESIPT by a methyl group blocks the transfer of the substituent and the CoIn can not be reached anymore.

In the following, the article "Photostability of 4,4'-Dihydroxythioindigo a mimetic of indigo", *Angew. Chem. Int. Ed.* **53** (2014), 591, is reprinted with the permission of John Wiley and Sons. The supplementary information is available under [dx.doi.org/10.1002/anie.201307016](https://dx.doi.org/10.1002/anie.201307016). Key points of the article are:

- 4,4'-Dihydroxythioindigo and 4,4'-dimethoxythioindigo were synthesized and their transient absorption and fluorescence were measured. The dimethoxy derivate exhibits significantly longer excited state lifetimes.
- Critical points of a relaxation pathway were quantum chemically determined. The pathway involves an ESIPT, which, for the methoxy substituted moiety is obstructed by a substantial barrier on the PES. This confirms the measurements.
- The mixedly substituted thioindigo was synthesized and found to behave comparable to the dihydroxy derivate, which confirms the theoretical interpretation.

## Indigo Mimetic

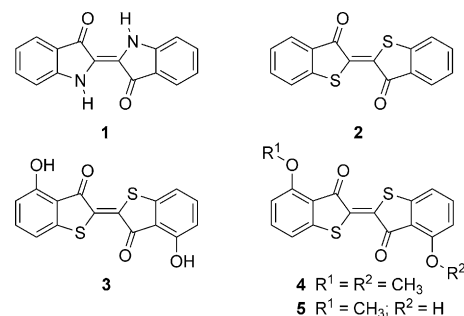
DOI: 10.1002/anie.201307016

## Photostability of 4,4'-Dihydroxythioindigo, a Mimetic of Indigo\*\*

Marc Dittmann, Franziska F. Graupner, Benjamin Maerz, Sven Oesterling,  
Regina de Vivie-Riedle, Wolfgang Zinth,\* Martin Engelhard,\* and Wolfgang Lüttke

**Abstract:** The photochemical properties of indigo, a widely used industrial dye, has attracted both experimentalists and theoreticians from the beginning. Especially the high photostability of indigo has been the subject of intensive research. Recently, it was proposed that after photoexcitation an intramolecular proton transfer followed by a nonradiative relaxation to the ground state promote photostability. In indigo the hydrogen bond and the proton transfer occur between the opposing hemiindigo parts. Here, we provide experimental and theoretical evidence that a hydrogen transfer within one hemiindigo or hemithioindigo part is sufficient to attain photostability. This concept can serve as an interesting strategy towards new photostable dyes for the visible part of the spectrum.

Indigo (**1**) has been used as brilliant dye for centuries. After the determination of its structure and its chemical synthesis by Adolf von Baeyer,<sup>[1]</sup> indigo was and still is produced industrially because of its characteristic color and most importantly its high photostability. In recent times new applications have been proposed for this “old” dye. For example, an ambipolar organic field-effect transistor on the basis of indigo has been developed.<sup>[2]</sup> Derivatives of indigo like hemithioindigo<sup>[3]</sup> are promising tools in the competitive field of chemical optogenetics.<sup>[4]</sup>



The photochemical properties of indigo, for example its long-wavelength absorption maximum and its photostability, have attracted the interest of experimentalists as well as theoreticians from the beginning and have resulted in an abundance of publications over the past decades. Quite early on, in theoretical studies using LCAO molecular orbital calculations (LCAO = linear combination of atomic orbitals) a basic chromophore structure of indigo was proposed<sup>[5]</sup> which was later confirmed by chemical synthesis.<sup>[6]</sup>

The photostability of indigo was attributed originally to the lack of *trans*–*cis* photoisomerization.<sup>[7]</sup> In contrast, indigo derivatives like thioindigo (**2**) readily isomerize about the central double bond<sup>[8]</sup> and, unlike indigo, show strong fluorescence.<sup>[9]</sup> It was proposed that the *trans* isomer of indigo is stabilized by hydrogen bonds formed between the NH and CO groups connecting the two halves of the molecule.<sup>[7,10]</sup> It was also discussed that after photoexcitation an intramolecular proton transfer followed by a nonradiative relaxation to the ground state occurs.<sup>[11]</sup> However, in picosecond infrared experiments Elsaesser et al. detected only small changes and they concluded that a proton transfer does not occur in the S<sub>1</sub> state.<sup>[12]</sup> Recent work reexamined indigo photochemistry. Iwakura et al.<sup>[13]</sup> reported on the fast photoexcited proton transfer which should occur on the femtosecond time scale. Interestingly the back reaction should be completed already at 0.5 ps, which explains the results of Elsaesser et al.<sup>[12]</sup> Computational analysis on the photostability of indigo addressed the role of isomerization and excited-state proton transfer and found that rapid internal conversion is induced by intramolecular single-proton transfer.<sup>[14]</sup> In indigo the hydrogen bond and the proton transfer occur between the opposing hemiindigo parts. The question whether a hydrogen transfer within one hemiindigo (HI) or hemithioindigo part would be sufficient to ascertain photostability is addressed herein.

Here we report on the synthesis and photophysical properties of the newly synthesized 4,4'-dihydroxythioindigo as well as 4,4'-dimethoxythioindigo (**3**), which was first

[\*] M. Dittmann, Prof. Dr. M. Engelhard  
Max Planck Institute of Molecular Physiology  
Otto-Hahn-Strasse 11, 44227 Dortmund (Germany)  
E-mail: martin.engelhard@mpi-dortmund.mpg.de  
F. F. Graupner, B. Maerz, Prof. Dr. W. Zinth  
Faculty of Physics and Center for Integrated Protein Science CIPSM  
Ludwig-Maximilians-Universität München  
Oettingenstrasse 67, 80538 München (Germany)  
E-mail: wolfgang.zinth@physik.uni-muenchen.de  
S. Oesterling, Prof. Dr. R. de Vivie-Riedle  
Department of Chemistry  
Ludwig-Maximilians-Universität München (Germany)  
Prof. Dr. W. Lüttke  
Institut für Organische und Biomolekulare Chemie  
Georg-August-Universität Göttingen  
Tammanstrasse 4, 37077 Göttingen (Germany)

[\*\*] This work was supported by the DFG through the SFB “Dynamics and intermediates of molecular transformations” (SFB 749, A5 and C2) and the Cluster of Excellence “Munich Center for Advanced Photonics” (MAP). W.Z. and F.F.G. thank C. Nehls for help with the time-resolved emission experiments. Scholarships from the International Max Planck Research School (IMPRS) in Chemical Biology and the Studienstiftung des deutschen Volkes are gratefully acknowledged (M.D.).

Supporting information for this article (including full experimental details) is available on the WWW under <http://dx.doi.org/10.1002/anie.201307016>.

prepared by Friedländer.<sup>[15]</sup> The spectroscopic properties of these compounds are similar to those of indigo (**1**) and thioindigo (**2**), respectively. Like indigo, 4,4'-dihydroxythioindigo does not undergo photoisomerization and displays a fast internal proton transfer. However, the possible proton transfer occurs only within the hemithioindigo units.

4,4'-Dihydroxyindigo (**3**) and its dimethyl ether **4** were synthesized in six and five steps, respectively, using a strategy proven successful for the synthesis of thioindoxyls.<sup>[16,17]</sup> Oxidation of thioindoxyls resulted in the formation of the thioindigo derivatives with overall yields of 25% for **3** and 30% for **4**. 4-Methoxy-4'-hydroxythioindigo (**5**) was obtained by partial hydrolysis of (**4**) and purified by thin-layer chromatography (see the Supporting Information).

Stationary irradiation experiments yielded the following results. Table 1 summarizes the results from long-term irradiation experiments. The samples were illuminated with a lamp (15 W) equipped with a yellow filter (for experimental

**Table 1:** Photoisomerization of indigo dyes in different solvents.<sup>[a]</sup>

	DMSO	DMF	CHCl <sub>3</sub>	Benzene
Thioindigo	–	–	+	+
4,4'-Dimethoxythioindigo	+	+	–	+
4,4'-Dihydroxythioindigo	–	–	–	–
Indigo	–	–	–	–
4-Methoxy-4'-hydroxythioindigo	–	n.d.	–	n.d.

[a] “+”: photoisomerization *trans*→*cis*; “–”: no photoisomerization *trans*→*cis*; n.d.: not determined.

details and use of another irradiation system see the Supporting Information). As expected, indigo (**1**) was photostable after 2 h of irradiation. Even after six weeks of exposure to daylight dihydroxythioindigo (**3**) showed no detectable signs of decomposition. A *trans*–*cis* isomerization yielding a stable product was not observed. In contrast, under identical conditions the dimethoxy derivative **4** and thioindigo (**2**) decomposed completely. In addition, the fluorescence of **3** and **5** was considerably weaker than that of **2** and **4**. Interestingly, isomerization of thioindigo (**2**) and dimethoxythioindigo (**4**) is quite dependent on the solvent (Table 1). Generally, more polar solvents inhibit *trans*–*cis* isomerization. When a strong acid (trifluoroacetic acid, TFA) was added to a solution of thioindigo, practically no isomerization was observed after two hours.

The strong change in fluorescence intensity is directly related to the lifetime of the light-emitting S<sub>1</sub> state, as can be seen from the time dependence of the fluorescence emission recorded with a streak camera (Figure 1 a, light red and light blue symbols; for experimental details see the Supporting Information). For compound **4** we observe a decay of the fluorescence emission with a time constant of approximately 11 ns (dots). The decay time of compound **3** of 50 ps (triangles) is roughly 200 times faster. Data recorded at 618 nm (**4**) and 597 nm (**3**) show that the absorption transients evolve with the same decay times as those found for fluorescence emission (Figure 1 a). Additional information was obtained from time-resolved absorption spectra recorded at distinct delay times. The transient difference spectra of

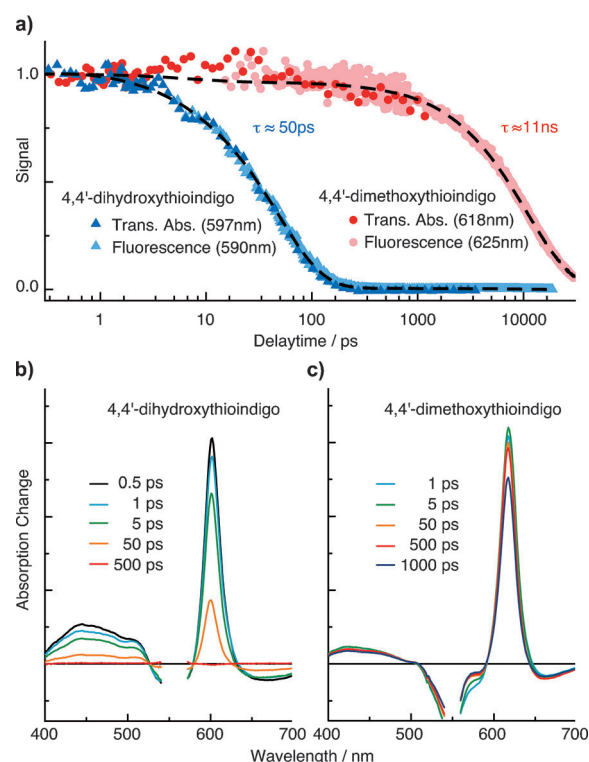


**Figure 1.** a) Time-dependent absorption change (Trans. Abs., red, blue) and fluorescence emission (light red and light blue) for **4** (red) and **3** (blue). b, c) Transient absorption difference data for the two compounds. Excitation wavelengths 525 nm (emission) and 550 nm (absorption experiments). For details of the experiments see the Supporting Information.

compound **3** (Figure 1 b) evolve on the picosecond time scale and finally disappear with the same time constant (50 ps) as that found for the decay of the excited electronic state. No absorption change remains at later times. At early times the transient absorption spectrum displays a strong and narrow peak at 600 nm due to excited-state absorption. A weaker and broader excited-state absorption band is found in the blue part of the spectrum around 430 nm. At longer wavelengths (630–700 nm) stimulated emission is visible and around 550 nm, the bleaching of the original ground state absorption is found. A global fitting procedure reveals additional absorption dynamics with a time constant of roughly 8 ps, which can be related to motions on the excited-state potential energy surface away from the originally populated Franck–Condon region.

Dimethoxythioindigo (**4**) shows very similar spectral features in the excited electronic state. Again there is a pronounced excited-state absorption peak for compound **4** at 618 nm. The decay of the absorption changes occurs much slower than in compound **3**. This long-term behavior can be well fitted with the same time constant as that found in the emission experiments.

The experiments on the two thioindigo compounds are summarized as follows: Dihydroxythioindigo (**3**) has higher photostability, a much shorter excited-state lifetime, and a weaker fluorescence quantum yield than dimethoxythioindigo (**4**). The excited electronic state of both compounds,



which is reached after 8 ps, shows very similar absorption and emission spectra. The major difference in the two molecules is the lifetime of this state. No indication of a long-lasting absorption change is found for compound **3**. Apparently isomerization at the central double bond of the molecule does not take place. Since compounds **3** and **4** differ only by the substitution at positions 4 and 4', the hydroxy group and a transient proton transfer as suggested for indigo should play a major role in the differences in photostability and reaction dynamics. The nearly identical features of the excited-state spectra of the two compounds suggest that the first relaxation out of the Franck–Condon region leads to similar intermediate states. A reaction along the proton-transfer coordinate of compound **3** should only occur afterwards and mediates the relaxation out of the  $S_1$  state. For dimethoxythioindigo (**4**) the methyl group prevents this reaction path and relaxation to the ground state occurs predominantly by fluorescence emission. The long lifetime of the  $S_1$  state may also increase the importance of other, destructive decay routes in compound **4**.

To support these qualitative interpretations, quantum-chemical computations were performed on suitable model molecules (for details see the Supporting Information). For both model molecules a conical intersection with the ground-state surface is found, located slightly below the energy at the Franck–Condon geometry. To reach this conical intersection the molecules must undergo a proton/methyl cation transfer and an out-of-plane deformation of the phenyl ring. The methyl cation transfer (red line), however, involves a large barrier ( $TS_{scan}$ ), which obstructs access to this conical intersection. In contrast, the proton transfer (blue line) occurs without a barrier in the model system and exhibits only a small barrier in the full system (compound **3**). Thus theoretical modeling indicates that both molecules **3** and **4** leave the Franck–Condon range in the direction of a nearby local minimum ( $Min_{S1}$ ) on the  $S_1$  potential surface due to the rearrangement of the  $\pi$  system. Only for compound **3** is the conical intersection accessible after passing the global minimum on  $S_1$  ( $MinP_{S1}$ ; see Figure 2). The shape of the potential energy surfaces in the vicinity of this conical intersection guides the molecule back to the planar structure. Back transfer of the proton from a first and shallow local ground-state minimum ( $MinP_{S0}$ ) completes the photophysical process. For compound **4** the large barrier in the  $S_1$  state prohibits access to the conical intersection, the excited electronic state becomes long-lived, and a high fluorescence quantum yield results.

A direct consequence of the long lifetime of the excited electronic state of compound **4** is the possibility that slow and destructive reaction channels in the nanosecond time domain may gain importance. Another implication may be photodecomposition induced by the absorption of another photon during the long population of the  $S_1$  state. The possibility of an excited-state proton transfer in compound **3** opens a new path for internal conversion, shortens the lifetime of the excited electronic state, and finally leads to the observed large gain in photostability.

The vastly different photochemical properties of the two thioindigo compounds **3** and **4** demonstrate that excited-state proton transfer within the rigid ring system of only one

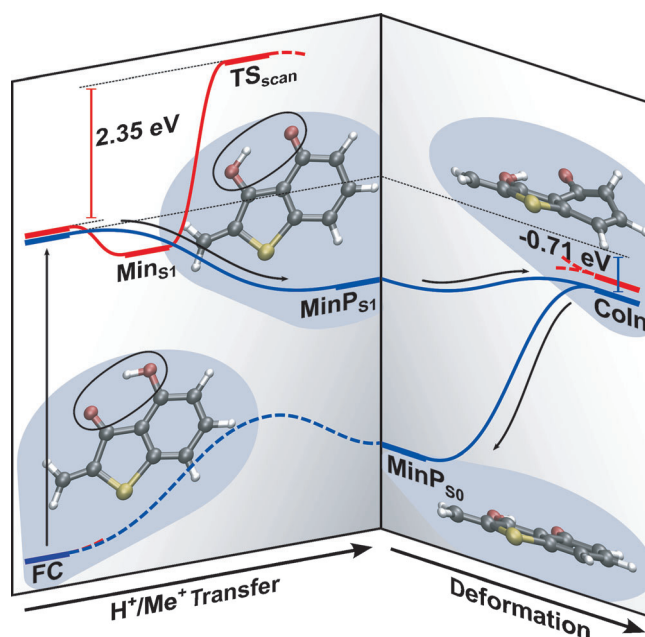


**Figure 2.** Critical points of the ground- and excited-state potential energy surfaces for the photoreaction of model systems of **3** and **4**. The process is illustrated along two reaction coordinates, the proton transfer or methyl cation transfer and the out-of-plane deformation of the phenyl ring. Although both conical intersections (Coln) are situated energetically below the Franck–Condon point (FC), the Coln can only be reached by compound **3**. The excited-state intramolecular proton/methyl<sup>+</sup> transfer is prerequisite to reach the Coln. In compound **4** the related methyl cation transfer is hindered by a substantial barrier.

hemithioindigo moiety improves photostability. To prove this point the monomethoxy derivative of thioindigo (**5**) was synthesized by partial hydrolysis of **4**. Indeed, the photostability of **5** in  $CHCl_3$  was comparable to that of dihydroxythioindigo (**3**). No photo-isomerization was found and the fluorescence emission was as weak as that of **3** (see the Supporting Information). The basic promoting mechanism—excited-state proton transfer—is the same as that in indigo and in many UV stabilizers (see Ref. [18] for the photochemistry of highly photostable compounds). However, the results on **3** show that suitably arranged proton donating and accepting groups promote excited-state proton transfer even if they are within rigid ring systems. This concept can serve as an interesting strategy towards new photostable dyes for the visible part of the spectrum.

Received: August 9, 2013

Revised: September 27, 2013

Published online: November 26, 2013

**Keywords:** dyes/pigments · photochemistry · proton transfer · thioindigo · ultrafast spectroscopy

[1] A. Baeyer, A. Emmerling, *Ber. Dtsch. Chem. Ges.* **1870**, *3*, 514–517.

[2] M. Irimia-Vladu, E. D. Glowacki, P. A. Troshin, G. Schwabegger, L. Leonat, D. K. Susarova, O. Krystal, M. Ullah, Y. Kanbur,

- M. A. Bodea, V. F. Razumov, H. Sitter, S. Bauer, N. S. Sariciftci, *Adv. Mater.* **2012**, *24*, 375–380.
- [3] N. Regner, T. T. Herzog, K. Haiser, C. Hoppmann, M. Beyer-  
mann, J. Sauermann, M. Engelhard, T. Cordes, K. Rück-Braun,  
W. Zinth, *J. Phys. Chem. B* **2012**, *116*, 4181–4191.
- [4] T. Fehrentz, M. Schönberger, D. Trauner, *Angew. Chem.* **2011**,  
*123*, 12362–12390; *Angew. Chem. Int. Ed.* **2011**, *50*, 12156–  
12182.
- [5] M. Klessinger, W. Lüttke, *Tetrahedron* **1963**, *19* (Suppl. 2), 315–  
335.
- [6] W. Lüttke, H. Hermann, M. Klessinger, *Angew. Chem.* **1966**, *78*,  
638–639; *Angew. Chem. Int. Ed. Engl.* **1966**, *5*, 598–599.
- [7] W. R. Brode, E. G. Pearson, G. M. Wyman, *J. Am. Chem. Soc.*  
**1954**, *76*, 1034–1036.
- [8] G. M. Wyman, W. R. Brode, *J. Am. Chem. Soc.* **1951**, *73*, 1487–  
1493.
- [9] G. Haucke, R. Paetzold, *Nova Acta Leopoldina, Supplement 11*,  
**1978**.
- [10] W. Madelung, O. Wilhelmi, *Ber. Dtsch. Chem. Ges.* **1924**, *57*,  
234–241.
- [11] G. M. Wyman, *J. Chem. Soc. D* **1971**, 1332–1334.
- [12] T. Elsaesser, W. Kaiser, W. Lüttke, *J. Phys. Chem.* **1986**, *90*,  
2901–2905.
- [13] I. Iwakura, A. Yabushita, T. Kobayashi, *Chem. Phys. Lett.* **2010**,  
*484*, 354–357.
- [14] S. Yamazaki, A. L. Sobolewski, W. Domcke, *Phys. Chem. Chem.*  
*Phys.* **2011**, *13*, 1618–1628.
- [15] P. Friedländer, *Ber. Dtsch. Chem. Ges.* **1916**, *49*, 955–966.
- [16] C. Mukherjee, A. De, *Synlett* **2002**, 325–327.
- [17] C. Mukherjee, S. Kamila, A. De, *Tetrahedron* **2003**, *59*, 4767–  
4774.
- [18] P. F. McGarry, S. Jockusch, Y. Fujiwara, N. A. Kaprinidis, N. J.  
Turro, *J. Phys. Chem. A* **1997**, *101*, 764–767.
-

## 2.3 The CoIn: Relaxation dynamics of furan, furfural and $\beta$ -furfural

Furan is a basic building block of many larger compounds. In the present study, furan, together with its derivatives furfural, an important, renewable chemical feedstock and  $\beta$ -furfural, serve as model systems to investigate the influence of substituents on CoIns. Furfural and  $\beta$ -furfural have an aldehyde group attached in  $\alpha$ - and  $\beta$ -position, respectively. Depending on its location, the electronic influence on the degenerating states of one of the  $S_1/S_0$  CoIns of furan differs. Thereby the geometry of the CoIn is altered in two different directions. Although the study shows, that in the end, the electronic effect at the FC point outweighs this for the example of furan, it is still apparent, that CoIns are crucial points, which could be altered to control photoprocesses. Most importantly in this regard, it is shown, how the extended two-electron two-orbital model [55, 56] can be used to even predict structural implications on CoIns when introducing substituents.

In the following, the article “Substituent effects on the relaxation dynamics of furan, furfural and  $\beta$ -furfural: a combined theoretical and experimental approach”, *Phys. Chem. Chem. Phys.* **19** (2017), 2025, is reprinted with permission from the PCCP Owner Societies. At [www.rsc.org/suppdata/c6/cp/c6cp06240g/c6cp06240g1.pdf](http://www.rsc.org/suppdata/c6/cp/c6cp06240g/c6cp06240g1.pdf) the supplementary information is available. Key points of the article are:

- The photorelaxation of furan was investigated experimentally using time resolved photoelectron spectroscopy, as well as theoretically by quantum chemical computations of critical points and semiclassical dynamics simulations. The time resolved photoelectron spectroscopy was performed with a high intensity probe pulse, which allowed to follow the whole relaxation of furan in the two photon probe signal. The evolution of the signal was attributed to two distinct processes, namely the movement of the wavepacket on the excited state PES, and the subsequent decay to the GS. The dynamics simulations showed two involved decay channels, a ring opening, and a puckering of furan.
- Using the extended two-electron two-orbital model, the  $S_1/S_0$  CoIn of the puckering pathway was analyzed in detail and implications on the effects of the substituent patterns of furfural and  $\beta$ -furfural on the CoIn were proposed.
- Quantum chemical calculations on furfural and  $\beta$ -furfural were performed, which confirm the geometrical predictions of the model. In agreement with experiments, they show, however, that further adjustment had to be made, to outweigh the simultaneous impact on the relaxation process, via the FC region.
- Theory and experiment combined, model the photorelaxation of furfural and  $\beta$ -furfural. Compared to furan, in both molecules an additional pathway is opened up by the aldehyde group.



Cite this: DOI: 10.1039/c6cp06240g

## Substituent effects on the relaxation dynamics of furan, furfural and $\beta$ -furfural: a combined theoretical and experimental approach†

Sven Oesterling,<sup>a</sup> Oliver Schalk,<sup>b</sup> Ting Geng,<sup>b</sup> Richard D. Thomas,<sup>b</sup> Tony Hansson<sup>b</sup> and Regina de Vivie-Riedle\*<sup>a</sup>

For the series furan, furfural and  $\beta$ -furfural we investigated the effect of substituents and their positioning on the photoinduced relaxation dynamics in a combined theoretical and experimental approach. Using time resolved photoelectron spectroscopy with a high intensity probe pulse, we can, for the first time, follow the whole deactivation process of furan through a two photon probe signal. Using the extended 2-electron 2-orbital model [Nenov *et al.*, *J. Chem. Phys.*, 2011, **135**, 034304] we explain the formation of one central conical intersection and predict the influence of the aldehyde group of the derivatives on its geometry. This, as well as the relaxation mechanisms from photo-excitation to the final outcome was investigated using a variety of theoretical methods. Complete active space self consistent field was used for on-the-fly calculations while complete active space perturbation theory and coupled cluster theory were used to accurately describe critical configurations. Experiment and theory show the relaxation dynamics of furfural and  $\beta$ -furfural to be slowed down, and together they disclose an additional deactivation pathway, which is attributed to the  $n_{\text{O}}$  lonepair state introduced with the aldehyde group.

Received 9th September 2016,  
Accepted 14th December 2016

DOI: 10.1039/c6cp06240g

www.rsc.org/pccp

## 1 Introduction

A general quest in chemistry is to find rules and correlations which can be used to describe, or, even better, predict properties and behaviours of molecular systems. In photo processes, substituents can not only influence the excitation energy, but also the conical intersections (CoIns) of a molecule, which are the sensitive regions for ultrafast population transfer between electronic states, and thus play a crucial role in most deactivation processes. This work investigates the relaxation pathways of photoexcited furan and two of its derivatives, furfural and  $\beta$ -furfural, which have an aldehyde group substituted in  $\alpha$ - and  $\beta$ -position (Fig. 1). For all three molecules, new theoretical and experimental data are provided. We discuss the influence of the substituent and of its positioning on the whole reaction path. Recently, it was shown that the energetic position and the geometry of CoIns can systematically be influenced by substituents.<sup>1–3</sup>

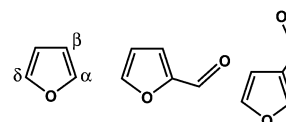


Fig. 1 Furan and its derivatives furfural and  $\beta$ -furfural.

Thus, one focus of our study is, to explain such influences for our series of molecules by the extended 2-electron-2-orbital model.<sup>1,2</sup> The substituent effects of furfural and  $\beta$ -furfural are predicted by the model for the ring puckering CoIn, one prominent relaxation pathway, and are verified by quantum chemical calculations.

A number of studies on the photorelaxation of furan has previously been performed.<sup>4–9</sup> Two possible relaxation pathways have been reported,<sup>4</sup> ring opening of the CO-bond, also known from related molecules like thiophene,<sup>5</sup> and ring puckering, which features a CoIn with a puckered structure with, most notably, the H-atom in either  $\alpha$ - or  $\delta$ -position being bent out of the ring plane. The opening has the energetically lower lying  $S_1/S_0$  CoIn. However, dynamics simulations result in long lifetimes for wavepacket-dynamics on EOM-CCSD surfaces in reduced dimensions,<sup>8,9</sup> or exclusively choose the second pathway in on-the-fly dynamics on TDDFT level of theory.<sup>6</sup>

The experimental observation of the whole relaxation is challenging due to the high probe energies needed. Two velocity

<sup>a</sup> Department of Chemistry, Ludwig-Maximilians-Universität München, Butenandtstr. 5-13, 81377 München, Germany.  
E-mail: Regina.de\_Vivie@cup.uni-muenchen.de; Fax: +49-89-2180-77133;  
Tel: +49-89-2180-77533

<sup>b</sup> Department of Physics, Stockholm University, AlbaNova University Centre, Roslagstullsbacken 21, 106 91 Stockholm, Sweden

† Electronic supplementary information (ESI) available. See DOI: 10.1039/c6cp06240g

map imaging studies were reported previously. One covered the initial part of the relaxation.<sup>6</sup> Here the constant photoelectron anisotropy parameters for individual photoelectron kinetic energies were interpreted as an indicator for a constant electronic character of the excited wavepacket, and thus the puckering mechanism. However, the measurements were restricted to the FC region, as the ionization potential does not remain constant with changing geometry of the molecule.<sup>10,11</sup> A recent experiment with a high energetic (160 nm) probe pulse reached further into the direction of both CoIns, but the spectrum of the short-time dynamics is superimposed by the signal generated by an inverted pump and probe order.<sup>7</sup>

In the present study, we use high intensity instead of high energy for the probing pulse, in order to cover the higher energetic range *via* two photon processes and thus circumvent this problem. This way, it is possible to follow the relaxation of furan from the FC region to the CoIn. Theoretically the deactivation of the three molecules is characterized by quantum chemical calculations complemented by non-adiabatic on-the-fly dynamics, where possible. One large challenge was to adequately describe on one hand the diffuse character of electronic states in the FC-region and on the other hand the multi-reference character at the CoIns. To meet this challenge, several high-level electron correlation methods were utilized which also allowed us to benchmark the setup used for the dynamics.

## 2 Methods

### 2.1 Experimental set-up

Furan, furfural and  $\beta$ -furfural were purchased from Sigma Aldrich with nominal purities of 99%, 99% and 97%, respectively, and were used without further purification.

Absorption spectra were measured in a 1 cm quartz cell (Hellma) under saturated vapor pressure using a Cary 5e photospectrometer (Varian). Our magnetic bottle set-up and wavelength generation schemes were described before.<sup>12</sup> As pump pulses, we used the third and fourth harmonic of the fundamental 800 nm pulses of our 1 kHz-laser system (Coherent Legend USP-HE) at intensities of 700 and 300 nJ pulse<sup>-1</sup>. As a probe, we used the second or the third harmonic at intensities of 6 and 1.4  $\mu$ J pulse<sup>-1</sup>. The cross correlation of our pulses varied between  $180 \pm 20$  fs for 267 + 400 nm experiments and  $150 \pm 20$  fs for 200 + 267 nm experiments as measured by the non-resonant ionization signal of Xe, which was also used for energy calibration of the spectrometer. For the experiments, the pulses were aligned collinearly and the focusing conditions were typically  $f/150$  for the pump and  $f/125$  for the probe pulse. Perpendicular to the incoming laser pulses, the molecular beam was introduced into the interaction region of our magnetic bottle spectrometer by a needle valve to which we applied a slightly negative voltage. The delay between pump and probe pulses was controlled by a stepper motor. At each delay time, the times of flight of the generated photoelectrons were recorded and the pump-probe signal was corrected by the independently measured signal for pump and probe only.

### 2.2 Data fitting

The data sets of furfural and  $\beta$ -furfural were modeled with a global fitting routine<sup>13</sup>

$$S(\Delta t, E) = \sum_i A_i(E) \int_0^\infty e^{-t/\tau_i} g(\Delta t - t_0'(E) - t) dt, \quad (1)$$

where the signal  $S(\Delta t, E)$  is a function of the delay time  $\Delta t$  and the kinetic energy  $E$ .  $A_i(E)$  are the decay associated spectra (DAS) of individual channels  $i$  characterized through the lifetimes  $\tau_i$ . They are broadened by a Gaussian cross-correlation function  $g(\Delta t - t_0'(E) - t)$ . Time zero  $t_0'(E) = t_0 + t_s(E)$  consists of two values, a globally constant starting time,  $t_0$ , which is measured in a separate experiment, and potentially a time zero shift  $t_s(E)$ . The shift  $t_s(E)$  is used as additional fitting parameter, when the spectrum shifts at different photoelectron kinetic energies, which is the case for the 2 photon probe signal of the 267 + 400 nm experiments. For the 200 + 267 nm experiments  $t_s(E)$  is set to zero, and  $t_0'(E) = t_0$ .

The data sets of furan were not fitted with a global exponential function. Instead, the different energy slices  $S_E(\Delta t)$  were fitted individually with not only  $t_s$ , but also  $\tau_1$  used as free fitting parameters in order to account for the temporal shift of the photoelectron spectrum<sup>10,11</sup> and a change of the lifetime in the different regions of the potential energy surface.<sup>11,14</sup> The temporal shift of the spectrum is caused by large amplitude motions of the molecule after photoexcitation. Along the relaxation paths, the ionization potential rises while potential energy is transformed into kinetic motion of the nuclei. Thus, when the molecules deform, the photoelectron kinetic energy decreases and the transient spectrum shifts. Therefore, for each energy trace, different lifetimes  $\tau_1$  can be observed as only parts of the dynamics are covered. At the energy where the largest shift is observed, the molecule has likely reached the energetic minimum of the potential energy surface and the decay constant measured at that point can be interpreted as the time the wavepacket needs to pass through the conical intersection back to the ground state. As a consequence, the total excited state lifetime can be considered as the maximum time shift plus the exponential decay time fitted at the energy where that shift is observed.

### 2.3 Computational details

Calculations were performed on several levels of theory to obtain a high level of accuracy for the different critical points on the potential energy surfaces, in spite of their individual demands. This kind of benchmarking also allows to rate the non-adiabatic on-the-fly dynamics simulations. Their quantum chemical description has to cover the whole potential surface. Simultaneously, it is most limited in terms of computational cost, which requires a compromise between accuracy and calculation time. We used the state averaged complete active space self consistent field (SA-CASSCF) method with 6-31G\* as basis set for the on-the-fly dynamics. The (10,9) active space for furan involves the whole  $\pi$ -system and both CO  $\sigma$ -bonds in order to describe the ring opening (Fig. 2a). For furfural and

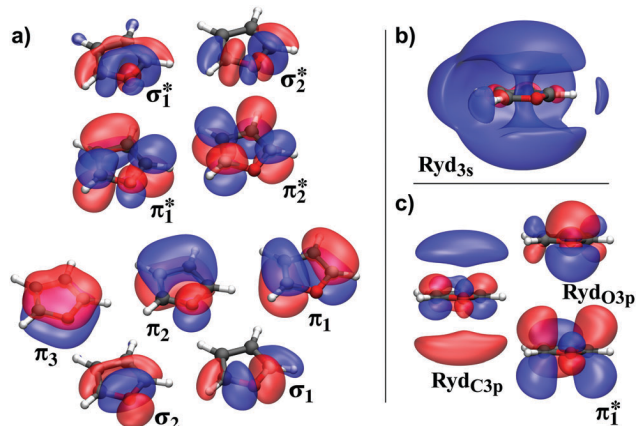


Fig. 2 Active space of furan. (a) The orbitals in the (10,9) active space used in most calculations. (b) The Ryd<sub>3s</sub> orbital, (c) two Ryd<sub>3p</sub> orbitals and the adapted  $\pi_1^*$  from (a). The isovalue chosen for all but Ryd<sub>3s</sub> is 0.03, the latter is rendered with an isovalue of 0.018. The expectation values  $\langle r^2 \rangle$  in [ $a_0^2$ ] for the orbitals are: (a)  $\pi_1^*$ : 3.82; (c)  $\pi_1^*$ : 10.11; Ryd<sub>3s</sub>: 18.68; RydC<sub>3p</sub>: 16.87; RydO<sub>3p</sub>: 4.03; see Fig. S9 in the ESI.†

$\beta$ -furfural, a (12,10) CAS was used. The additional  $\pi$  orbitals and the  $n_{\text{O}}$ -lonepair of the aldehyde group were included, in return one of the CO  $\sigma$ -bond pairs was removed to avoid too high computation times. This reduction is easily compensated as both orbitals are connected by the oxygen orbitals and can easily interchange by rotating in and out of the CAS automatically. The CO  $\sigma$ -bond can still break at both sides.

Geometry optimizations used the 6-31G\* basis set for all structures.‡ Equilibrium geometries and normal modes were obtained at CCSD(T) level of theory. CoIns between the ground and first excited state were optimized with CASSCF SA2 using the full  $\pi$ -space and both CO  $\sigma$ -orbital pairs as active space. In cases where the  $n_{\text{O}}$ -orbital does not contribute to either of the two states, it was not included in the CAS of furfural and  $\beta$ -furfural, else the active space was not stable.

In the FC region Rydberg orbitals proved to play a crucial role. In general, their presence complicates the description of the electronic states which becomes rather sensitive to the quantum chemical theories used. An extensive comparison was performed to assess results and methods at all critical points. As reference basis set, an augmented triple-zeta ANO basis,<sup>15</sup> as taken from the EMSL basis set exchange library,<sup>16,17</sup> was employed. Two smaller alternatives that also cover Rydberg orbitals were considered, 6-31+G\* as standard basis and a further reduced custom basis set. The latter was built by augmenting the 6-31G\* basis with just the diffuse p-orbitals of the 6-31+G\* basis (see Section 3.1). This basis set will further be referred to as “aug”.

The quantum chemical methods used include CASSCF, equation of motion coupled cluster singles and doubles (EOM-CCSD red, from here on referred to, as CCSD), and complete active

space perturbation theory (CASPT2) in various implementations: XMS-MSMR-RS2 (extended multistate multi reference Rayleigh Schrödinger perturbation theory, from here on referred to, as RS2) as reference, RS2C mainly to be able to compute the larger molecules, and CASPT2 as implemented in MOLCAS,<sup>18</sup> because multistate calculations were needed at some points. Apart from the latter, all quantum chemical calculations were performed with the MOLPRO2012 program package.<sup>19,20</sup>

For the non-adiabatic on-the-fly simulations our modified version of Newton-X,<sup>21,22</sup> which supports the usage of Molpro 2012<sup>23</sup> was used. For each molecule a set of 100 trajectories was started from a Wigner distribution around the ground-state equilibrium geometry and propagated for 250 fs (furan) or 500 fs (furan derivatives). The properties of the considered states were computed every 0.5 fs. The non-adiabatic coupling vectors between two states, which are used in Tully’s fewest switches surface hopping routine,<sup>24</sup> were calculated if the energy difference between the states was less or equal to 2 eV in the preceding step and else set to zero.

## 3 Furan

Furan serves as our reference to study the effect of substituents attached at different positions. We follow critical points along its possible relaxation pathways and try to find a balanced description for the electronic structure of the whole process.

### 3.1 Excited states at the Franck–Condon point

An overview about the excited states of furan at the FC point with comparison to other theoretical as well as experimental studies was given by Gavrilov *et al.* 2008.<sup>5</sup> In their work a basis set explicitly tailored for the description of the FC-region and thus of the Rydberg states is used in combination with the DFT/MRCI method, feasible only for single point calculations. Our benchmark ANO (10,10) RS2C excitation energies (Table 1) of the first  $\pi\pi^*$  excited states lie roughly 0.2 eV above the values provided in their work. The active space consists of the whole  $\pi$ -space, the CO- $\sigma$  orbitals (Fig. 2a) and a 3s-Rydberg

Table 1 Excitation energies of furan in eV for different levels of theory. The ANO basis set is an augmented triple zeta ANO-basis, taken from the EMSL-database.<sup>25,26</sup> The “aug” basis set is 6-31G\* with only the diffuse p-orbitals of 6-31+G\* added (compare Table S1 in the ESI). Experimental excitation energies are 5.91 eV for the  $\pi_1$ Ryd<sub>3s</sub> state and 6.04 eV for the  $\pi_1\pi_1^*$  state<sup>5</sup>

Dominant transition	Method	(10,10) ANO	(10,9) ANO	6-31+G*	6-31G*	(10,11) aug
$\pi_1\pi_1^*$	RS2		6.25	6.52	6.84	6.58
	RS2C	6.24	6.23	6.50	6.82	6.61
	CASSCF	7.72	7.62	7.69	8.00	6.79
$\pi_1$ Ryd <sub>3s</sub>	RS2C	6.26				
$\pi_1\pi_2^*$	RS2		6.45	6.58	6.72	6.63
	RS2C	6.44	6.41	6.55	6.68	6.59
	CASSCF	6.78	6.64	6.70	6.80	6.65

‡ Note, that the problems with the Rydberg influences, mentioned later, neither affect the ground state in the FC-region, nor the degenerate states in the region of the  $S_1/S_0$  CoIns.

orbital ( $\text{Ryd}_{3s}$ , Fig. 2b). In this basis, the  $\pi\text{Ryd}_{3s}$  state is nearly degenerate with the first  $\pi\pi^*$  state.

The influence of the  $\text{Ryd}_{3s}$ -orbital proved to be negligible for the description of the  $\pi\pi^*$  states (see Table 1 first and second column). In addition, it was found that the corresponding  $\pi\text{Ryd}_{3s}$  state does not play a crucial role in the relaxation process of furan.<sup>6</sup> To save computation time, the  $\text{Ryd}_{3s}$ -orbital is left out of the CAS and we will further focus the discussion on the  $\pi\pi^*$  states.

When using CASSCF instead of CASPT2, as done in the dynamics simulations, the order of the states changes. The excitation energy of the bright  $\pi_1\pi_1^*$  state raises significantly (see Table 1: RS2(C) vs. CASSCF). The dark  $\pi_1\pi_2^*/\pi_2\pi_1^*$  state is, in comparison, hardly affected, which results in a swap of the energetic order of the two.

Analyzing the PT2 correction shows, that the reason for the strong impact of the method on the  $\pi_1\pi_1^*$  state is its diffuse character. For CASSCF this effect can be included by increasing the basis set and the active space (also see Table S1 in the ESI<sup>†</sup>). Rotating two additional  $\text{Ryd}_{3p}$  orbitals into the CAS in the ANO or 6-31+G\* basis sets significantly improves the description of the state (Fig. 2c). In addition, the shape of the  $\pi_1^*$  orbital changes (compare Fig. 2a and c). For further improvement related to computational cost and stability, we constructed a basis set (“aug”), where we augmented the 6-31+G\* basis with only the diffuse p orbitals from 6-31+G\*. Comparing the CASSCF results of the (10,9) CAS with 6-31+G\* to the results of the (10,11) CAS with the aug basis (Table 1), the excitation energy of the latter is reduced by almost 1 eV and approaches its RS2 energies. However, for the correct ordering of the states still CASPT2 is needed.

Leaving the FC region, the diffuse character of the  $\pi_1\pi_1^*$  state decreases and the CoIns (see Section 3.3) are described well using just the 6-31G\* basis set on (10,9) CASSCF level of theory. As the (10,11) CAS even in the aug basis frequently runs into convergence issues outside the FC region, it was not used for the dynamics. Thus, the compromise for the dynamics simulations is to accept that too much energy is deposited in the molecule in the FC region.

### 3.2 Time-resolved photoelectron spectrum of furan

Photoelectron spectra of furan were recorded for two different pump–probe settings. The spectrum for the 200 nm pump and 267 nm probe (200 + 267 nm) is shown in Fig. 3 while the 200 + 400 nm spectrum is shown in the ESI.<sup>†</sup> In contrast to previous experiments,<sup>6</sup> we chose a higher probe intensity in order to use the two photon probe signal which allowed us to follow the dynamics further along the potential energy surface. The stronger one photon probe signal  $[1 + 1']$  extends from 2.1 eV to 0 eV electron kinetic energy. The electrons that form the weaker two photon probe signal have an additional kinetic energy of 4.6 eV (267 nm), the two photon probe signal  $[1 + 2']$  thus starts at 6.7 eV. The fitted  $t_s(E)$  (eqn (1)), which roughly follows the peak maximum of the photoelectron spectrum, shifts by  $60 \pm 15$  fs from the FC point (at 1.85 eV in the  $[1 + 1']$  signal) to an electron kinetic energy of 3.3 eV in the

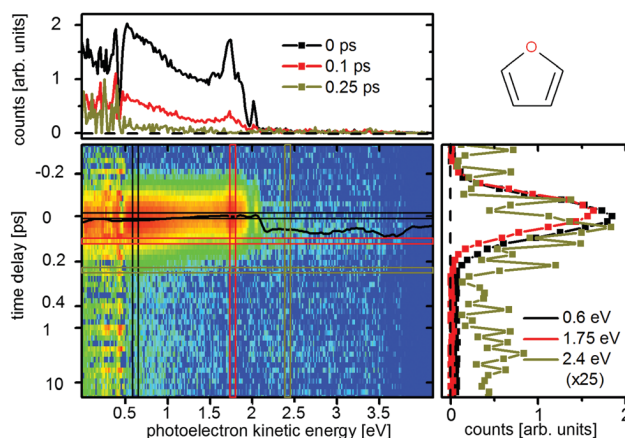


Fig. 3 Time-resolved photoelectron spectra of furan upon excitation at 200 nm and ionization at 267 nm. The black line represents the time zero shift  $t_s(E)$  as fitted by eqn (1). The cut at 2.4 eV (other) is scaled by a factor of 25.

$[1 + 2']$  signal. This shift is attributed to a motion of the wavepacket on the excited state potential energy surface towards the CoIns. From here the signal decays with a lifetime of  $110 \pm 25$  fs, which is attributed to the decay to the groundstate and the accompanying fast decrease of the potential energy of the molecules. Neither the extent of the shift nor the decay time could be monitored by previous experiments. At the energy cut-off of  $[1 + 1']$  ionization (at 2.1 eV), we fitted a time constant of  $30 \pm 15$  fs which was assigned to the lifetime of the  $\pi\text{Ryd}_{3s}$  state in accordance to Fuji *et al.*<sup>6</sup>

### 3.3 Relaxation pathways and associated $S_1/S_0$ conical intersections

Two possible relaxation pathways of furan have been described in literature.<sup>4</sup> The first is a ring puckering, where the oxygen atom moves out of the ring plane, and one of the hydrogen atoms attached in  $\alpha$  position bends far out of the plane in the opposite direction (CoIn<sub>p</sub> – Fig. 4, left). The other pathway is an opening of the ring between the oxygen atom and one of the carbon atoms (CoIn<sub>o</sub> – Fig. 4, right). Both pathways were found to be barrierless on CASSCF level of theory. Interpolations done on CCSD<sup>4</sup> and DFT/MRCI<sup>5</sup> level of theory exhibit very small barriers with an upper limit of 0.06 eV for the opening pathway. Both  $S_1/S_0$  CoIns lie below the FC-region and are thus energetically accessible. At ANO XMS-RS2 level of theory, they lie 5.0 eV (CoIn<sub>p</sub>) and 4.0 eV (CoIn<sub>o</sub>) above the ground state minimum. Literature indicates,<sup>6,8,9</sup> that the puckering probably is the main relaxation path, although its conical intersection CoIn<sub>p</sub> lies roughly 1 eV above the one of the opening pathway (CoIn<sub>o</sub>).

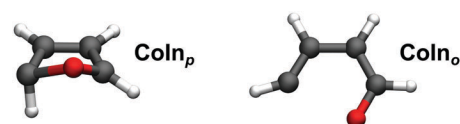


Fig. 4 Conical intersections of furan.

Our CASSCF dynamics exhibit trajectories of both channels, with the ring opening being the clear favorite. The geometries where the hops to the ground state occur, as well as the state characters at these points suggest that  $\text{CoIn}_p$  and  $\text{CoIn}_o$  are connected by a seam. Only a good half of the trajectories involving the ring opening directly jumps to the ground state at the  $\text{CoIn}$ . The rest stays in the excited state while the ring opens completely, and the large flexibility of the linear molecule allows for accessing various  $\text{CoIn}$ -structures, which were not distinguished further.

Of the 88 trajectories which reached the ground state, 43 are assigned to  $\text{CoIn}_o$ , 37 reach the ground state *via* completely opened  $\text{CoIn}$ s, and eight trajectories are assigned to  $\text{CoIn}_p$ . Two trajectories of  $\text{CoIn}_o$  and three of  $\text{CoIn}_p$  lie inbetween both structures and were assigned by inspecting orbitals and configuration interaction (CI)-vectors, to determine whether the states include mainly the  $\pi\pi^*$ -, or the  $\pi\sigma^*$ -excitation.

Most likely, the importance of the opening channel is overestimated. The small barrier along this path seemingly vanishes in CASSCF due to the shortcomings in the FC region. A frequency analysis of the  $\pi_1\pi_1^*$  state at the FC-point (Table 2) shows that the gradient in direction of the puckering is unaffected when going from RS2C to CASSCF level of theory, but the curvature in direction of the barrier of the opening path becomes much weaker. This is reflected by the decrease of the frequency of the asymmetric CO stretching mode from 1989 to 667  $\text{cm}^{-1}$ .

The excited state lifetimes, extracted from the on-the-fly dynamics, are in good agreement with the experiment. Fig. 5 shows the temporal evolution of the population dynamics of furan averaged over all 88 trajectories. The simulation is started in the  $S_2(\pi_1\pi_1^*)$  state from where the  $S_1$  state is populated almost directly. Away from the FC-region, the electronic characters of the  $S_2$  and  $S_1$  state interchange. The decay of the  $S_1(\pi_1\pi_1^*)$  state is then mediated by the  $S_1/S_0$   $\text{CoIn}$ s and is most easily followed by the rise of the ground state population. This begins after 25 fs, the first time a  $S_1/S_0$   $\text{CoIn}$  is reached. From here a fit (red line) to the on-the-fly data results in a total excited state lifetime of  $95 \pm 2$  fs (Fig. 5), which corresponds to the passage through the  $\text{CoIn}$ s. The 25 fs correspond to the experimentally observed 60 fs and the 95 fs to the observed 110 fs.

The discrepancy in the initial delay is attributed to the additional energy in the  $\pi_1\pi_1^*$  state at the FC point on CASSCF level. This may lead to a speed up in reaching the  $\text{CoIn}$ s to the  $S_0$ -state.

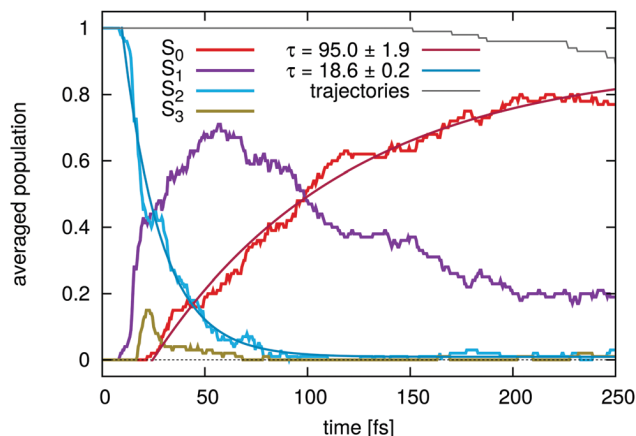


Fig. 5 Excited state population of the on-the-fly dynamics simulation of furan averaged over 100 trajectories. Lifetimes for the decay of the initially excited state ( $S_2$ , blue), as well as the total excited state lifetime (as negative of the rise of the ground state ( $S_0$ , red)) are shown. The fitting function used is  $\exp(-(x - x_0)/\tau) + y_0$ .  $x_0$  and  $y_0$  were included, because of the initial delay and the non-vanishing excited state population due to single trajectories which occasionally jump back from the ground state, or abort before the end of the propagation. The fraction of the 100 initial trajectories still running is indicated as grey line.

In addition, it may result in an overestimated fraction of the trajectories following the relaxation pathway *via* the ring opening, and could be the reason for the increased appearance of the opening pathway compared to the work of Fuji *et al.*<sup>6</sup>

## 4 The extended two-electron two-orbital model, introducing the aldehyde group

Furan is an interesting example of a molecule with competing relaxation pathways, where modification of one channel might influence which pathway is taken.<sup>§</sup> With this in mind, we use the extended two-electron two-orbital model,<sup>1,2</sup> to explain the formation of  $\text{CoIn}_p$ , the central point of the puckering pathway, and discuss, how its geometry will be altered by substitution of an aldehyde group. Predicting the implications on the geometry of a specific  $\text{CoIn}$  is the first step to being able to manipulate its energetic position.

The two-electron two-orbital model was first used by Bonačić-Koutecký *et al.*, to explain the formation of  $\text{CoIn}$ s in polyenes<sup>27,28</sup> and later extended by Nenov *et al.*<sup>1,2</sup> In this section, we provide a brief account of the model's fundamentals and utilization. The interested reader will find rigorous derivations of the formulas and in-depth discussion of the model in ref. 1, 2, 27 and 28. In the two-electron two-orbital model the description of the crossing states is reduced to two orbitals in which two electrons are placed in different occupation patterns. Reaching degeneracy of both states is split into two steps.

Table 2 Frequencies of the low lying normal modes of the  $\pi_1\pi_1^*$  state at the FC point which are connected to the opening and puckering pathway. The comparison between CASSCF and RS2C shows a major discrepancy in the asymmetric CO stretching vibration, indicating a steeper slope to the opened structure for RS2C. (Note that, due to symmetry, the gradients of the first three modes shown are zero, even in the excited state.) oop: out-of-plane motions of the O atom and the  $\alpha$ -H atom; CO asym: asymmetric stretching vibration of the CO-bonds; CO sym: symmetric stretching vibration of the CO-bonds

[ $\text{cm}^{-1}$ ]	oop (O)	oop (H)	CO asym	CO sym
CAS	-449	394	667	796
RS2C	-462	322	1989	789

<sup>§</sup> Even though the simulations likely misjudge the exact ratio between the pathways in furan, any alteration of one channel should lead to the same qualitative change in experiment and theory.



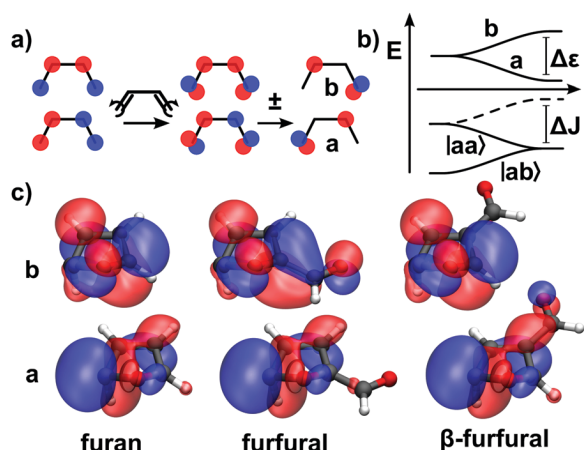


Fig. 6 (a) Schematic representation of the orbitals of butadiene, the polyene unit of furan. A disrotatory rotation of the CH<sub>2</sub> ends and subsequent linear combination of the degenerate HOMO and LUMO forms orbitals a and b. (b) Energy diagram of orbitals a and b, and the associated states |ab> and |aa> along a deformation coordinate. For the states to degenerate, a certain energy difference Δε between the orbitals a and b has to be introduced in order to cancel out ΔJ (difference between |ab> and the dashed line). (c) HOMO (bottom) and LUMO (top) of furan, furfural and β-furfural (from left to right).

The first step handles the requirements to reach orbital degeneracy, the second step addresses the requirements to reach energy degeneracy. Our discussion focuses on CoIn<sub>p</sub>, the S<sub>1</sub>/S<sub>0</sub> conical intersection of the puckering pathway.

First, we explain the formation of CoIn<sub>p</sub> in furan. For this purpose, the π-system of furan is treated as a modified *cis*-butadiene, its polyene building block, without the heteroatom. Here, the two states involved will be described by two occupation patterns of two electrons in orbitals a and b (Fig. 6a). The orbitals are localized at different atomic centers. The states are a single occupation of a and b, written |ab>, and a double occupation of a, written |aa>.

The first step is to reach a geometry where the highest occupied molecular orbital (HOMO) and the lowest unoccupied molecular orbital (LUMO) degenerate. In butadiene, this can be achieved by a disrotatory twist of the CH<sub>2</sub> ends. A linear combination between HOMO and LUMO at this point yields the orbitals a and b, which are localized at different atomic centers (Fig. 6a). They still have the same energy. The two crossing states are now described by the configurations |ab> and |aa>. At this point of orbital degeneracy, the resonance integral between a and b vanishes ( $h_{ab} = 0$ ). This is the first required condition to reach a CoIn within this model.<sup>2</sup> The energy difference between the states |ab> and |aa> at this point is:

$$E_{|aa\rangle} - E_{|ab\rangle} = \Delta J - \Delta \epsilon, \quad (2)$$

where  $\Delta J = J_{aa} - J_{ab}$  is the additional Coulomb repulsion from placing two electrons in orbital a,  $J_{aa}$ , compared to distributing them over a and b,  $J_{ab}$ , and  $\Delta \epsilon = \epsilon_b - \epsilon_a$  is the energy difference between both singly occupied orbitals in the presence of the remaining electrons of the molecule. Thus, at the point where a and b are degenerate, the states |ab> and |aa> are separated by ΔJ.

This manifests the second requirement to reach a CoIn, the heterosymmetry condition. Either the energy of a has to be lowered, and/or the energy b has to be raised, until Δε equals ΔJ (Fig. 6b). During this process the resonance condition  $h_{ab} = 0$  must still persist. Degeneracy can be achieved by deformation, e.g. one of the CH<sub>2</sub> groups is pyramidalized which leads to an sp<sup>3</sup> hybridization and lowers the energy of the orbital which is localized at the respective carbon atom.

In furan, the oxygen atom influences the electronic situation in the molecule significantly and additional terms have to be taken into account for the resonance condition.<sup>1</sup> Still one can assign the involved CAS orbitals (Fig. 6c left) to the orbitals a and b of the model (Fig. 6a). At the CoIn, the δ-H atom in Fig. 6c is bent below the ring plane which pyramidalizes the δ-C atom and thereby lowers the energy of orbital a sufficiently to reach energy degeneracy. Thus, in furan the heterosymmetry condition is fulfilled by deformation.

In addition to the deformation, electronic effects of heteroatoms influence the energy of the orbitals a and b. As both effects combine to achieve  $\Delta \epsilon = \Delta J$ , the deformation of the δ-H at the CoIn can be manipulated by introducing electronic effects. In (α)-furfural and β-furfural, the aldehyde group interacts exclusively with a or b, depending on whether the orbital is localized in α or β position: in furfural orbital b, in β-furfural orbital a is affected (compare Fig. 6c). In the affected orbital, the polyenic π system interacts with the unoccupied π\* orbital of the CO group, which lowers its energy. The unaffected orbital stays the same in shape and energy. Consequently, Δε will change, and for the CoIn to be reached, the structure of the molecule has to be adjusted in order to fulfill  $\Delta \epsilon = \Delta J$  again.

In furfural, where the energy of b is lowered by the aldehyde group, the hydrogen atom has to be bent more, compared to furan, to equivalently lower the energy of a. In β-furfural, the hydrogen atom has to be bent less, because a is already stabilized by the CO orbital. In β-furfural, CoIn<sub>p</sub> can also be reached, when, instead of the δ-H, the α-H atom is puckered. In this case, the role of the orbitals a and b is exchanged. Thus, instead of orbital a, orbital b is connected to the aldehyde-group, and, like in furfural, the puckering has to be increased.

One can try to infer the impact of those structural changes on the energetic position of the CoIn on the potential energy surface, but to judge the energetic behaviour of the whole molecule, instead of only single MOs, quantum chemical calculations are still needed for most cases. For furan and its derivatives the question was whether the relative energy rises in furfural and decreases in β-furfural, as the bending of the hydrogen atom means further deformation compared to the equilibrium geometry. The influences on the CoIn were analyzed as part of the investigation of the deactivation process of both molecules.

## 5 Quantum chemical results of furfural and β-furfural

Table 3 shows the energies and transition dipole moments for selected excited states of all three molecules, furan, furfural, and β-furfural at the FC point. The aldehyde group introduces

**Table 3** Excitation energies, oscillator strengths and classification of selected excited states of furan, furfural and  $\beta$ -furfural for different methods and basis sets. For furan, the involved orbitals of the  $\pi\pi^*$  excitations are given and the states are ordered by electronic character. For furfural and  $\beta$ -furfural only the type of excitation is noted. The states are ordered energetically. For reading convenience, some Rydberg excitations and one excitation from the  $n_{\text{O}}$  orbital with small oscillator strength are left out. The numbering of the states ( $S_n$ ) is with respect to the listed states only. (CASSCF is abbreviated as CAS, CASPT2 as PT2)

Furan	Exc. energies [eV] (osc. str.; character)				
RS2C(10,10) ANO	6.26 (0.00; $\pi\text{Ryd}_{3s}$ )		6.24 (0.15; $\pi_1\pi_1^*$ )		6.43 (0.01; $\pi_1\pi_2^*/\pi_2\pi_1^*$ )
CCSD ANO	6.21 (0.00; $\pi\text{Ryd}_{3s}$ )		6.45 (0.17; $\pi_1\pi_1^*$ )		6.76 (0.00; $\pi_1\pi_2^*/\pi_2\pi_1^*$ )
CCSD 6-31+G*	6.39 (0.00; $\pi\text{Ryd}_{3s}$ )		6.63 (0.17; $\pi_1\pi_1^*$ )		6.86 (0.00; $\pi_1\pi_2^*/\pi_2\pi_1^*$ )
CAS(10,11) aug			6.79 (0.17; $\pi_1\pi_1^*$ )		6.65 (0.00; $\pi_1\pi_2^*/\pi_2\pi_1^*$ )

Furfural	$S_1$	$S_2$	$S_3$	$S_4$	$S_5$
CCSD ANO	3.91 (0.00; $n_{\text{O}}\pi^*$ )	5.20 (0.36; $\pi\pi^*$ )	6.20 (0.03; $\pi\pi^*$ )	6.52 (0.00; $\pi\text{Ryd}_{3s}$ )	7.23 (0.13; $\pi\pi^*$ )
CCSD 6-31+G*	3.96 (0.00; $n_{\text{O}}\pi^*$ )	5.34 (0.36; $\pi\pi^*$ )	6.31 (0.04; $\pi\pi^*$ )	6.61 (0.00; $\pi\text{Ryd}_{3s}$ )	7.41 (0.10; $\pi\pi^*$ )
CAS(14,12) 6-31G*	3.84 (0.00; $n_{\text{O}}\pi^*$ )	5.94 (0.09; $\pi\pi^*$ )	6.85 (0.29; $\pi\pi^*$ )		7.51 (0.15; $\pi\pi^*$ )
PT2(14,12) 6-31+G*	3.87 ( $n_{\text{O}}\pi^*$ )	4.71 ( $\pi\pi^*$ )	6.39 ( $\pi\pi^*$ )		

$\beta$ -Furfural	$S_1$	$S_2$	$S_3$	$S_4$	$S_5$
CCSD ANO	4.06 (0.00; $n_{\text{O}}\pi^*$ )	5.70 (0.11; $\pi\pi^*$ )	6.45 (0.10; $\pi\pi^*$ )	6.68 (0.00; $\pi\text{Ryd}_{3s}$ )	6.78 (0.40; $\pi\pi^*$ )
CCSD 6-31+G*	4.08 (0.00; $n_{\text{O}}\pi^*$ )	5.83 (0.10; $\pi\pi^*$ )	6.55 (0.16; $\pi\pi^*$ )	6.79 (0.00; $\pi\text{Ryd}_{3s}$ )	6.92 (0.34; $\pi\pi^*$ )
CAS(14,12) 6-31G*	3.95 (0.00; $n_{\text{O}}\pi^*$ )	6.19 (0.01; $\pi\pi^*$ )	7.65 (0.26; $\pi\pi^*$ )		8.18 (0.12; $\pi\pi^*$ )
CAS(14,14) aug	4.00 (0.00; $n_{\text{O}}\pi^*$ )	6.13 (0.01; $\pi\pi^*$ )	6.97 (0.17; $\pi\pi^*$ )		7.78 (0.36; $\pi\pi^*$ )
PT2(14,12) 6-31+G*	3.99 ( $n_{\text{O}}\pi^*$ )	5.21 ( $\pi\pi^*$ )	6.36 ( $\pi\pi^*$ )		

significant changes. Compared to furan, the first excited state of the derivatives is always a  $n_{\text{O}}\pi^*$  excitation from the aldehyde oxygen. Due to the extension of the  $\pi$  system by the aldehyde group, the  $\pi\pi^*$  states are lowered in energy while the Rydberg orbitals are less affected. Thus the  $\text{Ryd}_{3s}$  state shifts from the  $S_1$  (in furan) to the  $S_4$  position and the  $\text{Ryd}_{3p}$  orbital mixes only with the higher lying  $\pi\pi^*$  states. The highest oscillator strength is found for the  $S_2$  state for furan and furfural, while in  $\beta$ -furfural the  $S_5$  state shows the strongest transition dipole moment.

In furan, the excitation energies change slightly, from RS2C and the ANO basis to CASSCF with the aug basis, but the states stay clearly identifiable. In furfural and  $\beta$ -furfural, the electronic characters of the  $\pi\pi^*$  states depend strongly on the level of theory. While the CCSD results are characterized by dominant  $\pi\pi^*$  transitions, the CASSCF results are a mixture of many transitions. In consequence, the CASSCF excited states show significantly different oscillator strengths and cannot be assigned to the CCSD-states, which is unambiguously possible in furan.¶

On CCSD level of theory, we could identify three low-lying  $\pi\pi^*$  states ( $S_2$ ,  $S_3$ ,  $S_5$ ) which are characterized by HOMO–LUMO, HOMO–1–LUMO and HOMO–LUMO+1 excitations. Between  $S_3$  and  $S_5$ , several Rydberg states and another excitation from the  $n_{\text{O}}$  orbital are located. All these states have no oscillator strengths and are not listed except for the  $S_4(\pi\text{Ryd}_{3s})$  state, which is already known from furan. In furfural, the LUMO and in  $\beta$ -furfural the LUMO+1 are most similar to the LUMO of furan (see Fig. 7). This explains the shift of the strong oscillator strength from  $S_2$  to  $S_5$  in  $\beta$ -furfural.

¶ To facilitate the comparison at all, a set of CCSD-calculations was started from the CAS-orbitals. This hardly affected the energies but greatly helped with the interpretation of the CI vectors.

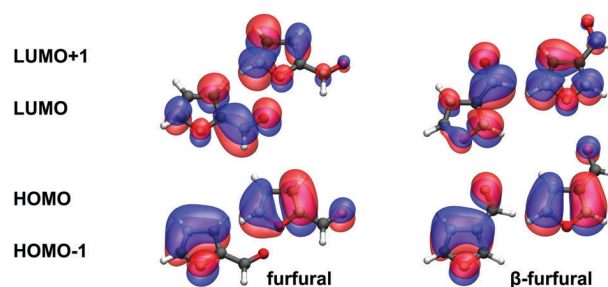


Fig. 7 Central  $\pi$  and  $\pi^*$  orbitals of furfural and  $\beta$ -furfural.

Regardless of which of the three basis sets is used, the  $\pi\pi^*$  states of the CASSCF calculations converge to solutions which are not described by one or two major determinants. The problem arises from the multitude of low-lying Rydberg states. In contrast to furan, adding diffuse 3p orbitals to the active space does not solve this issue. While no effect is observed in furfural, in  $\beta$ -furfural the description of the  $S_2$  and  $S_5$  states is only slightly improved such that  $S_5$  now has the strong oscillator strength. Nevertheless the electronic structure is still strongly mixed and remains unreliable. For this reason it is necessary to use multistate implementations when advancing to CASPT2. MOLCAS-CASPT2 (SA6) was employed to further investigate the character of the states. This results in two  $\pi\pi^*$  states with similar electronic character compared to the CCSD states for  $S_2(\pi\pi^*)$  and  $S_3(\pi\pi^*)$ .

The experimental data confirms the CCSD-results. Fig. 8 shows the experimental UV-spectra of furan (red), furfural (green) and  $\beta$ -furfural (blue) together with the theoretical data. The theoretical values are shifted by the difference between the calculated excitation energy of furan and the measured peak maximum. For CCSD (light green and blue) the shift is 0.39 eV (indicated by the red arrow) and for CASSCF (dark blue) 0.73 eV.

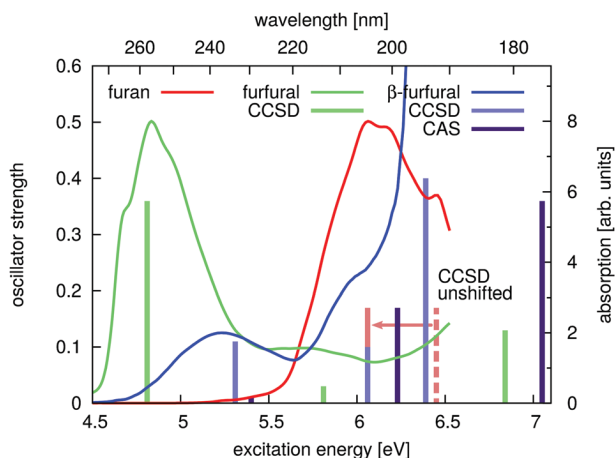


Fig. 8 Experimental UV absorption spectra of furan (red), furfural (green) and  $\beta$ -furfural (blue) and calculated excitation energies at the FC point (bars). The spectra are given in individual arbitrary units. The ANO CCSD- and aug (14,14) CASSCF-excitation energies are shifted by the energy difference of the experimental peak maximum of furan with the furan excitation energies of the respective methods. This is indicated by the dashed, red line, which symbolizes the unshifted CCSD excitation energy of furan (compare Table 3).

The CCSD excitation energies as well as the relative oscillator strengths coincide well with the experimental spectra. The CASSCF-results fit neither in their absolute nor relative peak position.

Leaving the FC region, the discrepancies in the description of the states between CCSD and CASSCF vanish. The influence of the Rydberg states decreases as their energy rises when outside the FC region. Therefore it is possible to apply the CASSCF method which allows to optimize the CoIns. CASSCF SA2 (12,11) was used to identify the  $S_1/S_0$  CoIns of the puckering and ring opening pathways. In this case the lonepair of the

aldehyde oxygen was left out, as the  $n_O\pi^*$  state lies energetically above the first  $\pi\pi^*$  state at this geometry. At another geometry, a third energetically low lying  $S_1/S_0$  CoIn between the  $n_O\pi^*$  and the  $S_0$  state can be located for both furan derivatives. It was optimized using the full (14,12) active space. To facilitate the comparison with the FC point, single point calculations on CCSD and MSPT2 level of theory were performed for all optimized CoIns. Table 4 shows the energy differences of the CoIns of all three molecules to the GS equilibrium energy and to the FC energy, as well as the pyramidalization realized in the puckered CoIns. The measurement of the degree of pyramidalization is explained in the ESI† (Fig. S2). A value of 0 corresponds to a planar and a value of 1 to a tetrahedral structure.

From furan to its derivatives the CoIns become less stabilized with respect to the FC point ( $\Delta_{FC-CoIn}$ ) for both, the puckering and the opening pathway, which will slow down the relaxation dynamics compared to furan. This is, as a general effect, largely attributed to the extension of the conjugated  $\pi$ -space in furfural and  $\beta$ -furfural compared to furan, which decreases the gap between the electronic states at the FC point. At the CoIns this effect is reduced, because the  $\pi$ -space partly segregates on the puckering pathway, and on the ring opening pathway the  $\sigma^*$  orbital of the  $\pi\sigma^*$  state is not part of the conjugation in the first place. Therefore,  $\Delta_{CoIn-Min}$  hardly changes from furan to its derivatives. For both derivatives the energies of the opened CoIns still lie roughly 1 eV below the puckered ones. The new  $S_1/S_0$  CoIns of the  $n_O\pi^*$  state (CoIn<sub>n</sub>) lie inbetween the others.

In comparison to the energetic consequences from the electronic changes at the FC point, the effect of the different degrees of pyramidalization in CoIn<sub>p</sub> is negligible. The exact position of only the H-atom turns out to be of minor importance. In case of  $\beta$ -furfural, where the  $\alpha$ - and  $\delta$ -CoIn<sub>p</sub> have the same FC point, the increased pyramidalization in the  $\alpha$ -position does not even lead to the assumed higher energy.

Table 4 Energetic position of the CoIns in furan, furfural and  $\beta$ -furfural, and the pyramidalization of the puckered CoIns. For furfural and  $\beta$ -furfural the values for the CoIn on both possible sides of the molecule are given and labeled  $\alpha$ , or  $\delta$ . The energy differences to the ground state energy in equilibrium geometry and to the FC-point ( $S_1$ ) with the exception of the PT2 energies of furan, were calculated with either MOLCAS-CASPT2 or CCSD using the 6-31+G\* basis set. For furan the results of RS2 (10,9) with the ANO basis set are given. To show the relatively small energy discrepancy between the methods at the CoIn structures, the  $\Delta_{CoIn-Min}$  on CASSCF level of theory were added (the basis sets are ANO for furan, 6-31G\* for CoIn<sub>p</sub> and CoIn<sub>o</sub> of the derivatives, and 6-31+G\* for CoIn<sub>n</sub>). The pyramidalization is given as  $(360 - \sum\gamma_i)/(360 - 3 \times \gamma_t)$ , where  $\gamma_i$  are the three angles around the considered atom, and  $\gamma_t$  is the angle of a tetrahedral surrounding (109.471°). The value runs from 0 (planar), over 1 (tetrahedral), to a theoretical maximum of 11.4 (all atoms coincide). See Fig. S2 in the ESI

			Furan	Furfural $\alpha$	Furfural $\delta$	$\beta$ -Furfural $\alpha$	$\beta$ -Furfural $\delta$
Puckering	$\Delta_{FC-CoIn_p}$ [eV]	PT2	1.30		-0.33	0.22	0.16
		CCSD	1.56		0.18	0.74	0.63
	$\Delta_{CoIn_p-Min}$ [eV]	PT2	4.95		5.05	4.99	5.05
		CCSD	5.07		5.16	5.09	5.20
		CAS	5.28		5.23	5.28	5.29
Pyramidalization		1.644		1.830	1.790	1.455	
Opening	$\Delta_{FC-CoIn_o}$ [eV]	PT2	2.26	0.82	0.64	1.19	1.40
		CCSD	2.39	1.19	0.99	1.45	1.74
	$\Delta_{CoIn_o-Min}$ [eV]	PT2	3.99	3.89	4.07	4.01	3.81
		CCSD	4.24	4.15	4.34	4.38	4.09
		CAS	3.82	3.63	3.67	3.63	3.70
$n_O\pi^*$ state	$\Delta_{FC-CoIn_n}$ [eV]	CCSD		0.88		0.95	
	$\Delta_{CoIn_n-Min}$ [eV]	CCSD		4.47		4.88	
		CAS		4.48		5.11	

The influence of the substituent and its location on the pyramidalization itself, however, is exactly as predicted by the extended two-electron two-orbital model. The degree of pyramidalization is highest in furfural, followed by  $\beta$ -furfural, puckered in the  $\alpha$ -position (the two CoIns with the stabilized orbital b), next is furan, and the last  $\beta$ -furfural, puckered in the  $\delta$ -position (the CoIn with the stabilized orbital a). This is an excellent confirmation for the validity of the model, and in a next step, one could think of altering the molecule to link its energy to the predicted structural change more strongly.

## 6 Dynamics of furfural and $\beta$ -furfural

Time resolved photoelectron spectroscopy was performed with two different pump-probe settings for the furan derivatives. Fig. 10 and 11 show the spectra of furfural upon pump-probe wavelengths of 267/400 nm and 200/267 nm, respectively. The spectra of  $\beta$ -furfural are similar and are provided in the ESI.† Overall the experimental time constants of furfural and  $\beta$ -furfural confirm the theoretical findings. In comparison to furan the dynamics are slowed down significantly, as expected from the reduced excitation energy due to the extended  $\pi$ -system.

The photoelectron spectra do not show the same strong time dependent shift of electron kinetic energy as in furan and thus no notable wavepacket dynamics in the excited state can be assigned. This is in agreement with the theoretically predicted decrease in the slope of the excited states. Instead the spectrum

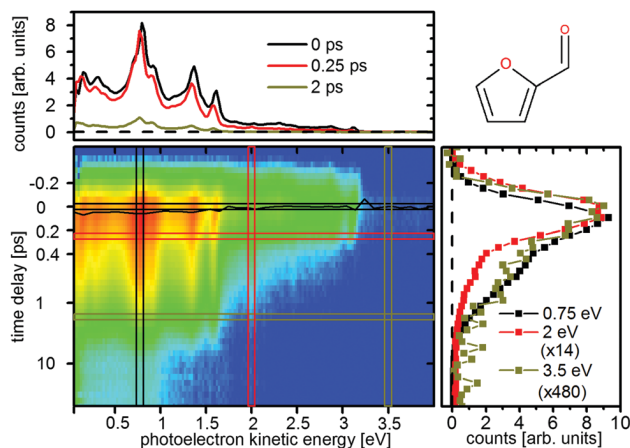


Fig. 10 Time-resolved photoelectron spectrum of furfural upon excitation at 267 nm and ionization at 400 nm. The black line represents the time zero shift  $t_0(E)$  as fitted by eqn (1). The scaling factors for the cuts on the right are 14 (2 eV, red) and 480 (3.5 eV, ocher).

is highly structured (Fig. 10 and 11, top) and the individual peaks remain throughout the measured time interval. For excitation with the 267 nm pulse two time constants can be attributed to the relaxation to the ground state. The time constants are  $\tau_1 = 140 \pm 30$  fs and  $\tau_2 = 1.58 \pm 0.2$  ps for furfural, and  $\tau_1 = 300 \pm 50$  fs and  $\tau_2 = 2.15 \pm 0.3$  ps for  $\beta$ -furfural, respectively. Both time constants are visible across the whole spectra. For excitation with the 200 nm pulse only

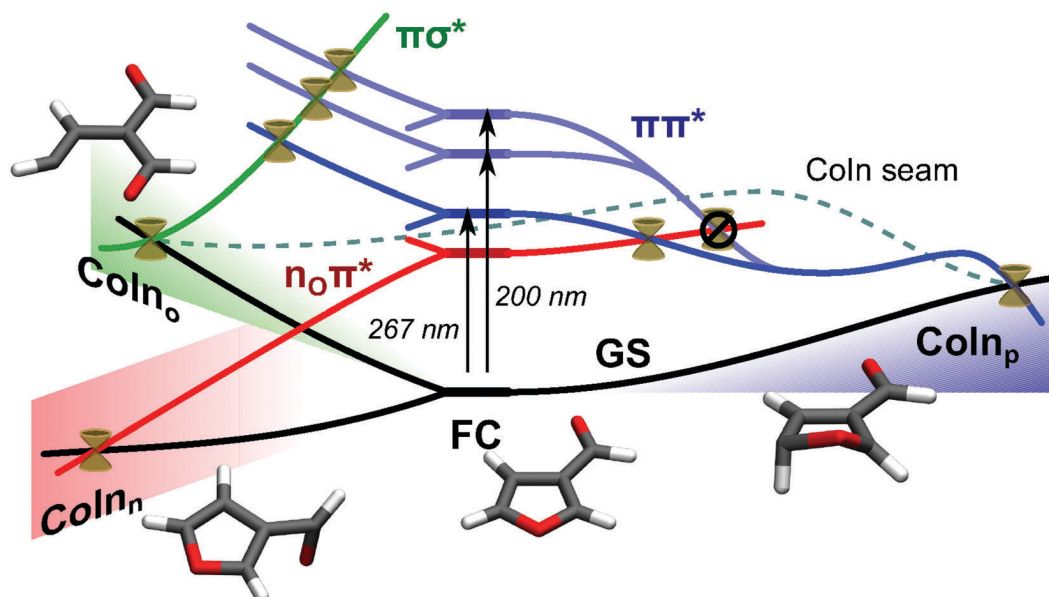


Fig. 9 Relaxation scheme for  $\beta$ -furfural. Initial excitation at the FC region populates the energetically lowest lying  $\pi\pi^*$  state (blue) with the 267 nm pump pulse, or two higher excited  $\pi\pi^*$  states (light blue) with the 200 nm pump pulse. Three possible deactivation routes arise: (1) (blue) – the puckering pathway is assumed to be the main pathway, in accordance with furan. It leads through a  $S_1$  minimum to  $Con_p$ . Here it relaxes to the ground state via a photophysical process. (2) (green) – If one of the CO bonds in the ring is elongated far enough, the  $\pi\sigma^*$  state (green) stabilizes and crosses all three  $\pi\pi^*$  states (see Fig. S3 in the ESI†). From  $Con_o$  the ring opens and thereby the photochemical process takes place.  $Con_o$  and  $Con_p$  are connected by a Con seam. (3) (red) – The  $n_o\pi^*$  state (red) crosses the  $\pi\pi^*$  states somewhere on the potential energy surface, here shown exemplarily in the puckering pathway. It gets populated only from the lowest  $\pi\pi^*$  state. If this happens,  $Con_n$  can be reached mainly by rotation of the aldehyde group. The puckering and the opening decay with  $\tau_2$ , relaxation via  $n_o\pi^*$  is responsible for  $\tau_1$ .

Paper

PCCP

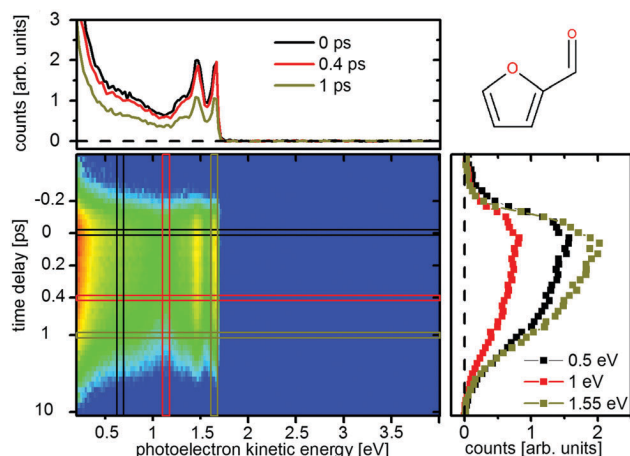


Fig. 11 Time-resolved photoelectron spectrum of furfural upon excitation at 200 nm and ionization at 267 nm.

one time constant can be observed,  $\tau_2 = 1.5 \pm 0.2$  ps for furfural and  $\tau_2 = 1.3 \pm 0.2$  ps for  $\beta$ -furfural. The maximum time-zero shift  $t_s$  for the 267 nm spectra is  $50 \pm 10$  fs for furfural and  $30 \pm 10$  fs for  $\beta$ -furfural. In the 200 nm spectra no shift is observed, which is likely caused by the wavepacket being temporarily trapped on the less steep, excited-state surface in the longer process connected to  $\tau_2$ .

The spectral structures show distinct peaks, but with different patterns for the two pump pulses. They can be explained by the corresponding He(I)-ionization spectra which exhibit a comparable structure.<sup>29</sup> This is exemplified in the ESI<sup>†</sup> (see Fig. S1) on furfural. The strong peak at 0.7 eV in the 267 nm spectrum using a two photon probe scheme has been attributed to an ionization from the  $n_O$  orbital of the aldehyde group.<sup>29</sup> This state is called  $n_O$  ionized state from here on. In the 200 nm spectrum the 0.7 eV peak is missing.

In addition the short lifetime  $\tau_1$  only appears for the excitation with the 267 nm pump. At this wavelength, the first excited  $\pi\pi^*$  state,  $S_2(\pi\pi^*)$ , is populated for both molecules, while the 200 nm pulse should populate both,  $S_2(\pi\pi^*)$  and  $S_3(\pi\pi^*)$  (see Fig. 8).

This means that an additional pathway opens when the reaction is started directly from the  $S_2(\pi\pi^*)$  state and is not reached from the higher lying  $S_3$  and  $S_5$  state. As both,  $\tau_1$  and  $\tau_2$ , can be observed over the whole spectrum, two separate relaxation pathways must exist. One of them corresponds to the one identified in furan, which is the pathway through the CoIn seam connecting  $CoIn_p$  and  $CoIn_o$ . Based on the reasoning from quantum chemistry given below, the other is assigned to  $CoIn_n$ , which is not included in this seam.  $CoIn_n$  mediates the relaxation involving the  $n_O\pi^*$  state (see Fig. 9).

After photoexcitation with either pump pulse the valence electrons of furfural and  $\beta$ -furfural are in a  $\pi n_O^2\pi^*$  configuration. This configuration remains when the systems follow the relaxation path towards the CoIn seam (Fig. 9, blue). Photoionization of the outer electron will dominantly lead to a  $\pi n_O^2$  configuration. When the other pathway towards  $CoIn_n$  is chosen (Fig. 9, red), the electronic character changes from  $\pi n_O^2\pi^*$  to  $\pi^2 n_O\pi^*$ . Photoionization of the outer electron will now result in a

$\pi^2 n_O$  configuration, which corresponds to the  $n_O$  ionized state. Consequently  $\tau_1$  is assigned to the relaxation *via* the  $n_O\pi^*$  state.

The participation of the  $n_O\pi^*$  state is also indicated by on-the-fly dynamics, where it gets partially populated. Keeping in mind the performance of CASSCF in the FC region, however, this can only be seen as a supportive indication. For the same reason, the corresponding  $S_2/S_1$  CoIns could not be optimized in a meaningful way.

## 7 Conclusions

The deactivation process of photoexcited furan and two of its derivatives, furfural and  $\beta$ -furfural were studied by time-resolved photoelectron spectroscopy and by quantum chemical calculation. The systems were selected to investigate the effect of substituents on the dynamics with furan taken as reference system. Using a high intensity probe pulse, the relaxation of furan from the FC region back to the ground state could be monitored through a two photon probe process. An excited state lifetime of  $60 \pm 15$  fs could be assigned to the time in which the molecule accesses the region of the CoIns to the ground state. A second time of  $110 \pm 25$  fs is assigned to the decay of the excited state which is mediated *via* the CoIn seam connecting the ring opening and ring puckering CoIns. The relaxation of furfural and  $\beta$ -furfural happens on a much slower timescale and, depending on the wavelength of the pump pulse, one or two lifetimes are found. Interestingly, for both molecules the pulse with the lower energy leads to the additional, shorter time constant. Quantum chemical calculations performed on CASSCF, CASPT2 and CCSD level of theory, assign the short life time to a deactivation *via* the  $n_O\pi^*$  state, which is related to the aldehyde group and thus not available in furan.

The general slowdown of the relaxation process from furan to its derivatives can also be explained by the aldehyde group introduced at different positions of the furan ring. It lowers the excitation energy in the FC region due to the extension of the  $\pi$  system, but it hardly effects the position of the CoIns with respect to the ground state minimum. Due to the structural deformation at the CoIns, the extension of the  $\pi$  system is removed. This is the dominant effect which defines the relative energies between ground state minimum, FC point and the CoIns. The two-electron two-orbital model successfully predicted the structural changes for  $CoIn_p$  of the puckering pathway when going from furan to its derivatives. The degree to which a hydrogen atom is bent beneath the ring has, however, only minor energetic effects. In molecules where the deformation has larger sterical consequences and the substituent position has less, even the energetic position of the CoIn on the potential energy surface should be predictable.

## Acknowledgements

We thank P. Limão-Vieira for sending us the data of their He(I) photoelectron spectrum of furfural used for Fig. S1 in the ESI<sup>†</sup>

[Jones *et al.*, *J. Chem. Phys.*, 2015, **143**, 184310] and acknowledge the generous support and technical advice of Prof. Dr Raimund Feifel. RDVR and SO acknowledge financial support by the Deutsche Forschungsgemeinschaft through the SFB749 and the excellence cluster Munich-Centre for Advanced Photonics (MAP) and thank Florian Rott and Daniel Keefer for carrying out first test calculations. OS would like to thank the Lars Hiertas Minne Foundation for a research grant. OS, TG, RT and TH acknowledge support from the Swedish Research Council and the Knut and Alice Wallenberg Foundation.

## References

- 1 A. Nenov and R. de Vivie-Riedle, *J. Chem. Phys.*, 2011, **135**, 034304.
- 2 A. Nenov and R. de Vivie-Riedle, *J. Chem. Phys.*, 2012, **137**, 074101.
- 3 A. Nenov, W. J. Schreier, F. Koller, M. Braun, R. de Vivie-Riedle, W. Zinth and I. Pugliesi, *J. Phys. Chem. A*, 2012, **116**, 10518–10528.
- 4 M. Stenrup and A. Larson, *Chem. Phys.*, 2011, **379**, 6.
- 5 N. Gavrilov, S. Salzmann and C. M. Marian, *Chem. Phys.*, 2008, **349**, 269–277.
- 6 T. Fuji, Y.-I. Suzuki, T. Horio, T. Suzuki, R. Mitrić, U. Werner and V. Bonačić-Koutecký, *J. Chem. Phys.*, 2010, **133**, 234303.
- 7 R. Spesyvtsev, T. Horio, Y.-I. Suzuki and T. Suzuki, *J. Chem. Phys.*, 2015, **143**, 014302.
- 8 E. V. Gromov, C. Léveque, F. Gatti, I. Burghardt and H. Köppel, *J. Chem. Phys.*, 2011, **135**, 164305.
- 9 E. V. Gromov, V. S. Reddy, F. Gatti and H. Köppel, *J. Chem. Phys.*, 2013, **139**, 234306.
- 10 T. J. A. Wolf, T. S. Kuhlman, O. Schalk, T. J. Martínez, K. B. Møller, A. Stolow and A.-N. Unterreiner, *Phys. Chem. Chem. Phys.*, 2014, **16**, 11770–11779.
- 11 O. Schalk, M. S. Schuurman, G. Wu, P. Lang, M. Mucke, R. Feifel and A. Stolow, *J. Phys. Chem. A*, 2014, **118**, 2279–2287.
- 12 O. Schalk, M. Stenrup, T. Geng, R. Lindh, R. D. Thomas, R. Feifel and T. Hansson, *J. Phys. Chem. A*, 2015, **119**, 11105.
- 13 O. Schalk, A. E. Boguslavskiy and A. Stolow, *J. Phys. Chem. A*, 2010, **114**, 4058–4064.
- 14 O. Schalk, T. Geng, T. Thompson, N. Baluyot, R. D. Thomas, E. Tapavicza and T. Hansson, *J. Phys. Chem. A*, 2016, **120**, 2320.
- 15 P. O. Widmark, P. A. Malmqvist and B. Roos, *Theor. Chim. Acta*, 1990, **77**, 291.
- 16 D. Feller, *J. Comput. Chem.*, 1996, **17**(13), 1571.
- 17 K. L. Schuchardt, B. T. Didier, T. Elsethagen, L. Sun, V. Gurumoorthi, J. Chase, J. Li and T. L. Windus, *J. Chem. Inf. Model.*, 2007, **47**(3), 1045.
- 18 F. Aquilante, J. Autschbach, R. K. Carlson, L. F. Chibotaru, M. G. Delcey, L. D. Vico, I. F. Galván, N. Ferré, L. M. Frutos, L. Gagliardi, M. Garavelli, A. Giussani, C. E. Hoyer, G. L. Manni, H. Lischka, D. Ma, P. A. Malmqvist, T. Müller, A. Nenov, M. Olivucci, T. B. Pedersen, D. Peng, F. Plasser, B. Pritchard, M. Reiher, I. Rivalta, I. Schapiro, J. Segarra-Martí, M. Stenrup, D. G. Truhlar, L. Ungur, A. Valentini, S. Vancoillie, V. Veryazov, V. P. Vysotskiy, O. Weingart, F. Zapata and R. Lindh, *J. Comput. Chem.*, 2016, **37**, 506–541.
- 19 H.-J. Werner, P. J. Knowles, G. Knizia, F. R. Manby, M. Schütz, P. Celani, T. Korona, R. Lindh, A. Mitrushenkov, G. Rauhut, K. R. Shamasundar, T. B. Adler, R. D. Amos, A. Bernhardsson, A. Berning, D. L. Cooper, M. J. O. Deegan, A. J. Dobbyn, F. Eckert, E. Goll, C. Hampel, A. Hesselmann, G. Hetzer, T. Hrenar, G. Jansen, C. Köppl, Y. Liu, A. W. Lloyd, R. A. Mata, A. J. May, S. J. McNicholas, W. Meyer, M. E. Mura, A. Nicklass, D. P. O'Neill, P. Palmieri, D. Peng, K. Pflüger, R. Pitzer, M. Reiher, T. Shiozaki, H. Stoll, A. J. Stone, R. Tarroni, T. Thorsteinsson and M. Wang, *MOLPRO, version 2012.1, a package of ab initio programs*, 2012, see <http://www.molpro.net/>.
- 20 H.-J. Werner, P. J. Knowles, G. Knizia, F. R. Manby and M. Schütz, *Wiley Interdiscip. Rev.: Comput. Mol. Sci.*, 2012, **2**, 242–253.
- 21 M. Barbatti, G. Granucci, M. Ruckebauer, F. Plasser, R. Crespo-Otero, J. Pittner, M. Persico and H. Lischka, *NEWTON-X: a package for Newtonian dynamics close to the crossing seam, version 1.4*, 2014, <http://www.newtonx.org/>.
- 22 M. Barbatti, M. Ruckebauer, F. Plasser, J. Pittner, G. Granucci, M. Persico and H. Lischka, *Wiley Interdiscip. Rev.: Comput. Mol. Sci.*, 2014, **4**, 26.
- 23 B. P. Fingerhut, S. Oesterling, K. Haiser, K. Heil, A. Glas, W. J. Schreier, W. Zinth, T. Carell and R. de Vivie-Riedle, *J. Chem. Phys.*, 2012, **136**, 204307.
- 24 S. Hammes-Schiffer and J. C. Tully, *J. Chem. Phys.*, 1994, **101**, 6.
- 25 D. Feller, *J. Comput. Chem.*, 1996, **17**(13), 1571–1586.
- 26 K. L. Schuchardt, B. T. Didier, T. Elsethagen, L. Sun, V. Gurumoorthi, J. Chase, J. Li and T. L. Windus, *J. Chem. Inf. Model.*, 2007, **47**(3), 1045–1052.
- 27 V. Bonačić-Koutecký, J. Köhler and J. Michl, *Chem. Phys. Lett.*, 1984, **104**, 440.
- 28 V. Bonačić-Koutecký, J. Koutecký and J. Michl, *Angew. Chem., Int. Ed.*, 1987, **26**, 170.
- 29 D. B. Jones, E. Ali, K. L. Nixon, P. Limão-Vieira, M.-J. Hubin-Franskin, J. Delwiche, C. G. Ning, J. Colgan, A. J. Murray, D. H. Madison and M. J. Brunger, *J. Chem. Phys.*, 2015, **143**, 184310.

## Chapter 3

# ASRS - passing the conical intersection

After traversing the excited state surface and reaching a CoIn, the wavepacket passes through it and thereby can relax back to the GS. While CoIns are naturally included in quantum chemical treatment and interpretation of photorelaxation processes, the direct experimental probing of them is rare. One major issue is the short amount of time, a wavepacket usually is located in their vicinity. Here the technical advances of the light sources enable a potential solution through attosecond laserpulses. In the present work, the theoretical simulation of ASRS signals is used to explore the capabilities of the method, and will serve as helpful tool to interpret the at times complex spectra.

In the following, the article “Monitoring conical intersections in the ring opening of furan by attosecond stimulated X-ray Raman spectroscopy”, *Struct. Dyn.* **3** (2016), 023601, is reprinted with the permission of AIP Publishing. The supplementary information is available at [aca.scitation.org/doi/suppl/10.1063/1.4933007](http://aca.scitation.org/doi/suppl/10.1063/1.4933007). Key points of the article are:

- The basic formalism and structure of ASRS, a novel spectroscopic detection scheme, are presented.
- A wavepacket passing through a conical intersection under three different mechanisms (adiabatic, diabatic, and branching) is simulated using a model system with a fixed number of state transitions and simple progressions of the state energies. The obtained signals show distinct characteristics, the branching signal, especially is suited to locate the CoIn. It forms, when only a fraction of the wavepacket changes its adiabatic state.
- The technique is utilized, to calculate spectra for a set of non-adiabatic semiclassical on-the-fly dynamics of furan, which decay to the GS via the ring opening pathway (see chapter 2.3). The signal of three distant points of one trajectory, as well as an adiabatic and a diabatic passage through the  $S_1/S_0$  CoIn of the ring opening pathway were analyzed in detail. The generated spectra prove to be very sensitive to the molecular geometry. The general patterns observed for the model system, however, can be found again in the spectra of the furan trajectories.
- Ensemble averaging was done for a set of trajectories which reached the ring opening CoIn within a certain time window. With some trajectories not hopping at the CoIn, the electronic character of the ensemble slowly changes, and a new feature forms in the spectrum.

## Monitoring conical intersections in the ring opening of furan by attosecond stimulated X-ray Raman spectroscopy

Weijie Hua,<sup>1,a)</sup> Sven Oesterling,<sup>2,a)</sup> Jason D. Biggs,<sup>1</sup> Yu Zhang,<sup>1</sup> Hideo Ando,<sup>1</sup> Regina de Vivie-Riedle,<sup>2,b)</sup> Benjamin P. Fingerhut,<sup>1,3</sup> and Shaul Mukamel<sup>1,c)</sup>

<sup>1</sup>Department of Chemistry, University of California, Irvine, California 92697, USA

<sup>2</sup>Department of Chemistry, University of Munich, Butenandtstr. 5-13, D-81377 Munich, Germany

<sup>3</sup>Max-Born-Institut für Nichtlineare Optik und Kurzzeitspektroskopie, Max Born Strasse 2A, 12489 Berlin-Adlershof, Germany

(Received 27 August 2015; accepted 31 August 2015; published online 9 October 2015; corrected 14 October 2015)

Attosecond X-ray pulses are short enough to capture snapshots of molecules undergoing nonadiabatic electron and nuclear dynamics at conical intersections (CoIns). We show that a stimulated Raman probe induced by a combination of an attosecond and a femtosecond pulse has a unique temporal and spectral resolution for probing the nonadiabatic dynamics and detecting the ultrafast ( $\sim 4.5$  fs) passage through a CoIn. This is demonstrated by a multiconfigurational self-consistent-field study of the dynamics and spectroscopy of the furan ring-opening reaction. Trajectories generated by surface hopping simulations were used to predict Attosecond Stimulated X-ray Raman Spectroscopy signals at reactant and product structures as well as representative snapshots along the conical intersection seam. The signals are highly sensitive to the changes in nonadiabatically coupled electronic structure and geometry. © 2015 Author(s). All article content, except where otherwise noted, is licensed under a Creative Commons Attribution 3.0 Unported License. [<http://dx.doi.org/10.1063/1.4933007>]

### I. INTRODUCTION

With the development of short femto- to picosecond light pulses,<sup>1</sup> it became possible to monitor molecular reactions in real time and determine ultrafast reaction rates.<sup>2</sup> Ultrafast photo-induced reactions are widely investigated in photochemistry and photobiology. Prominent examples are the photo damage and repair of the DNA bases,<sup>3–6</sup> the initial event in the process of vision,<sup>7,8</sup> electrocyclic photoreactions,<sup>9–12</sup> photodissociations,<sup>13,14</sup> and energy and charge transfer processes.<sup>15</sup> Ultrafast photodynamics is essential to current and emerging energy conversion and optical storage technologies. In many cases the observed dynamics can only be explained by the existence of conical intersections (CoIns)<sup>16</sup> a concept which has been established theoretically. CoIns are points where the molecule reaches a geometry for which potential energy surfaces of different electronic states come close in energy and may even become degenerate, and the Born-Oppenheimer (BO) approximation breaks down. The electronic and nuclear motions are strongly coupled and the molecule can rapidly relax nonradiatively to the lower lying electronic states, often all the way down to the ground state. A still existing caveat is that the rapid passage through a CoIn had so far prevented its direct spectroscopic observation. Only indirect evidence is available by recording the ultrafast changes in the spectroscopic signals of the reactants and the products in a pump-probe set up. CoIns lately became the focus of attention in the attosecond community.<sup>17</sup> Attosecond X-ray pulses have the capacity to probe

<sup>a)</sup>W. Hua and S. Oesterling contributed equally to the work.

<sup>b)</sup>Electronic mail: [regina.de\\_vivie@cup.uni-muenchen.de](mailto:regina.de_vivie@cup.uni-muenchen.de)

<sup>c)</sup>Electronic mail: [smukamel@uci.edu](mailto:smukamel@uci.edu)





the ultrafast electron and nuclear dynamics through CoIn. Attosecond pulses are now produced by high harmonic tabletop sources,<sup>18–21</sup> and much brighter femtosecond X-ray pulses are made possible by free electron lasers.<sup>22,23</sup>

In this paper, we show how this may be accomplished by a novel spectroscopic detection scheme, Attosecond Stimulated X-ray Raman Spectroscopy (ASRS), depicted in Fig. 1. The molecule interacts with 3 pulses. The first UV actinic pulse,  $k_1$ , initiates the ring-opening reaction. After a time delay  $T$ , the molecule evolves to a superposition of valence states described by the density matrix  $\rho_{ab}(T) = c_a c_b^*$ . It then interacts with two X-ray pulses  $k_2$  and  $k_3$ . The  $\sim 50$  femtosecond Raman pump  $k_2$  with frequency  $\omega_2$  is resonant with a core transition. The Raman probe  $k_3$  is broadband ( $\sim 100$  attosecond) with mean frequency  $\omega_3$  red-shifted from  $\omega_2$ . The Raman pump bandwidth is narrow compared with the lifetime broadening of the core transition and cannot induce an electronic Raman transition on its own. For example, a 30-fs pump has a FWHM bandwidth of 0.06 eV compared with the 0.13 eV lifetime broadening of the O1s core hole.<sup>24</sup> The signal is defined as the difference in the frequency dispersed transmission of the  $k_3$  pulse with and without the Raman pump. This technique is commonly used in vibrational Raman spectroscopy, where it is known as femtosecond stimulated Raman spectroscopy (FSRS).<sup>25–27</sup>

We assume an oriented sample, with both pump and probe having the same polarization vector,  $\epsilon$ . The transition dipole moments (TDMs) can then be replaced with their projection along this vector (that is,  $V_{ij} = V_{ij} \cdot \epsilon$ ). Assuming a monochromatic Raman pump  $\mathcal{E}_2(\omega) = \delta(\omega - \omega_2)$ , the ASRS signal is given by<sup>28</sup>

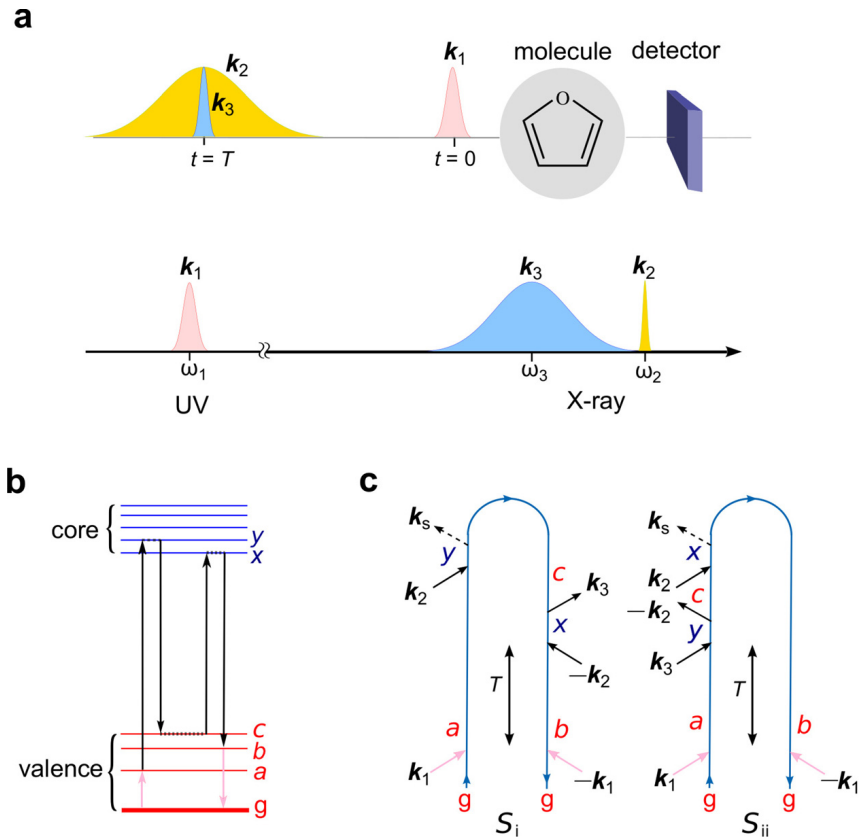


FIG. 1. Physical picture of the Attosecond Stimulated X-ray Raman Spectroscopy experiment. (a) Pulse sequence shown in the time (top) and frequency (bottom) domains. The UV actinic pump  $k_1$  initiates the reaction, and after time delay  $T$ , the time coincident narrow femtosecond pump  $k_2$  and broad attosecond probe X-ray pulses  $k_3$  interact with molecule to generate the ASRS signal. (b) Energy level diagram and transition process involved in ASRS detection. State variables are according to Eqs. (2)–(3):  $a, b, c$ , valence-excited states (including the ground state  $g$ );  $x, y$ , core-excited states. Energy order in each manifold is arbitrary. (c) The two loop diagrams that contribute to the signal [Eq. (1)]. Both diagrams show a wavefunction evolution pathway along  $b \leftarrow x \leftarrow c \leftarrow y \leftarrow a$ , but vary in the interaction with the Raman sequence in either the bra or the ket side of the loop (see ref 66 for diagram rules).

$$S(\omega - \omega_2, \omega_2, T) = S_i(\omega - \omega_2, \omega_2, T) + S_{ii}(\omega - \omega_2, \omega_2, T), \quad (1)$$

$$S_i(\omega - \omega_2, \omega_2, T) = -\text{Im} \sum_{abcxy} \frac{\rho_{ab}(T) V_{bx} V_{xc}^* V_{cy} V_{ya}^* \mathcal{E}_3(\omega) \mathcal{E}_3(\omega - \omega_{ab})}{(\omega_2 - \omega_{xb} - i\gamma_{xb})(\omega_2 - \omega_{ya} + i\gamma_{ya})(\omega - \omega_2 - \omega_{ac} + i\Gamma_{ac})}, \quad (2)$$

$$S_{ii}(\omega - \omega_2, \omega_2, T) = \text{Im} \sum_{abcxy} \frac{\rho_{ab}(T) V_{bx} V_{xc}^* V_{cy} V_{ya}^* \mathcal{E}_3(\omega) \mathcal{E}_3(\omega - \omega_{ab})}{(\omega - \omega_{xb} + i\Gamma_{xb})(\omega - \omega_{yb} + i\Gamma_{yb})(\omega - \omega_2 - \omega_{cb} + i\Gamma_{cb})}. \quad (3)$$

The two contributing terms  $S_i$  and  $S_{ii}$  can be, respectively, read off diagrams i and ii in Fig. 1(c).  $a$ ,  $b$ , and  $c$  denote valence excited states (including the ground state), whereas  $x$  and  $y$  represent core-excited states,  $\gamma_\alpha$  is the lifetime broadening of state  $\alpha$  with  $\Gamma_{\alpha\beta} = \gamma_\alpha + \gamma_\beta$ ,  $\gamma_{\alpha\beta} = \gamma_\alpha - \gamma_\beta$ , and  $\omega_{\alpha\beta} = \omega_\alpha - \omega_\beta$  stands for the energy difference.  $\mathcal{E}_3(\omega)$  is the Raman probe envelope. We also assumed that the electronic Hamiltonian does not change considerably during the fast interaction with the Raman probe (i.e., we neglect the dynamics during the interaction of the attosecond pulse). This is justified, since the X-ray Raman process occurs within the core lifetime ( $\sim 5$  fs),<sup>29</sup> whereby the nuclear motions are frozen. We watch the system valence dynamics by monitoring the signal variation with the time delay  $T$ .

We show that ASRS captures the geometrical and electronic structure changes when a CoIn is reached and passed, and can discriminate reactant, product, and CoIns with high sensitivity. This is confirmed by a complete active space self-consistent-field (CASSCF) spectroscopic study of the dynamics and relaxation pathways in the ring opening of photoexcited furan. Trajectories were generated by surface hopping nonadiabatic molecular dynamics (MD) simulations, and ASRS signals were calculated at selected snapshots.

## II. RESULTS AND DISCUSSION

### A. Passage through a conical intersection in a model system

The ultrafast passage through conical intersections is an example of a nonadiabatic transition—a fundamental problem in many chemical and biological systems.<sup>30</sup> The CoIn relaxation timescale and branching ratios are controlled by the topology of the branching space around the CoIn, the 2D subspace of nuclear degrees of freedom which lifts the degeneracy.<sup>16</sup> To set the stage for the ASRS signals of the nonadiabatic dynamics of a complex molecular system, i.e., the ring opening reaction of furan, we first illustrate the power of the technique with help of a simple model (see scheme in Fig. 2(e)) that captures the essentials of CoIn-mediated relaxation processes. 4 valence states,  $g$  (the ground state),  $e$ ,  $e_2$ , and  $e_3$ , are coupled to 2 core excited states,  $f$  and  $f_2$ . A conical intersection is created by  $g$  and  $e$ . Starting from a bright  $e$  state, the dynamics is incorporated phenomenologically, by varying the energy gap between  $e$  and  $g$  (from 1 eV to 0 eV and back to 1 eV) as well as TDMs between  $g$ ,  $e$  and core-excited states (all parameters provided in supplementary Note 1<sup>31</sup>).

The passage through a CoIn can in principle occur via three mechanisms. This is depicted in Figs. 2(a)–2(c) (left). Starting from a pure  $e$  state, states  $g$  and  $e$  switch state character (e.g., closed shell  $\leftrightarrow \pi\pi^*$ ) after the passage. The passage can occur (i) via a diabatic mechanism, where the wavepacket relaxes to the ground state and keeps the state character, (ii) via an adiabatic mechanism, where the wavepacket stays in the excited state with the character interchanged, or (iii) via a branching mechanism which gradually mixes the former two.<sup>32</sup> Using the same set of energies and TDMs, different passing mechanisms are modeled by different time evolution of the quantum amplitudes (supplementary Fig. 1).

Figures 2(a)–2(c) (right) depict the simulated ASRS signals. Signal at the initial time ( $T = -$ ) is the same for the three mechanisms. It is recaptured on top of Fig. 2(d) to demonstrate the ASRS peak features. Three major peaks contributed from diagram i (ii) are labeled by an A (1 and 2). For all these peaks, the same ASRS-active transition  $e \leftarrow f_2 \leftarrow e_3 \leftarrow f_2 \leftarrow e$  (see Fig. 2(e)) is assigned, in the order of  $b \leftarrow x \leftarrow c \leftarrow y \leftarrow a$ . Resonances are generated when one or several factors in the denominator of Eqs. (2) and (3) vanishes:  $\omega$  appears only

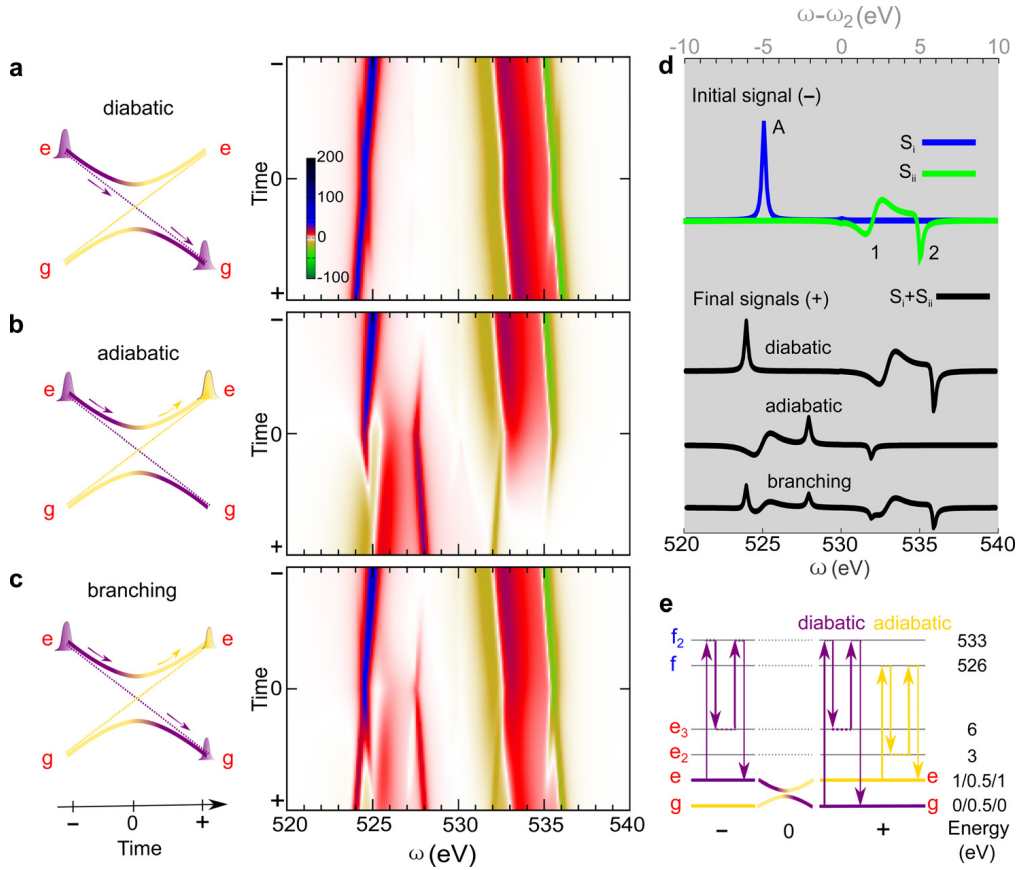


FIG. 2. Signals of a model system passing a conical intersection ( $T=0$ ) under 3 different mechanisms. (a)–(c) Left: Illustration of 3 mechanisms for passing a CoIn constituted by ground state  $g$  and valence excited state  $e$ , starting ( $T = -$ ) from a wavepacket with only  $e$  populated,  $|w_{-}\rangle = 1.0|e\rangle + 0|g\rangle$ . States with different characters are colored by purple and gold, and arrows show the wavepacket evolution. Solid lines, adiabatic representation; dashes, diabatic representation. Right: 2D-plot of the simulated ASRS signals for the model system (defined in panel e) at different time under each mechanism. (a) Diabatic passage. The system relaxes to state  $g$  while the state character persists (purple line). We assume the system changes via  $|w_0\rangle = \sqrt{0.5}|e\rangle + \sqrt{0.5}|g\rangle$  into  $|w_{+}\rangle = 0|e\rangle + 1.0|g\rangle$  in our model. (b) Adiabatic process. The system remains in state  $e$ , but the state character changes. We set  $|w_0\rangle = |w_{+}\rangle = |e\rangle = |w_{-}\rangle$ . (c) Branching mechanism with partial population transfer. We adopt  $|w_0\rangle = \sqrt{0.9}|e\rangle + \sqrt{0.1}|g\rangle$  and  $|w_{+}\rangle = \sqrt{0.5}|e\rangle + \sqrt{0.5}|g\rangle$ . (d) 1D slices of initial and final ASRS signals with respect to absolute (bottom axis) and relative (top axis) photon energies. Initial signal is decomposed as  $S_i$  and  $S_{ii}$ , and peaks are labeled. (e) Level scheme of the model of 4 valence and 2 core states.  $g$  and  $e$  have a switch in state character after the CoIn passage (purple and gold), and no change is assumed for other states (black). State energies are labeled. Only  $\omega_e$  and  $\omega_g$  vary during the process, to give an energy gap 1.0 eV at  $T = -/+$  and 0.0 eV at  $T=0$ . Additional parameters are given in supplementary Note 1. ASRS-active transitions at initial and final (diabatic and adiabatic passage) time are indicated by arrows.

once in  $S_i$  and resonances are attributed to  $c \leftarrow a$  valence transition ( $\omega - \omega_2 = \omega_{ac}$ );  $\omega$  appears three times in  $S_{ii}$ , indicating resonances to  $b \leftarrow c$  valence transition ( $\omega - \omega_2 = \omega_{cb}$ ), or  $b \leftarrow y$  or  $b \leftarrow x$  core deexcitation ( $\omega = \omega_{yb}$  or  $\omega = \omega_{xb}$ ). A single resonance from either diagram exhibits absorptive lineshape, and captures the valence transition information. The two absorptive peaks A and 2 correspond to the single valence resonance  $e \leftarrow e_3$  and  $e_3 \leftarrow e$ , respectively. Their transition energies  $-5.0$  eV and  $5.0$  eV can be read off the top axis (photon energy relative to  $\omega_2$ ).  $S_{ii}$  intensities can be greatly enhanced when two or three denominator factors approach zero at the same time (double- or triple-resonance), creating a dispersive-like lineshape. Among the multiple transitions, the double resonances for the same core transitions ( $\omega = \omega_{xb} = \omega_{yb}$ ) are the easiest to be satisfied. The dispersive peaks are an effective probe for core transitions. Peak 1 corresponds to double resonances of the  $e \leftarrow f_2$  core transition. The transition energy 532.0 eV (spreading 531.5–532.5 eV) can be read off the bottom axis (absolute photon energy). The dispersive peak magnitude depends on the core hole lifetime (supplementary Fig. 2).

Under the three mechanisms, signals evolve differently as different transitions are activated. For the diabatic passage (Fig. 2(a)), the involved state  $e$  is gradually transformed into  $g$ . At the final time ( $T = +$ ), the active transition is  $g \leftarrow f_2 \leftarrow e_3 \leftarrow f_2 \leftarrow g$  (Fig. 2(e)). In the diabatic model, the ASRS signal provides a direct probe of the populated state character irrespective of the energy order. The energy order switch leads to a red shift of peak A and a blue shift of peaks 1 and 2 by 1.0 eV ( $= \omega_{eg}$ ). Clear signal changes are observed during the adiabatic passage (Fig. 2(b)). This is because a different type of transition  $e \leftarrow f \leftarrow e_2 \leftarrow f \leftarrow e$  (Fig. 2(e)) is probed as time goes (while contribution of the initial transition channel decays) and uniquely remains till the end. Two absorptive peaks at  $\omega - \omega_2 = -2.0, 2.0$  eV from  $S_i$  and  $S_{ii}$  probe single valence resonance  $e \leftarrow e_2$  and  $e_2 \leftarrow e$ , respectively. A dispersive  $S_{ii}$  peak at  $\omega = 525.0$  eV (spreading 524.5–525.5 eV) probes the double core resonance  $e \leftarrow f$ . In the 2D signal of Fig. 2(b), these new peaks become gradually stronger, and the  $S_i$  and  $S_{ii}$  peaks manifest blue and red shifts. Figure 2(c) gives the signals of a prototypic population branching mechanism. Significant signal changes are observed during the passage, which arise from the adiabatic pathway. At the final time, the system is still in a superposition of states  $e$  and  $g$  (supplementary Fig. 1(c)), and the final signal combines features of the former two mechanistic limiting cases (Fig. 2(d)).

### B. Semiclassical molecular dynamics simulations of furan

Nonadiabatic MD simulations of the relaxation of photo-excited furan were performed using Tully’s fewest switch trajectory surface hopping (TSH) algorithm.<sup>33</sup> 100 250-fs trajectories were generated where 4 low-lying singlet valence states ( $S_0$ – $S_3$ ) were considered at the state-averaged CASSCF level. The simulations started with a bright  $\pi\pi^*$  state  $S_2$  prepared by the actinic pump and shortly underwent a population redistribution to  $S_1$  (supplementary Fig. 3). Then in an average time of 95 fs,  $S_1/S_0$  CoIn structures were reached with smooth variation from deformed to ring opening geometries. Most trajectories ended in the ground state  $S_0$ , in agreement with previous predictions.<sup>34</sup> Both pathways, the deformation,<sup>35</sup> as well as relaxations through a ring opening, were observed.

Snapshots were selected, aiming to study the signal change (1) among the reactant,  $S_1/S_0$  conical intersection, and product; and (2) during the diabatic/adiabatic passage of the CoIn. The conical intersections are not isolated points but form multidimensional seams. Signals for several CoIns within the seam are compared in supplementary Fig. 13. Nuclear coordinates and amplitudes of electronic states were used for the ASRS signal calculations. We had increased the number of states (from 4  $S_0$ – $S_3$  to 10  $V_0$ – $V_9$ ) and basis set (6-31G\* to aug-cc-pVDZ) to achieve more accurate and broad signals. The amplitudes of  $S_0$ – $S_3$  were projected into the new basis set, and the original  $S_1/S_0$  CoIn can be tracked as the  $V_1/V_0$  CoIn (supplementary Note 2).

### C. Signals at the reactant, conical intersection, and product configurations

To observe the structural changes around the C–O bond in the ring opening reaction, we focused on the core excitations at the O1s edge. This avoids the complexity caused by multiple core centers at the C1s edge.<sup>36</sup> 50 core excited states ( $C_1$ – $C_{50}$ ) were computed with the state-averaged restricted-active-space SCF (RASSCF) method.<sup>37</sup> The Raman pump frequency was set to 533.0 eV. A Gaussian spectral envelope  $\mathcal{E}_3(\omega) = e^{-\sigma^2(\omega-\omega_3)^2/2}$  was used for the broadband probe pulse, with  $\omega_3$  set to 528.0 eV and pulse duration  $\sigma = 100$  as. Most trajectories followed the ring opening pathway, where a possible product is a 3-membered ring. We picked one trajectory, traj. 3, which ran into a comparable geometry, and selected 3 snapshots at  $T = 0.0$  fs (**Reac-3**), 62.5 fs (**CoIn-3**), and 231.0 fs (**Prod-3**) as representative structures for the reactant, conical intersection, and product (see structures in Fig. 3(c)). The resulting ASRS signals displayed in Fig. 3(a) reveal strong variations in both shapes and magnitudes. This is to be expected due to the drastic changes in geometry and electronic structure. Absolute magnitude of the signals are sensitive to transition dipole moments due to the quadratic dependence [Eqs. (2) and (3)]. Here, **Reac-3** has absolute intensity  $10^3$  orders lower than the others simply

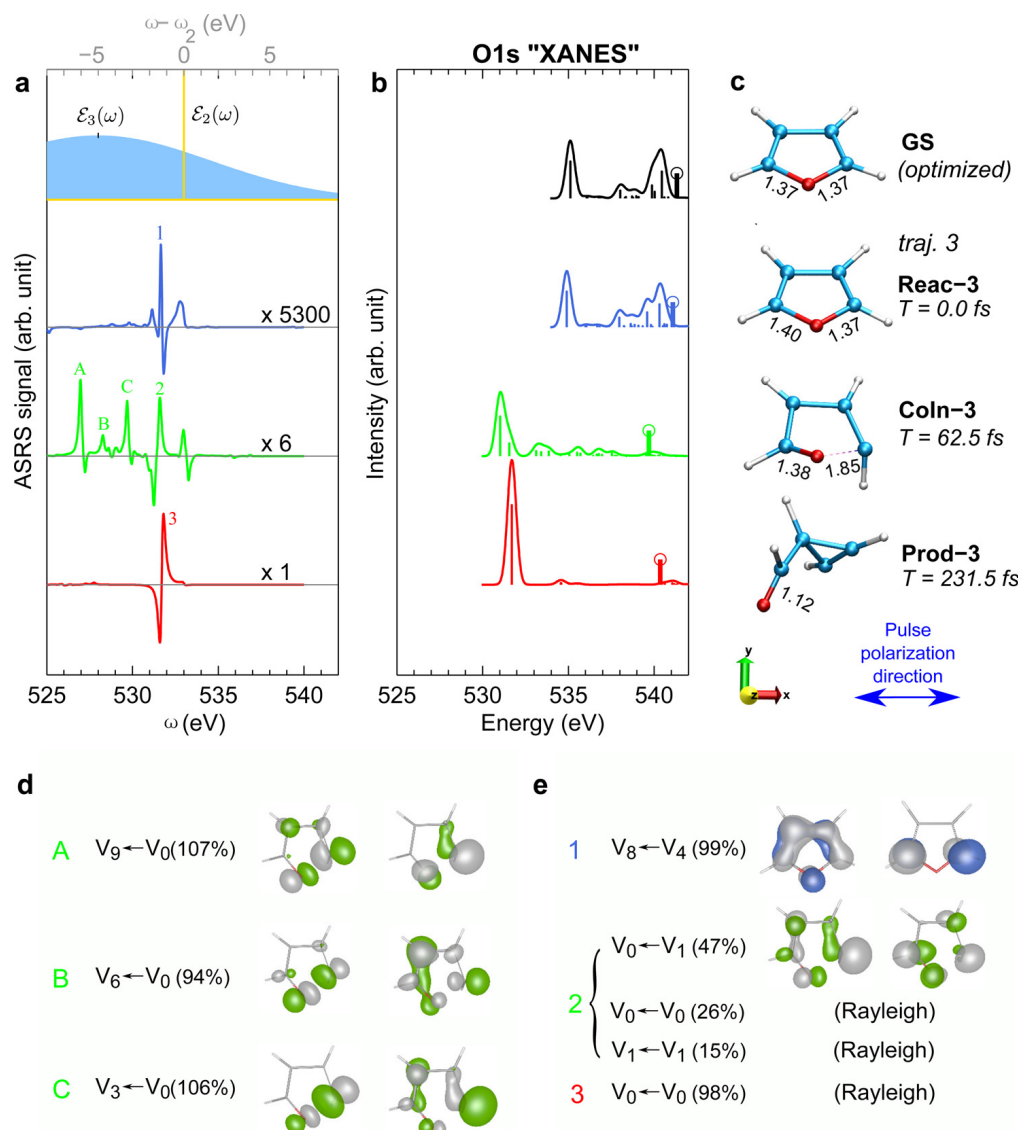


FIG. 3. Signals for reactant, conical intersection, and product geometries. (a) Simulated O1s ASRS signals of furan at 3 snapshots along trajectory 3: reactant **Reac-3**, conical intersection **CoIn-3**, and product **Prod-3**. Intense peaks contributed by diagrams i (ii) are labeled by A (1 and 2). Envelopes of pulses 2 and 3 ( $\mathcal{E}_2$  and  $\mathcal{E}_3$ ) are shown on the top. (b) Simulated artificial "O1s XANES spectra" at these snapshots and the optimized ground-state geometry. Stems label calculated O1s IPs. (c) Corresponding geometries, with C–O distances given in Å. (d) Assignment of major transitions. Percentages in parenthesis are contributions of the specified major transitions divided by  $S_i$  or  $S_{ii}$ . (e) Raman transitions are analyzed in terms of the natural transition orbitals (NTOs),<sup>38–40</sup> where dominant particle (left) and hole (right) orbital pairs are plotted with contour isovalue = 0.08.

because small X component of TDM between active valence and core states (it is a nearly planar structure put in the XY plane and we set the photon X-polarized).

The dominant peaks from diagram i (ii) are labeled by A, B, C (1, 2, 3). Separate plots of  $S_i$  and  $S_{ii}$  contributions are provided in supplementary Fig. 4; experimentally, we only observe their sum. Peaks assignments are given in Table I. Peak 1 of **Reac-3** is interpreted as  $V_8 \leftarrow C_{23} \leftarrow V_4 \leftarrow C_{23} \leftarrow V_8$ . Triple resonances lead to a strong dispersive peak. Valence transition frequency  $\omega(V_4) - \omega(V_8) = -1.4$  eV and core transition frequency  $\omega(C_{23}) - \omega(V_8) = 531.7$  eV can be directly read from the top and bottom axes, respectively. Peak 3 of **Prod-3** probes double resonances for the core transitions  $V_0 \leftarrow C_1$ . Mixing of different channels appears in **CoIn-3**. The impurity is caused by the two constituting states  $V_0$  and  $V_1$  (projected

TABLE I. ASRS peak assignments. Assignments of major transitions along the entire pathway of wavefunction evolution  $b \leftarrow x \leftarrow c \leftarrow y \leftarrow a$  (Fig. 1(c)) for ASRS peaks defined in Fig. 3(a). Peak positions are in eV.

Geometry	peak	position	$b \leftarrow x \leftarrow c \leftarrow y \leftarrow a$
<b>Reac-3</b>	1	531.7	$V_8 \leftarrow C_{23} \leftarrow V_4 \leftarrow C_{23} \leftarrow V_8$
<b>CoIn-3</b>	A	527.0	$V_{0,1} \leftarrow C_{3,4,2} \leftarrow V_9 \leftarrow C_{3,4,2} \leftarrow V_0$
	B	528.3	$V_{0,1} \leftarrow C_{3,4,2} \leftarrow V_6 \leftarrow C_{3,4,2} \leftarrow V_0$
	C	529.7	$V_{0,1} \leftarrow C_{3,4} \leftarrow V_3 \leftarrow C_{3,4} \leftarrow V_0$
	2	531.6	$V_{0,1} \leftarrow C_2 \leftarrow V_{1,0} \leftarrow C_2 \leftarrow V_{1,0}$
<b>Prod-3</b>	3	531.8	$V_0 \leftarrow C_1 \leftarrow V_0 \leftarrow C_1 \leftarrow V_0$

from  $S_0$  and  $S_1$ ; supplementary Note 2), which have close energy (ca. 0.1 eV) and similar state population. For instance, peak 2 (from  $S_{ii}$ ) is interpreted as  $V_{0,1} \leftarrow C_2 \leftarrow V_{1,0} \leftarrow C_2 \leftarrow V_{1,0}$ . To see the involved valence transitions between the two states, we decomposed the signal into each  $(b, c)$  pair as the  $S_{ii}$  channel probes the  $b \leftarrow c$  valence transition. This assigns a mixture of anti-Stokes transition  $V_0 \leftarrow V_1$  (47%) and Rayleigh transitions  $V_0 \leftarrow V_0$  (26%) and  $V_1 \leftarrow V_1$  (15%).

We had further analyzed the valence Raman transitions in terms of the natural transition orbitals (NTOs)<sup>38–40</sup> (Figs. 3(d) and 3(e)). The NTOs obtained from singular value decomposition of the spin-summed transition density matrix provide a visual illustration of each transition through one or several hole and particle orbitals (NTO pairs). For instance, the  $V_8 \leftarrow V_4$  to transition of **Reac-3** (peak 1) is mainly characterized by the creation of an electron in the delocalized, bonding  $\pi$  orbital and a hole in the localized, anti-bonding  $C-p_z$  orbitals. **CoIn-3** is a biradical. Peak A is characterized as  $V_9 \leftarrow V_0$  transition, through which the biradicals on the two terminals become more delocalized. By contrast, in peaks B and C, the electrons are transferred from a delocalized  $\pi$  orbital to be more localized on the two terminals. For peak 2, the NTOs picture the electron movement for the  $V_0 \leftarrow V_1$  transition.

Figure 3(b) gives the simulated O1s X-ray absorption near edge structure (XANES) spectra from the ground state at each geometry. Even though these are not experimental observables (since the molecule is in a superposition of valence states instead of ground state), they provide a window into the transition energies and dipole moments. In **CoIn-3** and **Prod-3**, the C–O bond is broken and the oxygen site becomes a radical. This leads to a 3–4 eV red shift for the main peak positions in the simulated XANES spectra, as compared to **GS** or **Reac-3**. A similar red shift was observed experimentally in the C1s XANES spectra of the  $\cdot\text{CH}_3$  radical.<sup>41</sup> Unlike XANES, there is no large global shift in the ASRS signals because the broadband pulse covers a wide region (ca. 10 eV, top of Fig. 3(a)) and can excite different valence-core transitions.

#### D. Signals in the vicinity of conical intersections

The ASRS signals clearly reveal the rapid passage through a CoIn. We use two MD trajectories 21 and 24 to illustrate the diabatic and adiabatic passage, respectively. Figure 4 displays the energy and amplitude variation of four states  $S_0$ – $S_3$  in the first 50 fs of the MD simulations. Initially, the molecule is excited to the bright  $S_2$  state, then it redistributes into  $S_1$  during 15.0–25.0 fs, reaching the  $S_1/S_0$  CoIn at 29.0 fs (traj. 21) or 28.5 fs (traj. 24). The difference is that the system then turns into  $S_0$  in traj. 21, while it remains in  $S_1$  in traj. 24. The two constituting states populations change steeply in the vicinity of a CoIn. We study the passage for 10 consecutive snapshots in a time window of 4.5 fs (26.5–31.0 fs). Each set provides a series with minor perturbations in chemical structure but show noticeable variations in electronic structure due to the breakdown of the BO approximation.

Figure 5(a) displays the simulated ASRS signals of traj. 21, where from left to right we show the total signal and separated contributions arising from populations ( $\rho_{00}$  and  $\rho_{11}$ ) and the coherence ( $\rho_{01} + \rho_{10}$ ) of the two constituting states,  $V_0$  and  $V_1$ . The system gradually evolves from  $V_1$  to  $V_0$  (see their amplitudes in Fig. 5(b)); other valence states have negligible

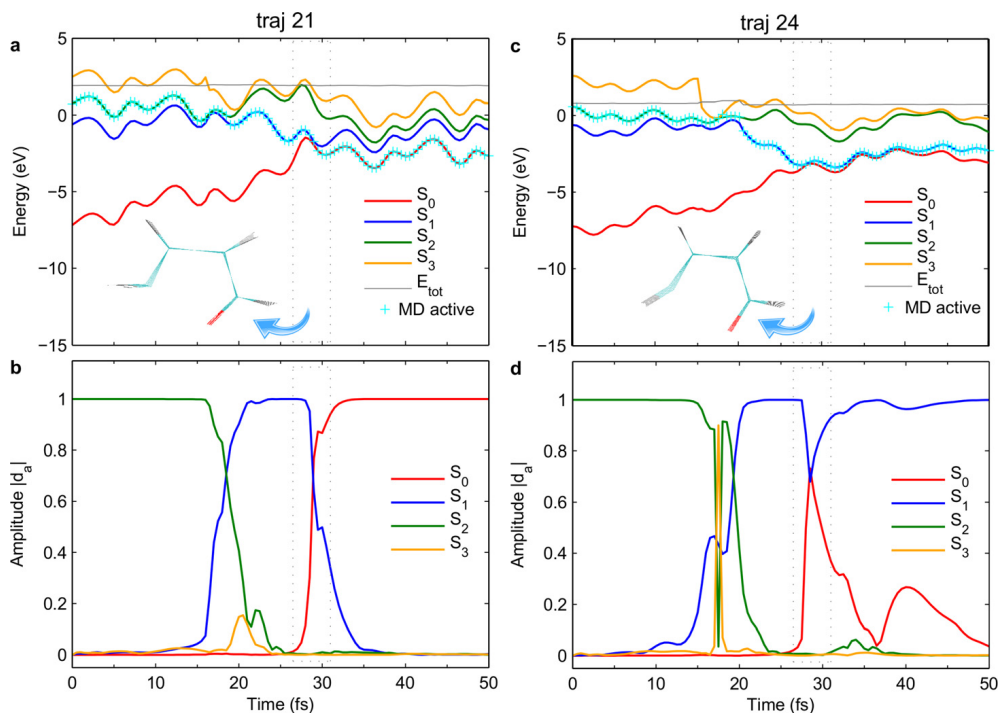


FIG. 4. Time-dependent energies and amplitudes. Time-dependent CASSCF energies (top) and amplitudes (bottom) of valence states  $S_0$ – $S_3$  in the first 50 fs of (a) and (b) MD traj. 21 and (c) and (d) traj. 24. The  $S_1/S_0$  CoIn of the two trajectories appears at ca. 29.0 fs and 28.5 fs and is characterized as mainly diabatic and adiabatic passage, respectively. A time window of 4.5 fs ( $T=26.5$ – $31.0$  fs, see dotted boxes) is chosen to study its CoIn passage (enlarged view provided in supplementary Fig. 5). Insets show the superposition of snapshots in the time window, with rmsd change in coordinates of 0.11 and 0.18 Å, respectively. In top panels, cyan crosses denote MD-active states and gray lines are total energies (sum of kinetic and potential energies).

amplitudes, see supplementary Note Fig. 2). The total signal is thus dominated by the  $\rho_{11}$  component first and then by  $\rho_{00}$ . In the middle region ( $T=28.5$ – $29.5$  fs), both states have comparable populations (thus induce coherence of comparable magnitude), so the total signal is composed by both population and coherence terms on similar footing. Time-dependent signals exhibit a “jump” around 29.0 fs (see also 2D contour plot in supplementary Fig. 6), which reflect the geometry and electronic structure changes in furan when the CoIn is approached. Such signal variation is caused by the change in valence-core transition dipole moments, and the sensitivity comes from the quadratic dependence which amplifies the difference. The evolution of  $V_0$ -core and  $V_1$ -core TDMs is interpreted in supplementary Fig. 7 by using the corresponding Gaussian convoluted oscillator strengths, where each exhibits a piecewise function switching at 29.0 fs. Apart from the short transition period (say, before 28.0 fs and after 29.5 fs), the electronic structure evolves much more slowly and accordingly the signals show relatively mild changes.

To understand the signal evolution, coherence contributions, and resonances that enhance the signals during the CoIn, we followed a major absorptive peak at ca. 527 eV (labeled by “o”), which comes from the  $S_i$  channel. The peak is interpreted as  $V_1 \leftarrow C_3 \leftarrow V_9 \leftarrow C_3 \leftarrow V_1$  in the beginning (till 28.0 fs), and  $V_0 \leftarrow C_3 \leftarrow V_9 \leftarrow C_3 \leftarrow V_0$  in the end (from 29.5 fs). While in the transition period (28.5–29.0 fs), both  $V_0$  and  $V_1$  are involved. The switch from  $V_1$  to  $V_0$  involved in the major transitions indicates that the ASRS signal picks up the state features regardless of their energy reversal. Underlying valence transitions ( $V_9 \leftarrow V_1$  or  $V_9 \leftarrow V_0$ ) are interpreted as mainly oxygen  $p$  orbital to  $\pi^*$  transitions by the NTOs (Fig. 5(c)). The NTOs verify the similar features of active transitions during the time. Meanwhile, they also visualize the progression for these transitions. As time increases, the hole (particle) orbitals change from delocalized to localized on the O atom (C-O terminals).

The calculated ASRS signals of traj. 24 is given in Fig. 6(a) to demonstrate the signal evolution during the adiabatic passage of the  $V_1/V_0$  CoIn. The CoIn is approached at ca. 28.5 fs.

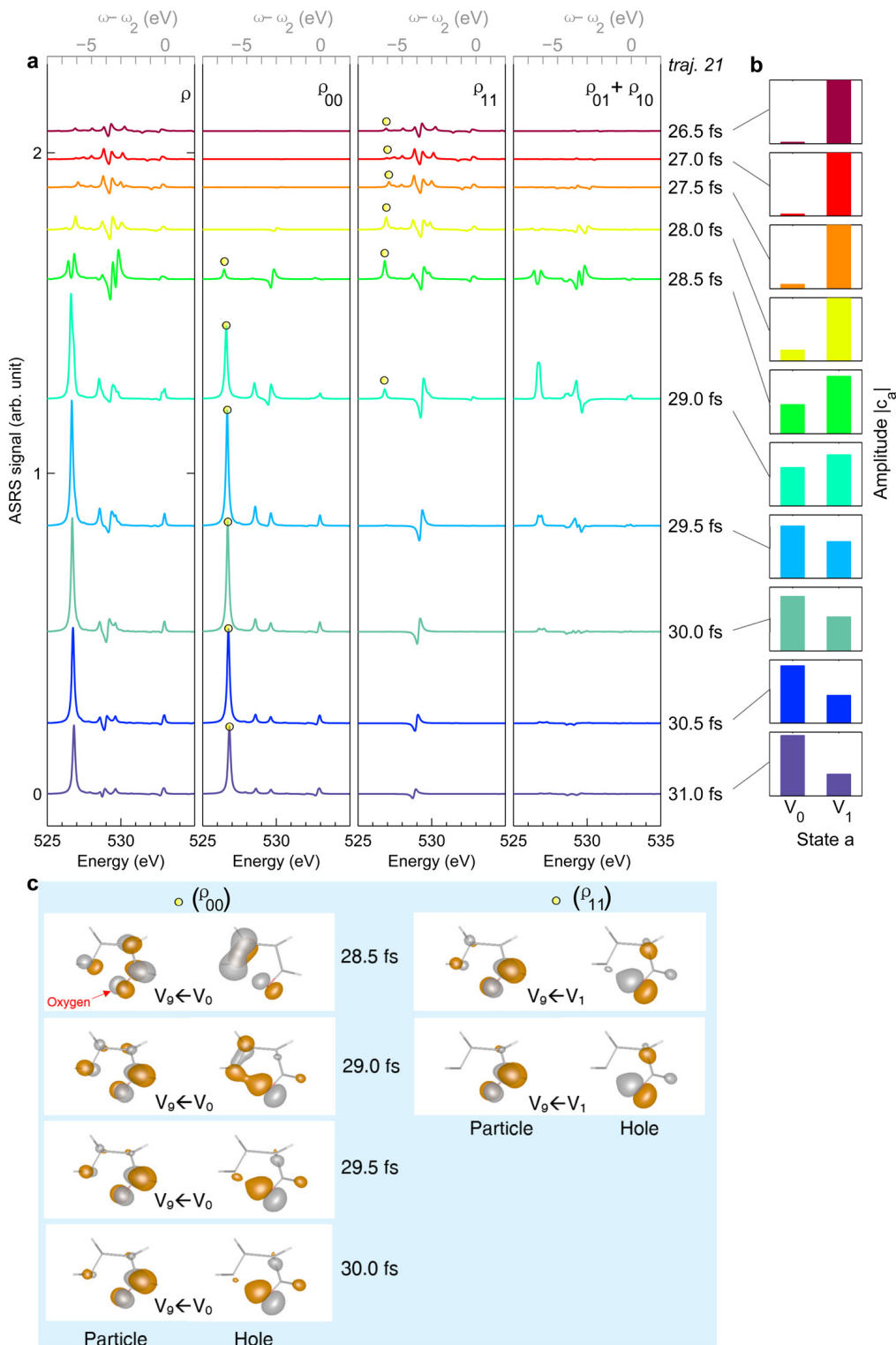


FIG. 5. Rapid variation of ASRS signals in diabatic passage of a conical intersection. (a) Simulated ASRS signals of furan during the diabatic passage of  $V_1/V_0$  conical intersection ( $T = 26.5 - 31.0$  fs in MD trajectory 21). From left to right, total signals and contributions from  $\rho_{00}$  and  $\rho_{11}$  populations, and  $\rho_{01} + \rho_{10}$  coherence (0 and 1 refer to states  $V_0$  and  $V_1$ ). (b) Absolute amplitudes of the two constituting states. (c) Major valence transitions (denoted by “o”) visualized by NTOs at selected time. Dominant hole and particle orbitals are plotted with contour isovalue = 0.08.

The wavepacket still remains in state  $V_1$  after passing the CoIn (in contrast to traj. 21; Fig. 6(b)), while the state character of  $V_1$  and  $V_0$  interchanges. As a result of the evident total signal change around the transition point (cf. signals at 27.5 – 29.0 fs in Fig. 6(a); see also 2D plot in



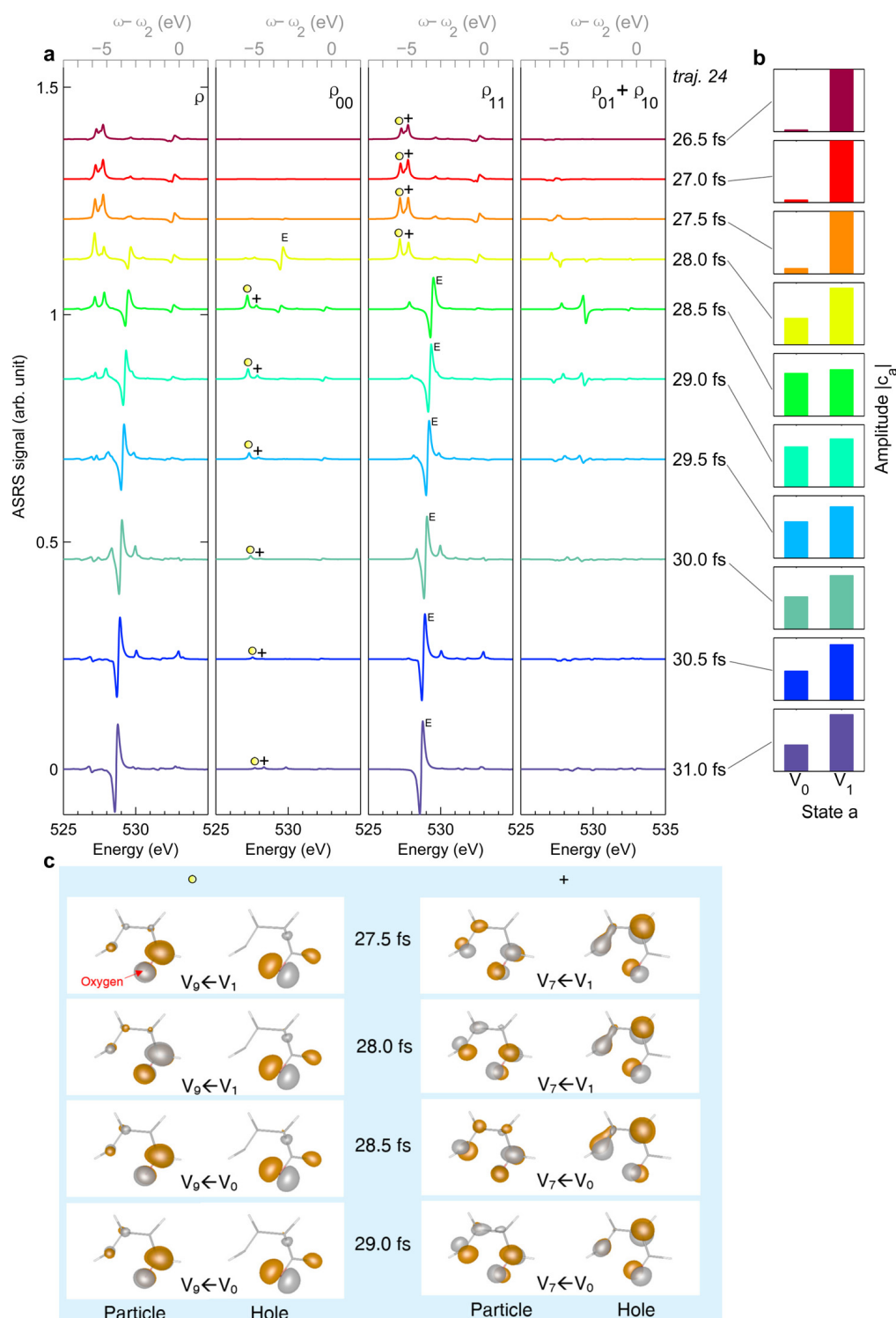


FIG. 6. Rapid variation of ASRS signals in adiabatic passage of a conical intersection. (a) Simulated ASRS signals of furan during the adiabatic passage of  $V_1/V_0$  conical intersection ( $T = 26.5 - 31.0$  fs in MD trajectory 24). From left to right, total signals and contributions from  $\rho_{00}$  and  $\rho_{11}$  populations, and  $\rho_{01} + \rho_{10}$  coherence (0 and 1 refer to states  $V_0$  and  $V_1$ ). (b) Absolute amplitudes of the two constituting states. (c) Major valence transitions for the two main peaks (denoted by “+” and “o”) visualized by NTOs at selected time. Dominant hole and particle orbitals are plotted with contour isovalue = 0.08.

supplementary Fig. 8), the absorptive double peaks at 527–528 eV (denoted by “o” and “+”) decay while the dispersive, elastic peak (denoted by “E”) at 528.5 eV grows. For instance, peak “o” comes from  $V_1 \leftarrow C_{2,3} \leftarrow V_9 \leftarrow C_{2,3} \leftarrow V_1$  in the beginning and  $V_0 \leftarrow C_{2,3} \leftarrow V_9 \leftarrow C_{2,3} \leftarrow V_0$  transitions in the end. Clear sequence and progression of the NTOs for valence

Raman transitions is depicted in Fig. 6(c). The peak E corresponds to elastic valence transition  $V_0 \leftarrow V_0$  transition at 28.0 fs and  $V_1 \leftarrow V_1$  since 28.5 fs, both via an intermediate core state  $C_1$ . The evolution of  $V_0$ -core and  $V_1$ -core TDMs is interpreted in supplementary Fig. 9.

### E. Ensemble averaging

Above discussion had shown that the ASRS signals are capable to probe the diabatic or adiabatic passage of a CoIn along an individual trajectory. Experiments however record the ensemble average of many trajectories which may average out some features. Ensemble averaging over the complete trajectory evolution would require repeating the whole computational procedure for hundreds (more likely thousands) of trajectories, which is computationally extremely expensive. We focus on the fast appearance ( $< 40$  fs) of the  $S_1/S_0$  CoIns of the ring opening pathway. Within the short period, the trajectories sample a limited phase space and approximately resemble a compact wavepacket. We performed 300 short 40 fs MD simulations (in addition to the 100 250 fs MD trajectories), and chose the sub-ensemble of trajectories approaching the CoIn between 26.5–31.0 fs (most trajectories did not approach the  $S_1/S_0$  CoIn within the period). ASRS signals are then evaluated within this narrow time window to obtain good statistics. Totally 15 trajectories (including trajs. 21 and 24) were selected out (see structures in supplementary Fig. 10), and the signal evolution of each trajectory was calculated. For most trajectories, the initial wavepacket at 26.5 fs has a dominant  $S_1$  population and mainly  $\pi\sigma^*$  character. They constitute a rich set for the evolution of amplitudes ( $S_0 \leftarrow S_1$ ) and character [ $\pi^2 \leftarrow (\pi)^1(\sigma^*)^1$ ] to different extent (i.e., including those mainly retain the character). They show how the signals overlap and how the branching of different pathways would be observed. It has been shown above that when the electronic structure change is mild, the signal progression is slowed down. It is therefore reasonable to assume that the omitted trajectories contribute a smooth background within this time window.

Figure 7 displays the simulated averaged signal. It exhibits two clear regions contributed mainly from  $S_i$  and  $S_{ii}$ , respectively, and include two absorptive (labeled by “o” and “\*”) and one dispersive major features (“E”). Features of individual features can still be recognized. One important reason is that absolute signal intensity of individual trajectory varies by orders of 1–100 (due to the sensitivity to the TDMs). For instance, traj. 21 contributes to the feature “o” starting at 29.0 fs, while traj. 24 makes invisible contribution (cf. intensity scales in supplementary Figs. 6 and 8). Statistics selects out those trajectories with strong intensities, with limited smearing effect by others. Additional feature “\*” in the  $S_i$  region comes from the  $V_8 \leftarrow V_1$

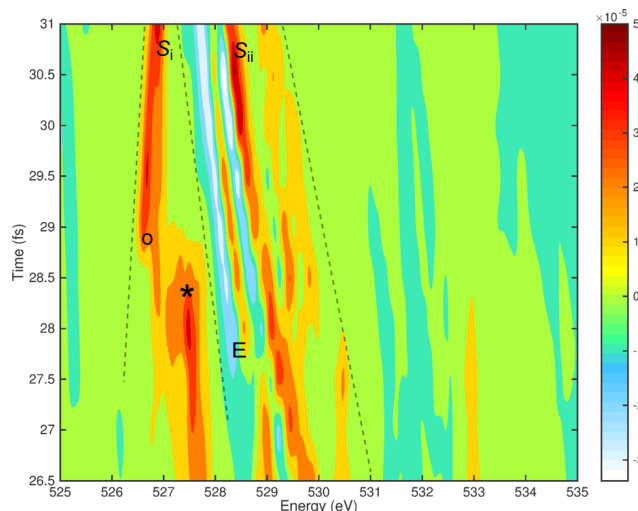


FIG. 7. Statistical average. Two-dimensional plot of the simulated ASRS signals averaged over 15 trajectories during the period 26.5–31.0 fs. The signals feature two evident regions (dashes are added to guide eyes), which mainly come from the  $S_i$  and  $S_{ii}$  channels, respectively. Three peak features are labeled as “o,” “\*” (absorptive peaks) and “E” (dispersive peak) at where they appear or disappear.

transition which starts to disappear at around 28.5 fs, indicating a CoIn at this region (see a constituting trajectory contribution in supplementary Fig. 11). Thus, the ASRS technique has its own capacity to record the main feature and turning point of different channels according to their signal intensities. Those with large absolute intensities are highly visible in the averaged signal. The  $S_{ii}$  region exhibits evident red shift. A dispersive feature “E” appears at around 27.5 fs and then gradually increases in intensity. It corresponds to mainly  $V_1 \leftarrow V_1$  (and slightly  $V_0 \leftarrow V_0$ ) elastic transition and appears in many trajectories (see a contributing trajectory in supplementary Fig. 12). Since this peak resonates with the state with  $\pi^2$  character, the increase in intensity qualitatively refers to the yield via the adiabatic passage. Thus, it indicates branching of different trajectories between the adiabatic and diabatic relaxation channels upon passage of the CoIn. The ASRS technique provides the required selectivity to record the distinct relaxation channels which arise from non Born-Oppenheimer branching events in the vicinity of CoIn.

### III. CONCLUSIONS

ASRS signals of photo-excited furan simulated at the CASSCF level reveal microscopic details of the ring-opening pathways. ASRS is highly sensitive to the electronic structure and serves as a probe for its variation during ultrafast reactions. The signals calculated for representative snapshots provide clear signatures which allow to discriminate reactant, product, and transient conical intersection structures as well as different CoIn structures in the seam (supplementary Fig. 13). Furthermore, the nonadiabatic transitions in the vicinity of conical intersections can be resolved by the proposed technique. Underlying physical processes of major ASRS peaks have been analyzed in detail. Absorptive and dispersive peaks have been interpreted: mathematically, they come from the single- and multiple- (double and triple) resonances, respectively, and chemically, they map out the valence and core resonance information, respectively.

In the ASRS technique, the attosecond pulse serves as a sharp time mark and ruler to accurately measure the time delay  $T$  to the actinic pump—by scanning  $T$ , the system dynamics can be monitored. Attosecond pulses have a broadband spectrum. For example, pulse duration of 100 attoseconds cover an energy range of 10–20 eV. This offers a broader window into electronic valence transitions. It is thus capable to follow the entire valence state evolution regardless of changing inter-valence transition moments or vanishing energy gap during the valence state relaxation dynamics. Attosecond pulses can be generated in the X-ray or XUV regime. When the carrier frequency falls in the X-ray regime, the spectroscopy is element-specific. By tuning the pulse frequency to excite the atom that is directly involved in the bond breaking, the chemical structure change during the reaction can be localized and followed.

In the vicinity of a conical intersection, electronic changes become increasingly rapid as the populations of the two constituting states are switched. The ASRS technique has the temporal resolution for monitoring these changes and detecting the appearance of a CoIn. Moreover, the combination of narrowband and broadband pulses in the Raman probe sequence facilitates unprecedented spectral resolution compared to X-ray absorption. When a CoIn is approached, additional coherence terms emerge from the off-diagonal elements of the density matrix and affect the ASRS signals. ASRS should provide a novel way for the powerful characterization of conical intersections, which are essential to the understanding of ultrafast photo-induced chemical reactions. Due to the high density of states of core excitations, it should deliver clear signatures of CoIn mediated dynamics, even for situations with vanishing energy gaps of valence electronic states which are often hampered by inter valence transition moments and the limited bandwidth of optical probe techniques.<sup>8</sup>

To date, the direct time-resolved experimental probing of conical intersections is rare. Most reported experiments have indirect circumstantial evidence of their presence, by probing the fast dynamics of a vibrational wave packet passing through a conical intersection<sup>8,42</sup> or via the product branching ratio.<sup>43</sup> Ultrafast femtosecond techniques can locate the CoIn with resolution of a few tens of femtoseconds.<sup>44</sup> Recent examples that are sensitive directly to the change in

electronic structure include high harmonic generation study of NO<sub>2</sub>,<sup>45</sup> X-ray ionization and fragmentation of hexane,<sup>46</sup> and the Auger probe of thymine.<sup>47</sup> ASRS signals offer a new possibility for capturing signatures of conical intersections. The technique provides a measure for coupled electron nuclear dynamics by mapping the instantaneous occupied valence state on core excitations. The incorporation of dephasing effects due to vibrational motions on different potential energy surfaces will be an important subject for future research. By combining femtosecond-attosecond pump-probe pulses for X-ray Raman detection, broadband signals are recorded in a single shot, making ASRS a promising tool for nonlinear X-ray spectroscopy.

## IV. METHODS

### A. MD simulation

Trajectories were simulated using the NewtonX 1.2 package<sup>48,49</sup> modified<sup>50</sup> to be compatible with Molpro.<sup>51</sup> The starting points for the individual trajectories were 100 structures taken out of a Wigner phase space distribution along the normal modes of the optimized ground state. Optimization and vibrational frequencies were calculated at the CCSD(T)/6-31G\* level. Nonadiabatic dynamics was simulated using the TSH algorithm.<sup>33</sup> No thermostat was used. Energies, gradients, and nonadiabatic couplings were computed every 0.5 fs at the CASSCF/6-31G\* level averaged over 4 states. The (10, 9) active space was employed which consists of the entire  $\pi$ -system of furan and both CO- $\sigma$  bonds and all corresponding antibonding orbitals (supplementary Fig. 14). The nonadiabatic coupling was evaluated only for states closer than 2 eV. Snapshots were then harvested for signal calculations.

### B. Transition dipole moments between valence and core states

The MD provided wavefunctions ( $|\Psi_n^{\text{MCSCF}}\rangle$ ) and amplitudes ( $d_n$ ) of 4 valence states ( $n = S_0-S_3$ ) at each geometry. However, the 6-31G\* basis set used in these trajectories is not suitable for core hole calculations since it does not adequately describe the short-range asymptotic behavior of the core hole states. We therefore switched to a larger aug-cc-pVDZ basis set.<sup>52</sup> Point test with the aug-cc-pVTZ basis set,<sup>52</sup> verified<sup>36</sup> for well description of the core excited furan, was also performed and similar results were obtained (supplementary Fig. 15). The TDMs between the core and valence states are easier to calculate with the same basis set. We recalculated the valence excited states using the aug-cc-pVDZ basis set, and projected the amplitudes  $d_n$  into the new basis set ( $c_m$ ) (supplementary Note 2). Additional states are needed in order to cover reasonably broad energy range for the ASRS spectroscopy. 10 valence states ( $V_0-V_9$ ) and 50 core-excited states ( $C_1-C_{50}$ ) were computed. This provided low-lying valence excited states up till  $\sim 10$  eV and core states up till the ionic potential (IP). The Molpro package<sup>51</sup> was used for valence and core calculations. The CASSCF method was used for valence calculations. For validation, we calculated the artificial ‘‘UV absorption’’ spectra at different active space sizes. Even though this is not a physical observable at geometries other than **GS**, it provides a good test for the accuracy of the calculated TDMs. Comparison of different active space sizes for selected geometries shows that the active space with 10 orbitals and 10 electrons led to converged spectra (supplementary Figs. 16(a)–16(b)). This active space was used for valence state calculations at all geometries.

MCSCF core state calculations were initiated in the 1980s by Ågren and co-workers.<sup>53–56</sup> In recent years, Odelius *et al.*<sup>57</sup> first employed the state-averaged RASSCF method<sup>37</sup> in conjunction with the state-interaction treatment of SO effects<sup>58</sup> for metal L-edge XANES and RIXS calculations. We started with the optimized 10-state-averaged valence wavefunction and employed RASSCF to calculate the core states. The O1s core orbital was frozen and set with a single occupation (RAS1). For geometries other than **GS** and **Reac-3**, we selected 10 orbitals in the RAS2 space, which allows full configuration interaction (CI). For **GS** and ground-state-like geometry **Reac-3** with mainly closed-shell feature, only 4 orbitals are set in the RAS2 space while 20 more orbitals are included in the RAS3 space with maximum occupation of 1 electron. This gives additional states in the high-energy region, as required for better agreement of the

calculated “O1s XANES spectroscopy” with experiment. Similarly, different active spaces had been tested for selected geometries to verify the accuracy of the calculated TDMs (supplementary Figs. 16(c)–16(d)). The O1s IP was calculated as the difference of the state-specific RASSCF total energies of the ionized and the neutral molecule. Core state energies of **GS** were shifted by  $-3.05$  eV by aligning the first resolved main peak of O1s XANES spectrum to experiment (535.1 eV).<sup>59</sup> The same shift value was then applied for all structures. Additionally, for the ground state geometry, the simulated UV and XANES spectra compare well with experiment<sup>59–62</sup> and theoretical TD-DFT results<sup>36</sup> (supplementary Fig. 17).

We then calculated the TDMs between all valence states  $m$  and core states  $p$ . The MCSCF wavefunctions are respectively given by  $|\Phi_m^{\text{MCSCF}}\rangle = \sum_j \lambda_j^m |\phi_j^m\rangle$  and  $|\Theta_p^{\text{MCSCF}}\rangle = \sum_i \kappa_i^p |\theta_i^p\rangle$ , where  $|\phi_j^m\rangle$  and  $|\theta_i^p\rangle$  are Slater’s determinants,  $\lambda_j^m$  and  $\kappa_i^p$  are the CI coefficients. The transition dipole matrix between  $|\Phi_m^{\text{MCSCF}}\rangle$  and  $|\Theta_p^{\text{MCSCF}}\rangle$  is given by

$$\langle \Phi_m^{\text{MCSCF}} | \hat{\mu} | \Theta_p^{\text{MCSCF}} \rangle = \sum_i \sum_j (\lambda_j^m)^* \kappa_i^p \langle \phi_j^m | \hat{\mu} | \theta_i^p \rangle. \quad (4)$$

$\langle \phi_j^m | \hat{\mu} | \theta_i^p \rangle$  were calculated using the Löwdin rules.<sup>63,64</sup>

### C. ASRS signal simulations

Using wavefunction and dipole integral matrices, the signals were calculated by our home built code. The two X-ray pulses were X polarized, while the molecule in the initial geometry stays in the XY plane. The narrowband frequency  $\omega_2$  was set to 533.0 eV to coincide with the first main peak in the O1s XANES spectra (an average value for all structures). The broadband pulse central frequency  $\omega_3$  is set to 5 eV lower, and pulse duration  $\sigma = 100$  as. 0.13 eV lifetime broadening was assumed for O1s core excited states.<sup>24</sup> For all valence excited states, a generic value of 0.05 eV was employed.<sup>36,65</sup> For the detection window,  $\omega$ ’s from 525 to 540 eV with 0.05 eV intervals were used. Point test was also carried out for **CoIn-3** to examine the effects of pulse (supplementary Fig. 18), where the narrowband frequency  $\omega_2$  was tuned from 529.0 eV to 535.0 eV with  $\omega_3$  fixed at 528.0 eV.

Our ASRS simulation protocol can be summarized as follows:

1. Nonadiabatic MD simulations at the CASSCF/6-31G\* level for 4 valence states ( $S_0$ – $S_3$ ) generate wavefunctions  $|\Psi_n^{\text{MCSCF}}\rangle$  and amplitudes  $d_n$ ; select representative snapshots for consequent steps.
2. CASSCF/aug-cc-pVDZ calculations for 10 valence states ( $V_0$ – $V_9$ ) to get  $|\Phi_m^{\text{MCSCF}}\rangle$ .
3. RASSCF/aug-cc-pVDZ calculations for 50 core-excited states ( $C_1$ – $C_{50}$ ) yield the wavefunctions  $|\Theta_e^{\text{MCSCF}}\rangle$ .
4. Project the amplitudes obtained from step 1 ( $d_n$ ) to the aug-cc-pVDZ level ( $c_m$ ) according to supplementary Eq. (5).
5. Calculate the TDMs between  $|\Phi_m^{\text{MCSCF}}\rangle$  and  $|\Theta_e^{\text{MCSCF}}\rangle$  using Eq. (4).
6. The amplitudes from step 4 and TDMs from step 5 are used to calculate the signals Eqs. (1)–(3).

### ACKNOWLEDGMENTS

The support of the National Science Foundation (Grant No. CHE1361516) and the Chemical Sciences, Geosciences and Biosciences Division, Office of Basic Energy Sciences, Office of Science, U.S. Department of Energy is gratefully acknowledged. This research used resources of the National Energy Research Scientific Computing Center, a DOE Office of Science User Facility supported by the Office of Science of the U.S. Department of Energy under Contract No. DE-AC02-05CH11231. B.P.F. gratefully acknowledges support through the German Research Foundation (DFG) within the Emmy Noether Program (Grant No. FI 2034/1-1).

- <sup>1</sup> *Ultrafast Phenomena VII*, edited by C. B. Harris, E. P. Ippen, G. A. Mourou, and A. H. Zewail (Springer-Verlag, Berlin-Heidelberg, 1990).
- <sup>2</sup> A. H. Zewail, "Femtochemistry: Atomic-scale dynamics of the chemical bond," *J. Phys. Chem. A* **104**, 5660–5694 (2000).
- <sup>3</sup> A. L. Sobolewski and W. Domcke, "Ab initio studies on the photophysics of the guanine-cytosine base pair," *Phys. Chem. Chem. Phys.* **6**, 2763–2771 (2004).
- <sup>4</sup> S. Perun, A. L. Sobolewski, and W. Domcke, "Ab initio studies on the radiationless decay mechanisms of the lowest excited singlet states of 9h-adenine," *J. Am. Chem. Soc.* **127**, 6257–6265 (2005).
- <sup>5</sup> C. Z. Bisgaard, O. J. Clarkin, G. Wu, A. M. D. Lee, O. Geßner, C. C. Hayden, and A. Stolow, "Time-resolved molecular frame dynamics of fixed-in-space CS<sub>2</sub> molecules," *Science* **323**, 1464–1468 (2009).
- <sup>6</sup> K. Haiser, B. P. Fingerhut, K. Heil, A. Glas, T. T. Herzog, B. M. Pilles, W. J. Schreier, W. Zinth, R. de Vivie-Riedle, and T. Carell, "Mechanism of UV-Induced Formation of Dewar Lesions in DNA," *Angew. Chem. Int. Ed.* **51**, 408–411 (2012).
- <sup>7</sup> L. M. Frutos, T. Andruniów, F. Santoro, N. Ferré, and M. Olivucci, "Tracking the excited-state time evolution of the visual pigment with multiconfigurational quantum chemistry," *Proc. Natl. Acad. Sci.* **104**, 7764–7769 (2007).
- <sup>8</sup> D. Polli, P. Altoè, O. Weingart, K. M. Spillane, C. Manzoni, D. Brida, G. Tomasello, G. Orlandi, P. Kukura, R. A. Mathies, M. Garavelli, and G. Cerullo, "Conical intersection dynamics of the primary photoisomerization event in vision," *Nature* **467**, 440–443 (2010).
- <sup>9</sup> G. Tomasello, M. J. Bearpark, M. A. Robb, G. Orlandi, and M. Garavelli, "Significance of a zwitterionic state for fulgide photochromism: Implications for the design of mimics," *Angew. Chem. Int. Ed.* **49**, 2913–2916 (2010).
- <sup>10</sup> A. Hofmann and R. de Vivie-Riedle, "Adiabatic approach for ultrafast quantum dynamics mediated by simultaneously active conical intersections," *Chem. Phys. Lett.* **346**, 299–304 (2001).
- <sup>11</sup> A. M. Müller, S. Lochbrunner, W. E. Schmid, and W. Fuß, "Low-Temperature Photochemistry of Previtamin D: A Hula-Twist Isomerization of a Triene," *Angew. Chem. Int. Ed.* **37**, 505–507 (1998).
- <sup>12</sup> B. C. Arruda and R. J. Sension, "Ultrafast polyene dynamics: The ring opening of 1,3-cyclohexadiene derivatives," *Phys. Chem. Chem. Phys.* **16**, 4439–4455 (2014).
- <sup>13</sup> B. P. Fingerhut, C. F. Sailer, J. Ammer, E. Riedle, and R. de Vivie-Riedle, "Buildup and decay of the optical absorption in the ultrafast photo-generation and reaction of benzhydryl cations in solution," *J. Phys. Chem. A* **116**, 11064–11074 (2012).
- <sup>14</sup> M. Lipson, A. A. Deniz, and K. S. Peters, "The sub-picosecond dynamics of diphenylmethylchloride ion pairs and radical pairs," *Chem. Phys. Lett.* **288**, 781–784 (1998).
- <sup>15</sup> L. Blancafort, F. Jolibois, M. Olivucci, and M. A. Robb, "Potential energy surface crossings and the mechanistic spectrum for intramolecular electron transfer in organic radical cations," *J. Am. Chem. Soc.* **123**, 722–732 (2001).
- <sup>16</sup> *Conical Intersections: Electronic Structure, Dynamics & Spectroscopy*, edited by W. Domcke, D. R. Yarkony, and H. Köppel (World Scientific, Singapore, 2004).
- <sup>17</sup> P. von den Hoff, R. Siemering, M. Kowalewski, and R. de Vivie-Riedle, "Electron dynamics and its control in molecules: From diatomics to larger molecular systems," *IEEE J. Sel. Top. Quantum Electron.* **18**, 119–129 (2012).
- <sup>18</sup> J. Krause, K. Schafer, and K. Kulander, "High-order harmonic generation from atoms and ions in the high intensity regime," *Phys. Rev. Lett.* **68**, 3535–3538 (1992).
- <sup>19</sup> P. Corkum, "Plasma perspective on strong field multiphoton ionization," *Phys. Rev. Lett.* **71**, 1994–1997 (1993).
- <sup>20</sup> H. Kapteyn, O. Cohen, I. Christov, and M. Murnane, "Harnessing attosecond science in the quest for coherent x-rays," *Science* **317**, 775–778 (2007).
- <sup>21</sup> K. T. Kim, D. M. Villeneuve, and P. B. Corkum, "Manipulating quantum paths for novel attosecond measurement methods," *Nat. Photonics* **8**, 187–194 (2014).
- <sup>22</sup> P. Emma, R. Akre, J. Arthur, R. Bionta, C. Bostedt, J. Bozek, A. Brachmann, P. Bucksbaum, R. Coffee, F.-J. Decker, Y. Ding, D. Dowell, S. Edstrom, A. Fisher, J. Frisch, S. Gilevich, J. Hastings, G. Hays, P. Hering, Z. Huang, R. Iverson, H. Loos, M. Messerschmidt, A. Miahnahri, S. Moeller, H.-D. Nuhn, G. Pile, D. Ratner, J. Rzepiela, D. Schultz, T. Smith, P. Stefan, H. Tompkins, J. Turner, J. Welch, W. White, J. Wu, G. Yocky, and J. Galayda, "First lasing and operation of an ångström-wavelength free-electron laser," *Nat. Photonics* **4**, 641–647 (2010).
- <sup>23</sup> J. Ullrich, A. Rudenko, and R. Moshhammer, "Free-electron lasers: New avenues in molecular physics and photochemistry," *Annu. Rev. Phys. Chem.* **63**, 635–660 (2012).
- <sup>24</sup> G. H. Zschornack, *Handbook of X-Ray Data*, 1st ed. (Springer, Berlin, 2007).
- <sup>25</sup> P. Kukura, D. W. McCamant, and R. A. Mathies, "Femtosecond stimulated Raman spectroscopy," *Annu. Rev. Phys. Chem.* **58**, 461–488 (2007).
- <sup>26</sup> K. E. Dorfman, B. P. Fingerhut, and S. Mukamel, "Time-resolved broadband raman spectroscopies: A unified six-wave-mixing representation," *J. Chem. Phys.* **139**, 124113 (2013).
- <sup>27</sup> K. E. Dorfman, B. P. Fingerhut, and S. Mukamel, "Broadband infrared and Raman probes of excited-state vibrational molecular dynamics: simulation protocols based on loop diagrams," *Phys. Chem. Chem. Phys.* **15**, 12348–12359 (2013).
- <sup>28</sup> Y. Zhang, J. D. Biggs, W. Hua, S. Mukamel, and K. E. Dorfman, "Three-dimensional attosecond resonant stimulated x-ray raman spectroscopy of electronic excitations in core-ionized glycine," *Phys. Chem. Chem. Phys.* **16**, 24323 (2014).
- <sup>29</sup> M. Tashiro, M. Ehara, H. Fukuzawa, K. Ueda, C. Buth, N. V. Kryzhevoi, and L. S. Cederbaum, "Molecular double core hole electron spectroscopy for chemical analysis," *J. Chem. Phys.* **132**, 184302 (2010).
- <sup>30</sup> H. Nakamura, *Nonadiabatic Transition: Concepts, Basic Theories and Applications* (World Scientific, 2012).
- <sup>31</sup> See supplementary material at <http://dx.doi.org/10.1063/1.4933007> for supplementary Figs. 1–18, Table 1, and Notes 1–2.
- <sup>32</sup> D. R. Yarkony, "Nonadiabatic quantum chemistry past, present, and future," *Chem. Rev.* **112**, 481–498 (2011).
- <sup>33</sup> J. C. Tully, "Molecular dynamics with electronic transitions," *J. Chem. Phys.* **93**, 1061–1071 (1990).
- <sup>34</sup> N. Gavrilov, S. Salzmann, and C. M. Marian, "Deactivation via ring opening: A quantum chemical study of the excited states of furan and comparison to thiophene," *Chem. Phys.* **349**, 269–277 (2008).
- <sup>35</sup> T. Fuji, Y.-I. Suzuki, T. Horio, T. Suzuki, R. Mitrić, U. Werner, and V. Bonačić-Koutecký, "Ultrafast photodynamics of furan," *J. Chem. Phys.* **133**, 234303–234303–9 (2010).

- <sup>36</sup>W. Hua, J. D. Biggs, Y. Zhang, D. Healion, H. Ren, and S. Mukamel, "Multiple core and vibronic coupling effects in attosecond stimulated x-ray raman spectroscopy," *J. Chem. Theory Comput.* **9**, 5479–5489 (2013).
- <sup>37</sup>P. Å. Malmqvist, A. Rendell, and B. O. Roos, "The restricted active space self-consistent-field method, implemented with a split graph unitary group approach," *J. Phys. Chem.* **94**, 5477–5482 (1990).
- <sup>38</sup>R. Martin, "Natural transition orbitals," *J. Chem. Phys.* **118**, 4775 (2003).
- <sup>39</sup>I. Mayer, "Identifying a pair of interacting chromophores by using SVD transformed CIS wave functions," *Chem. Phys. Lett.* **443**, 420–425 (2007).
- <sup>40</sup>P. Å. Malmqvist and V. Velyazov, "The binatural orbitals of electronic transitions," *Mol. Phys.* **110**, 2455–2464 (2012).
- <sup>41</sup>M. Alagia, M. Lavollée, R. Richter, U. Ekström, V. Carravetta, D. Stranges, B. Brunetti, and S. Stranges, "Probing the potential energy surface by high-resolution x-ray absorption spectroscopy: The umbrella motion of the core-excited CH<sub>3</sub> free radical," *Phys. Rev. A* **76**, 022509 (2007).
- <sup>42</sup>T. A. A. Oliver, N. H. C. Lewis, and G. R. Fleming, "Correlating the motion of electrons and nuclei with two-dimensional electronic vibrational spectroscopy," *Proc. Natl. Acad. Sci. U.S.A.* **111**, 10061–10066 (2014).
- <sup>43</sup>J. S. Lim and S. K. Kim, "Experimental probing of conical intersection dynamics in the photodissociation of thioanisole," *Nat. Chem.* **2**, 627–632 (2010).
- <sup>44</sup>T. Horio, T. Fuji, Y.-I. Suzuki, and T. Suzuki, "Probing ultrafast internal conversion through conical intersection via time-energy map of photoelectron angular anisotropy," *J. Am. Chem. Soc.* **131**, 10392–10393 (2009).
- <sup>45</sup>H. J. Wörner, J. B. Bertrand, B. Fabre, J. Higuët, H. Ruf, A. Dubrouil, S. Patchkovskii, M. Spanner, Y. Mairesse, V. Blanchet, E. Mvel, E. Constant, P. B. Corkum, and D. M. Villeneuve, "Conical intersection dynamics in NO<sub>2</sub> probed by homodyne high-harmonic spectroscopy," *Science* **334**, 208–212 (2011).
- <sup>46</sup>V. S. Petrović, M. Siano, J. L. White, N. Berrah, C. Bostedt, J. D. Bozek, D. Broege, M. Chalfin, R. N. Coffee, J. Cryan, L. Fang, J. P. Farrell, L. J. Frasinski, J. M. Glowina, M. Gühr, M. Hoener, D. M. P. Holland, J. Kim, J. P. Marangos, T. Martinez, B. K. McFarland, R. S. Minns, S. Miyabe, S. Schorb, R. J. Sension, L. S. Spector, R. Squibb, H. Tao, J. G. Underwood, and P. H. Bucksbaum, "Transient x-ray fragmentation: Probing a prototypical photoinduced ring opening," *Phys. Rev. Lett.* **108**, 253006 (2012).
- <sup>47</sup>B. K. McFarland, J. P. Farrell, S. Miyabe, F. Tarantelli, A. Aguilar, N. Berrah, C. Bostedt, J. D. Bozek, P. H. Bucksbaum, J. C. Castagna, R. N. Coffee, J. P. Cryan, L. Fang, R. Feifel, K. J. Gaffney, J. M. Glowina, T. J. Martinez, M. Mücke, B. Murphy, A. Natan, T. Osipov, V. S. Petrović, S. Schorb, T. Schultz, L. S. Spector, M. Swiggers, I. Tenney, S. Wang, J. L. White, W. White, and M. Gühr, "Ultrafast x-ray Auger probing of photoexcited molecular dynamics," *Nat. Commun.* **5**, 4235 (2014).
- <sup>48</sup>M. Barbatti, G. Granucci, M. Ruckebauer, F. Plasser, J. Pittner, M. Persico, and H. Lischka, "NEWTON-X: A package for Newtonian dynamics close to the crossing seam," version 1.2, [www.newtonx.org](http://www.newtonx.org) (2011).
- <sup>49</sup>M. Barbatti, G. Granucci, M. Persico, M. Ruckebauer, M. Vazdar, M. Eckert-Maksić, and H. Lischka, "The on-the-fly surface-hopping program system newton-x: Application to *ab initio* simulation of the nonadiabatic photodynamics of benchmark systems," *J. Photochem. Photobiol. A* **190**, 228–240 (2007).
- <sup>50</sup>B. P. Fingerhut, S. Oesterling, K. Haiser, K. Heil, A. Glas, W. J. Schreier, W. Zinth, T. Carell, and R. de Vivie-Riedle, "Oniom approach for non-adiabatic on-the-fly molecular dynamics demonstrated for the backbone controlled Dewar valence isomerization," *J. Chem. Phys.* **136**, 204307 (2012).
- <sup>51</sup>H.-J. Werner, P. J. Knowles, G. Knizia, F. R. Manby, M. Schütz, P. Celani, T. Korona, R. Lindh, A. Mitrushenkov, G. Rauhut, K. R. Shamasundar, T. B. Adler, R. D. Amos, A. Bernhardsson, A. Berning, D. L. Cooper, M. J. O. Deegan, A. J. Dobbyn, F. Eckert, E. Goll, C. Hampel, A. Hesselmann, G. Hetzer, T. Hrenar, G. Jansen, C. Köppl, Y. Liu, A. W. Lloyd, R. A. Mata, A. J. May, S. J. McNicholas, W. Meyer, M. E. Mura, A. Nicklass, D. P. O'Neill, P. Palmieri, D. Peng, K. Pflüger, R. Pitzer, M. Reiher, T. Shiozaki, H. Stoll, A. J. Stone, R. Tarroni, T. Thorsteinsson, and M. Wang, MOLPRO, version 2012.1, a package of *ab initio* programs (2012).
- <sup>52</sup>T. H. Dunning, "Gaussian basis sets for use in correlated molecular calculations. I. The atoms boron through neon and hydrogen," *J. Chem. Phys.* **90**, 1007–1023 (1989).
- <sup>53</sup>H. J. A. Jensen, P. Jørgensen, and H. Ågren, "Efficient optimization of large scale MCSCF wave functions with a restricted step algorithm," *J. Chem. Phys.* **87**, 451–466 (1987).
- <sup>54</sup>H. Ågren and H. J. Å. Jensen, "An efficient method for the calculation of generalized overlap amplitudes for core photoelectron shake-up spectra," *Chem. Phys. Lett.* **137**, 431–436 (1987).
- <sup>55</sup>H. Ågren, A. Flores-Riveros, and H. J. Å. Jensen, "An efficient method for calculating molecular radiative intensities in the VUV and soft x-ray wavelength regions," *Phys. Scr.* **40**, 745 (1989).
- <sup>56</sup>H. Ågren and H. J. Å. Jensen, "Relaxation and correlation contributions to molecular double core ionization energies," *Chem. Phys.* **172**, 45–57 (1993).
- <sup>57</sup>I. Josefsson, K. Kunnus, S. Schreck, A. Föhlisch, F. de Groot, P. Wernet, and M. Odelius, "*Ab initio* calculations of x-ray spectra: Atomic multiplet and molecular orbital effects in a multiconfigurational SCF approach to the l-edge spectra of transition metal complexes," *J. Phys. Chem. Lett.* **3**, 3565–3570 (2012).
- <sup>58</sup>P. A. Malmqvist, B. O. Roos, and B. Schimmelpfennig, "The restricted active space (RAS) state interaction approach with spin-orbit coupling," *Chem. Phys. Lett.* **357**, 230–240 (2002).
- <sup>59</sup>D. Duflot, J.-P. Flament, A. Giuliani, J. Heinesch, and M.-J. Hubin-Franskin, "Core shell excitation of furan at the O1s and C1s edges: An experimental and *ab initio* study," *J. Chem. Phys.* **119**, 8946–8955 (2003).
- <sup>60</sup>M. H. Palmer, I. C. Walker, C. C. Ballard, and M. F. Guest, "The electronic states of furan studied by VUV absorption, near-threshold electron energy-loss spectroscopy and *ab initio* multi-reference configuration interaction calculations," *Chem. Phys.* **192**, 111–125 (1995).
- <sup>61</sup>D. C. Newbury, I. Ishii, and A. P. Hitchcock, "Inner shell electron-energy loss spectroscopy of some heterocyclic molecules," *Can. J. Chem.* **64**, 1145–1155 (1986).
- <sup>62</sup>Z. D. Pešić, D. Rolles, I. Dumitriu, and N. Berrah, "Fragmentation dynamics of gas-phase furan following K-shell ionization," *Phys. Rev. A* **82**, 013401 (2010).
- <sup>63</sup>P.-O. Löwdin, "Quantum theory of many-particle systems. I. Physical interpretations by means of density matrices, natural spin-orbitals, and convergence problems in the method of configurational interaction," *Phys. Rev.* **97**, 1474–1489 (1955).

<sup>64</sup>D. B. Cook, *Handbook of Computational Quantum Chemistry* (Dover Publications, Mineola, NY, 2005), pp. 66–69.

<sup>65</sup>D. Healion, H. Wang, and S. Mukamel, “Simulation and visualization of attosecond stimulated x-ray Raman spectroscopy signals in *trans*-N-methylacetamide at the nitrogen and oxygen K-edges,” *J. Chem. Phys.* **134**, 124101 (2011).

<sup>66</sup>J. D. Biggs, J. A. Voll, and S. Mukamel, “Coherent nonlinear optical studies of elementary processes in biological complexes: diagrammatic techniques based on the wave function versus the density matrix,” *Philos. Trans. R. Soc. A* **370**, 3709–3727 (2012).



## Chapter 4

# Summary and outlook

Photorelaxation plays a role in diverse fields. It is constituting properties of synthetic products, and taking part in shaping nature. Ultrafast photorelaxation of a single molecule through CoIns involves typically large deformations and to theoretically describe the process, large areas of the PES have to be considered. Naturally, simulation of the whole dynamics of those mechanisms is desirable. The present work features as one major topic the interfacing between NewtonX and Molpro and describes the implementation of the quantum chemical methods ONIOM and CASPT2 into non-adiabatic semiclassical on-the-fly dynamics, which are well suited for this purpose. Furthermore, quantum chemical studies are presented, which focus on the influence of substituents on different regions of the pathways, and lastly the passage through a CoIn is investigated. All aspects are presented for different molecules, which entail their own specific results.

In the first chapter, using the ONIOM approach within the dynamics simulations on a whole dinucleotide, it is shown that the formation of the Dewar photolesion of DNA is backbone-controlled. Non-adiabatic dynamics on CASPT2 level of theory were successfully implemented and by this, the photorelaxation of ethylene was simulated, including the 3s-Rydberg state. Both examples show, how non-adiabatic semiclassical dynamics can be augmented, to increase both, the size of molecules considered, as well as the accuracy which is available for the description. Moving forward, implementing the Firefly program package [57] would allow to use a fast CASPT2 routine, which, in contrast to the fast CASPT2 versions of Molpro and Molcas, has an extended MS option, to assure a constant level of accuracy even in the vicinity of CoIns. As in the other program packages, too, analytic gradients are not available for this method. Here, the interface to Molcas, presented in appendix A, could be used as template.

In the second chapter, the Z to E isomerization speed of the hemithioindigo photoswitch was connected to the Hammett constants of substituents on the stilbene moiety. The speed of the reaction increases with raising electron donor strength of the substituents (decreasing Hammett constants), until at a certain point the FC state changes its electronic character due to their influence. As a result the isomerization speed peaks and its linear relationship with the Hammett constants changes its sign. Based on the relation found, the, up to this date fastest isomerizing hemithioindigo could be designed and synthesized. For the related thioindigo derivatives it was shown that the introduction of a hydroxy group on one moiety can open up an efficient decay channel for the excited state, which involves an ESIPT. This concept potentially could be used for other dyes and other compounds, too, as this fast relaxation pathway provides greatly enhanced photostability, because the proton easily recombines in the GS, which leads back to the reactant structure. Lastly, for the series furan, furfural and  $\beta$ -furfural the effect of the aldehyde substituent on the relaxation dynamics was investigated. Alongside uncovering an additional decay path and proposing a complete relaxation scheme for the two derivatives, the electronic structures of all three molecules is discussed in detail, also with respect to the

quantum chemical methods used. Special focus is given to one of the main  $S_1/S_0$  CoIns, which is explained within the two electron two orbital model used to predict the geometrical influence of the substituents on the considered CoIn. Altering the molecule, to tightly link the structural impact of the substituents to energetic consequences, for example via sterical hindrances, could pose yet another point of action to manipulate and tailor photorelaxation processes.

All in all, it is shown that rational design of molecules, despite the complications arising due to the numerous geometries a molecule can form, and the diverse electronic structures, which need to be considered, is more and more feasible, even for photoprocesses, which require the calculation of excited states and large regions on the PES, away from the FC point.

Finally ASRS, a novel spectroscopic detection scheme was presented, and spectra for the ring opening reaction of furan were simulated and analyzed. The method is a promising tool, to directly record the passing of a wavepacket through a CoIn. ASRS proved to be highly sensitive to the populated electronic states and to the actual region on the PES the molecules are located at. Even before put into praxis, much theoretical work can be done on trying to fade transitions in and out, as desired, by altering the ASRS pump and probe pulses, and formulating precise rules how diverse peak shapes and positions are to be interpreted in experimental spectra, where the underlying electronic processes are not known a priori.

# Appendix A

## NewtonX

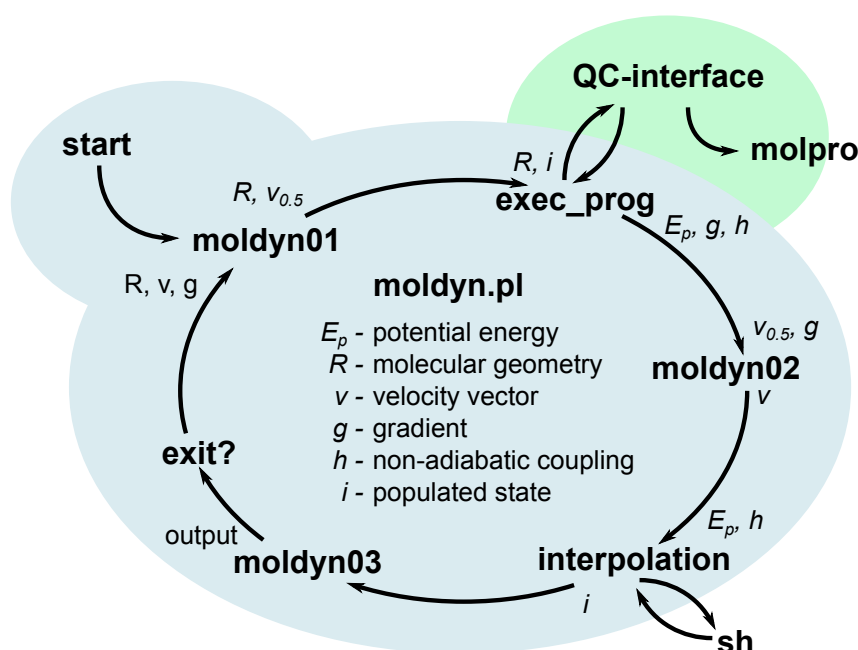


Figure A.1: Scheme of the main functions of `moldyn.pl`, the central script of NewtonX. The variables needed by a routine are noted before, the variables updated by the routine are noted behind it, in clockwise direction. At the start of the trajectory, the interface to the quantum chemistry package is called once, to compute energy and gradient of the starting structure. From here, `moldyn01` and `moldyn02` are responsible for the velocity-verlet algorithm, where the velocity is calculated in two steps. Before the execution of `moldyn02`, `exec_prog` calls the interface to update the energy, gradient and non-adiabatic coupling. After completing the step of the propagation of the nuclei, the electronic wavefunction is integrated by interpolating all values, updating the coefficients of the adiabatic states (see chap. 1.2.1), and using the fewest switches surface hopping routine in `sh`, to determine which state is populated. The output is then written by `moldyn03`.

NewtonX uses the Velocity-Verlet algorithm (formula B.3) to propagate the molecules within the on-the-fly dynamics. This is combined with non-adiabatic surface hopping (see chapter 1.2) and various other enhancements and features. NewtonX is written in a modular approach in Perl 5 and Fortran 90. The central Perl-script `moldyn.pl`, schematically depicted in fig. A.1, organizes the propagation of a single trajectory by calling a set of subroutines and programs which are in charge of specific subtasks within the algorithm. The communication between

external programs is realized by a set of files which store options and variables. This makes implementation of altered or new programs in principle easy.

In the following two sections, the features, added to NewtonX, mostly via the interface to Molpro, are presented chronologically, comments on the usage of Molpro (and Molcas) in NewtonX are given, and the structure of the interface is explained.

## A.1 Overview of the development and capabilities of the interface

In the process of the development of the interface, the code was completely rebuilt two times. The first version was adopted from Benjamin P. Fingerhut. It based on the interface to Gaussian03, provided by NewtonX 1.2, and was rewritten to allow ONIOM (CASSCF/HF) simulations for one specific molecule, combining Gaussian03 for the HF calculations and Molpro10 for the CASSCF calculations (see chapter 1.1). For the implementation of CASPT2 (see chapter 1.2), the interface was programmed from scratch, to be universal with respect to which molecules are computed. Within the process of refining the computation of the CASPT2 non adiabatic coupling, a second major reconstruction of the interface was undertaken. It was linked to NewtonX 1.4 and focused on allowing implementation of diverse additional features in an easy and clear way. The features below list the main capabilities of the interface. Minor options are given in the section A.2.

### CASSCF

CASSCF is the basic method for which the dynamics are implemented. For the non-adiabatic coupling usually the coupling vectors calculated by Molpro analytically should be used. For verification of the numerical calculation used in other methods, the numerical calculation of its projection onto the velocity vector (see chapter 1.2.1) is available, too.

### CASPT2 (RS2)

Non-adiabatic CASPT2 dynamics are available for the Rayleigh-Schrödinger perturbation theory (RS2) implementation of Molpro, using its analytic gradients and the calculation of the non-adiabatic coupling, implemented in the interface (chapter 1.2.1).

### CASPT2 (Molcas)

To be able to simulate molecular dynamics on CASPT2 level of theory even for larger molecules, one version of the interface was changed, to be able to use Molcas instead of Molpro. The Molcas CASPT2 is a faster version, comparable to RS2C of Molpro, but with the option to do multi-state calculations. It has no analytical gradients available, though, therefore the calculation of numerical gradients was added to the interface in a highly parallelized manner (see chapter A.2). To save computation time, the gradient is only calculated in forward direction. Although the implementation worked for ethylene, early trajectories tested on furan exhibited problems with the gradient and quickly violated the conservation of energy. In retrospect, this can most likely be attributed to the combination of the complicated electronic situation of furan at the FC point (chapter 2.3), where single reference CASPT2 might not be exact enough, combined with the gradient being calculated via two instead of three points. Further testing and verification is required here, nonetheless.

## Field effects on the nuclei motion

In an additional version, the interface was enhanced by Robert Siemering [58], to enable the inclusion of an electric field from a laser pulse, which then acts on the motion of the nuclei.

## Excitation by a laser field

The effect of the field on the hopping probability between the electronic states was included, by adding its interaction with the transition dipole moment into Tully's surface hopping algorithm, as suggested, e.g. by Tavernelli et al. [59]. Equation 1.4 becomes:

$$\dot{c}_i = - \sum_j c_j \left( \frac{i}{\hbar} H_{ij} + \dot{\mathbf{R}} \mathbf{h}_{ij} - \underline{\Delta E_{ij} \frac{A_0}{c\hbar^2} \epsilon_\lambda \cdot \mu_{ij} e^{-i\omega t}} \right), \quad (\text{A.1})$$

where  $\Delta E_{ij} = E_i - E_j$  and  $\epsilon_\lambda \cdot \mu_{ij}$  is the scalar product between the direction of the electric field of the laser and the transition dipole moment between the two states considered. The rest of the additional term (underlined) is the field strength at a given time  $t$ . Instead of calculating the latter for a continuous wave, as done in [59], we read the current field strength in each step from a file, to be able to describe laser pulses.

This part of the code is not yet implemented in the main fork of the program. Firstly some larger adjustments outside the interface were needed, and, more important, secondly we disabled the algorithm which checks whether hops between states are energetically allowed.

## ONIOM

After the calculations on the formation of the Dewar lesion were performed using the first version of the interface, the ONIOM routine was not directly added when rewriting it. This was later done by Matthias Roos, who now uses Molpro exclusively for the ONIOM routine.

## A.2 Comments on the usage and the source code of the interface and NewtonX

Using Molpro with NewtonX requires the usual steps of generating starting conditions via a previously performed frequency analysis and the files containing the options and parameters using the script *nxinp*. In the *general options* menu, Molpro (number 15) has to be set as quantum chemistry software. Two additional files have to be provided: In the *TRAJECTORIES* folder a file *opt* has to be placed, which contains information used by the queuing system established in our group, in the base directory *molpro.par* has to be provided, which contains all options specific to the interface. Formerly its configuration was included in the *non-adiabatic information* option of *nxinp*, but it didn't prove to be practicable and was not maintained. (An important side note for the reader setting up a set of trajectories - some versions of NewtonX are bugged and do not default to using random seeds for the surface hopping procedure. Run two short test trajectories, check whether the seed provided in *sh.out* either differs or is 1, which means a random seed is used in newer versions, and if not, set up the optional file *sh.inp*.) Options for the basic version of the interface, set in *Molpro.par* are provided in table A.1.

The template Molpro input *Molpro.inp*, which has to be provided in the *JOB\_NAD* folder, can be formatted relatively free. The Molpro-file containing the orbitals, "file,2", has to be named *Molpro.wfu*, however, and, although the actual geometry information can be skipped, as it will be overwritten by the interface, the curly brackets have to be supplied. The interface will generate appropriate *cpmcsf* and *force* commands for each step, whereas the general calculation containing the *multi* block has to be prepared by the user, to provide the maximal amount of

Table A.1: Options provided via the configuration file *Molpro.par*. The format is a simple line separated list of parameter name and value, separated by whitespace or “=”. The option *tdmxyz* in conjunction with *nstatdyn = 0* in the *control.dyn* file will perform an extra calculation at the starting structure of the trajectory and set the initial state to the state with the largest absolute dot product between its transition dipole moment with the ground state and the provided vector.

nopus	<number>	number of cpus to use
mode		quantum chemical method used
	cas	CASSCF
	srpt2	single-reference CASPT2
	mrpt2	multi-reference CASPT2
nacm		method to compute the non-adiabatic coupling
	an	analytical vectors from Molpro
	dr	numerical (see chapter 1.2)
nacs		non-adiabatic couplings to compute
	a	all (with a maximum of four - see below)
	n	none (adiabatic dynamics)
	<number>	maximum energetic gap between considered states
tdm	1	read and print transition dipole moments each step
cp		when to store output and molden files
	a	always
	n	never
	<number>	each n'th step
	r	not at the displaced geometry (in case of “nacm = dr”)
tdmxyz	<x y z>	in conjunction with other options; see the caption

flexibility. One copy of *Molpro.wfu*, preferably from the FC point, should be provided, to serve as a starting guess for the CASSCF wave function.

Together with the interface a set of smaller scripts were programmed, which primarily serve to perform the dynamics at the group's computing cluster, and to help with basic analysis.

*tsub* is used to submit trajectories.

*en* plots the energetic course of a single trajectory.

*dyn* is used together with the program *gmolden* to visualize the motion of the molecules.

*rep* can be used to check aborted trajectories and assist in fixing them.

*sven.pm* is a perl-library containing auxiliary subroutines.

The basic structure of the interface, *run-molpro.pl*, is rather simple. After the definition of various global variables, the main program calls *readctd()* to read NewtonX specific variables and *what\_to\_do()* to read *molpro.par* and determine its tasks. *modify\_input()* prepares the Molpro input and *run\_molpro()* executes Molpro, *read\_molprolog()* parses the output and *write\_nx()* writes the files read by NewtonX. This is a bit obstructed as *run\_molpro()* and *read\_molprolog()* are executed in a loop which checks for errors in the execution of Molpro and automatically restarts the calculation in attempt to fix certain ones.

In case of “nacm = dr” Molpro is executed a second time at the displaced geometry. The *molpro.inp* which is used as template therefor is prepared by placing “!r!” and “!dr!” in front of lines which should only be executed at one of the geometries.

At the end of the program code, a class named *Matrix* is defined, which is used for variables like geometries, gradients and couplings.

After reading *molpro.par*, the subroutine *what\_to\_do()* determines between which states the non-adiabatic coupling has to be calculated. As Molpro2012 computes only a maximum of five *cpmcsf* orders per *multi* block, usually a maximum of four non-adiabatic coupling vectors will be calculated. In the case that more than this number are requested, the four energetically

closest to the occupied state are included, the rest is left out.

The subroutine *run\_molpro()* which executes Molpro contains the path to Molpro and potentially sets environment variables. It has to be adjusted, if the interface should be used elsewhere.

*read\_molpro\_log()* defines the variable *parser*, a hash, which contains the code to read each variable on different levels of theory in separate entries. Depending on which are needed, the array *extractor* is built and used to finally extract the information in a rather small *while*-loop further into the subroutine. In the parser for the non-adiabatic coupling information of the multi-reference CASPT2, in the latest version a small external program written by Artur Nenov is called, which diagonalizes the effective Hamiltonian extracted by the parser. This is done in the output of Molpro, too, but the phase information between the states seems to not be reliable.

The subroutines *calc\_nac()* and *rootflip()* are responsible for the calculation of the non-adiabatic coupling when the numeric treatment is selected, and in case of CASPT2 dynamics, to keep track of the order of states of CASPT2 compared to CASSCF. In case of rootflipping, i.e. the order of the CASPT2 states differs from their respective CASSCF reference states, the gradient of the respective state has to be recalculated, when single-reference CASPT2 is used. For Molpro2010, regardless whether single- or multi-reference is used, the order of the states of the transition dipole moments has to be adjusted. For Molpro2012 and Molpro2015 the output is not consistent between all CASPT2 versions and options (especially the extended multi-state (XMS) option), and the ordering of the transition dipole moments has to be checked.

The interface can be executed with parameters, which is done at two stages of the execution of NewtonX: A subroutine called *check\_initial\_state* was added to the main program *molodyn.pl*, which, if “nstatdyn = 0” is set in *control.dyn*, calls the interface once, to compute the transition dipole moment at the starting geometry, and then determines the electronic state the trajectory is started from. Additionally the source code of *sh.f90* and *sh\_mod.f90* was changed, to allow the surface hopping routine to call the interface, in case of a hopping event to a state which does not have its gradient computed (which usually is the case for all but the currently populated state). In both cases the interface will perform only the required tasks to retrieve the needed information.

The *run-molcas.pl* routine, which was written to perform CASPT2 dynamics with Molcas, contains the subroutine *calc\_grad()*, which numerically calculates the gradient of the molecule. To do this, in *modify\_input()* the whole set of inputs at displaced geometries is prepared and placed in a folder accessible from all nodes of the cluster. *run-molcas.pl* is programmed to successively initiate all computations if necessary, but will also check for outputs. This means, that the Molcas jobs can be performed externally, too. A script called *helper* was set up, which can be submitted to the queue multiple times on independent nodes, and is supposed to run alongside a couple of trajectories, to conduct the computation of the gradients. This can highly parallelize this step.





# Appendix B

## Formulas

**Newtons equation of motion** describes the acceleration in terms of the second derivative of the coordinates  $\mathbf{R}$  of time, acting on a particle with mass  $m$  in presence of the energy gradient  $\nabla_{\mathbf{R}}E$ :

$$m\ddot{\mathbf{R}} = -\nabla_{\mathbf{R}}E . \quad (\text{B.1})$$

The **time-independent electronic Schrödinger equation** obtains the electronic energy  $E$  of a system by applying the electronic Hamilton operator  $\hat{H}$  to the electronic wavefunction  $\Psi$ , which depends on the electronic coordinates  $\mathbf{r}$  and parametrically on the coordinates of the nuclei  $\mathbf{R}$ .  $\hat{H}$  hereby consists of the operator for the kinetic energy of the electrons  $\hat{T}_e$  and the potential operators  $\hat{V}$  which describe the electron-electron repulsion, the attraction of the nuclei on the electrons, as well as the repulsion between the nuclei. (Whether the last is included, is subject to definition.)

$$\begin{aligned} \hat{H}\Psi(\mathbf{r}; \bar{\mathbf{R}}) &= E\Psi(\mathbf{r}; \bar{\mathbf{R}}) , \\ \hat{H} &= \hat{T}_e + \hat{V}_{ee} + \hat{V}_{en} + \hat{V}_{nn} . \end{aligned} \quad (\text{B.2})$$

The **Velocity-Verlet algorithm** integrates Newtons equation of motion, to evolve the coordinates  $\mathbf{R}$  and the velocity  $\mathbf{v}$  of the nuclei using a time-dependent gradient  $\mathbf{g}$  along discrete time intervals  $\Delta t$ .

$$\begin{aligned} \mathbf{R}(t + \Delta t) &= \mathbf{R}(t) + \mathbf{v}(t)\Delta t + \frac{\mathbf{g}(t)}{2} (\Delta t)^2 , \\ \mathbf{v}(t + \Delta t) &= \mathbf{v}(t) + \frac{\mathbf{g}(t) + \mathbf{g}(t + \Delta t)}{2} \Delta t . \end{aligned} \quad (\text{B.3})$$



# List of abbreviations

**AS** active space

**ASRS** attosecond stimulated X-ray Raman spectroscopy

**CASSCF** complete active space self consistent field

**CCSD** coupled cluster singles and doubles

**CoIn** conical intersection

**DFT** density functional theory

**DNA** deoxyribonucleic acid

**ESIPT** excited state intramolecular proton transfer

**FC** Franck-Condon

**GS** ground state

**HF** Hartree-Fock

**HOMO** highest occupied molecular orbital

**IPEA** ionisation energy electron affinity

**MRCI** multi-reference configuration interaction

**MS** multi-state

**ONIOM** our own n-layered integrated molecular orbital and molecular mechanics

**PES** potential energy surface

**CASPT2** complete active space second-order perturbation theory

**RS2** Rayleigh-Schrödinger perturbation theory

**SA** state average

**SS** single-state

**UV** ultra violet

**XMS** extended multi-state



# Bibliography

- [1] M. Barbatti, A. J. A. Aquino, J. J. Szymczak, D. Nachtigallová, P. Hobza and H. Lischka, *Proc. Natl. Acad. Sci. USA* **107**, 21453 (2010).
- [2] C. E. Crespo-Hernández, B. Cohen, P. M. Hare and B. Kohler, *Chem. Rev.* **104**, 1977 (2004).
- [3] G. Wald, *Science* **162**, 230 (1968).
- [4] R. Croce and H. van Amerongen, *Photosynth. Res.* **116**, 153 (2013).
- [5] H. van Amerongen and R. Croce, *Photosynth. Res.* **116**, 251 (2013).
- [6] M. Dittmann, F. F. Graupner, B. Maerz, S. Oesterling, R. de Vivie-Riedle, W. Zinth, M. Engelhard and W. Lüttke, *Angew. Chem. int. Ed.* **53**, 591 (2014).
- [7] S. Kawata and Y. Kawata, *Chem. Rev.* **100**, 1777 (2000).
- [8] Y. Yokoyama, *Chem. Rev.* **100**, 1717 (2000).
- [9] S. B. Darling and F. You, *RSC Adv.* **3**, 17633 (2013).
- [10] L. Lu, T. Zheng, Q. Wu, A. M. Schneider, D. Zhao and L. Yu, *Chem. Rev.* **115**, 12666 (2015).
- [11] Q. An, F. Zhang, J. Zhang, W. Tang, Z. Deng and B. Hu, *Energy Environ. Sci.* **9**, 281 (2016).
- [12] G. A. Worth and L. S. Cederbaum, *Annu. Rev. Phys. Chem.* **55**, 127 (2004).
- [13] W. Domcke, D. R. Yarkony and H. Köppel, *Conical Intersections; Electronic Structure, Dynamics and Spectroscopy*, vol. 15 of *Advanced Series in Physical Chemistry*, World Scientific (2004).
- [14] M. Barbatti, G. Granucci, M. Ruckebauer, F. Plasser, R. Crespo-Otero, J. Pittner, M. Persico and H. Lischka, *NEWTON-X: a package for Newtonian dynamics close to the crossing seam, version 1.4* (2014), <http://www.newtonx.org/>.
- [15] H.-J. Werner, P. J. Knowles, G. Knizia, F. R. Manby, M. Schütz, P. Celani, T. Korona, R. Lindh, A. Mitrushenkov, G. Rauhut, K. R. Shamasundar, T. B. Adler, R. D. Amos, A. Bernhardsson, A. Berning, D. L. Cooper, M. J. O. Deegan, A. J. Dobbyn, F. Eckert, E. Goll, C. Hampel, A. Hesselmann, G. Hetzer, T. Hrenar, G. Jansen, C. Köppl, Y. Liu, A. W. Lloyd, R. A. Mata, A. J. May, S. J. McNicholas, W. Meyer, M. E. Mura, A. Nicklass, D. P. O'Neill, P. Palmieri, D. Peng, K. Pflüger, R. Pitzer, M. Reiher, T. Shiozaki, H. Stoll, A. J. Stone, R. Tarroni, T. Thorsteinsson and M. Wang, *MOLPRO, version 2012.1, a package of ab initio programs* (2012), see <http://www.molpro.net/>.

- [16] M. Barbatti, *WIREs: Comp. Mol. Sci.* **1**, 620 (2011).
- [17] S. Dapprich, I. Komáromi, K. S. Byun, K. Morokuma and M. J. Frisch, *Mol. Struct. (Theochem)* **462**, 1 (1999).
- [18] T. Vreven, K. S. Byun, I. Komáromi, S. Dapprich, J. A. M. Jr., K. Morokuma and M. J. Frisch, *J. Chem. Theo. and Comp.* **2**, 815 (2006).
- [19] M. ta Araújo, B. Lasorne, A. L. M. aes, M. J. Bearpark and M. A. Robb, *J. Phys. Chem. A* **114**, 12016 (2010).
- [20] A. Hofmann and R. de Vivie-Riedle, *J. Chem. Phys.* **112**, 5054 (2000).
- [21] D. Keefer, S. Thallmair, S. Matsika and R. de Vivie-Riedle, *J. Am. Chem. Soc.* **139**, 5061 (2017).
- [22] S. Thallmair, M. Kowalewski, J. P. P. Zauleck, M. K. Roos and R. de Vivie-Riedle, *J. Phys. Chem. Lett.* **5**, 3480 (2014).
- [23] E. Wigner, *Phys. Rev.* **40**, 749 (1932).
- [24] M. Barbatti, A. J. A. Aquino and H. Lischka, *Phys. Chem. Chem. Phys.* **12**, 4959 (2010).
- [25] S. Hammes-Schiffer and J. C. Tully, *J. Chem. Phys.* **101**, 6 (1994).
- [26] M. J. Frisch, G. W. Trucks, H. B. Schlegel, G. E. Scuseria, M. A. Robb, J. R. Cheeseman, G. Scalmani, V. Barone, G. A. Petersson, H. Nakatsuji, X. Li, M. Caricato, A. Marenich, J. Bloino, B. G. Janesko, R. Gomperts, B. Mennucci, H. P. Hratchian, J. V. Ortiz, A. F. Izmaylov, J. L. Sonnenberg, D. Williams-Young, F. Ding, F. Lipparini, F. Egidi, J. Goings, B. Peng, A. Petrone, T. Henderson, D. Ranasinghe, V. G. Zakrzewski, J. Gao, N. Rega, G. Zheng, W. Liang, M. Hada, M. Ehara, K. Toyota, R. Fukuda, J. Hasegawa, M. Ishida, T. Nakajima, Y. Honda, O. Kitao, H. Nakai, T. Vreven, K. Throssell, J. A. Montgomery, Jr., J. E. Peralta, F. Ogliaro, M. Bearpark, J. J. Heyd, E. Brothers, K. N. Kudin, V. N. Staroverov, T. Keith, R. Kobayashi, J. Normand, K. Raghavachari, A. Rendell, J. C. Burant, S. S. Iyengar, J. Tomasi, M. Cossi, J. M. Millam, M. Klene, C. Adamo, R. Cammi, J. W. Ochterski, R. L. Martin, K. Morokuma, O. Farkas, J. B. Foresman and D. J. Fox, *Gaussian09 Revision D.01*, Gaussian Inc. Wallingford CT 2016.
- [27] K. Haiser, B. P. Fingerhut, K. Heil, A. Glas, T. T. Herzog, B. M. Pilles, W. J. Schreier, W. Zinth, R. de Vivie-Riedle and T. Carell, *Angew. Chem. Int. Ed.* **51**, 408 (2012).
- [28] B. P. Fingerhut, K. Heil, E. Kaya, S. Oesterling, R. de Vivie-Riedle, and T. Carell, *Chem. Sci.* **3**, 1794 (2012).
- [29] H. Tao, B. G. Levine and T. J. Martínez, *J. Phys. Chem. A* **113**, 13656 (2009).
- [30] M. Barbatti, J. Paier and H. Lischka, *JCP* **121**, 11614 (2004).
- [31] L. E. McMurchie and E. R. Davidson, *JCP* **66**, 2959 (1977).
- [32] M. M. Luis Serrano-Andres, I. Nebot-Gil, R. Lindh and B. O. Roos, *JCP* **98**, 3151 (1993).
- [33] F. Aquilante, J. Autschbach, R. K. Carlson, L. F. Chibotaru, M. G. Delcey, L. D. Vico, I. F. Galván, N. Ferré, L. M. Frutos, L. Gagliardi, M. Garavelli, A. Giussani, C. E. Hoyer, G. L. Manni, H. Lischka, D. Ma, P. A. Malmqvist, T. Müller, A. Nenov, M. Olivucci, T. B. Pedersen, D. Peng, F. Plasser, B. Pritchard, M. Reiher, I. Rivalta, I. Schapiro, J. Segarra-Martí, M. Stenrup, D. G. Truhlar, L. Ungur, A. Valentini, S. Vancoillie, V. Veryazov, V. P. Vysotskiy, O. Weingart, F. Zapata and R. Lindh, *J. Comp. Chem.* **37**, 506 (2016).

- [34] K. Andersson, P. Malmqvist and B. O. Roos, *J. Chem. Phys.* **96**, 1218 (1992).
- [35] H.-J. Werner, *Mol. Phys.* **89**, 645 (1996).
- [36] L. Serrano-Andrés, M. Merchán, I. Nebot-Gil, R. Lindh and B. O. Roos, *J. Chem. Phys.* **98**, 3151 (1993).
- [37] D. Feller, *J. Comp. Chem.* **17(13)**, 1571 (1996).
- [38] K. L. Schuchardt, B. T. Didier, T. Elsethagen, L. Sun, V. Gurumoorth, J. Chase, J. Li and T. L. Windus, *J. Chem. Inf. Model.* **47(3)**, 1045 (2007).
- [39] *ANO-RCC basis set error*, [www.molcas.org/ANO/indexC.html](http://www.molcas.org/ANO/indexC.html), Accessed: 10.04.2017.
- [40] G. Ghigo, B. O. Roos and P. Malmqvist, *Chem. Phys. Lett.* **396**, 142 (2004).
- [41] P. G. Wilkinson and H. L. Johnston, *J. Chem. Phys.* **18**, 190 (1950).
- [42] P. Farmanara, V. Stert and W. Radloff, *Chem. Phys. Lett.* **288**, 518 (1998).
- [43] K. Kosma, S. A. Trushin, W. Fuss and W. E. Schmid, *J. Phys. Chem. A* **112**, 7514 (2008).
- [44] V. Stert, H. Lippert, H.-H. Ritze and W. Radloff, *Chem. Phys. Lett.* **388**, 144 (2004).
- [45] Y. Zhao, N. E. Schultz and D. G. Truhlar, *J. Chem. Theory and Comput.* **2**, 364 (2006).
- [46] H. Tao, T. K. Allison, T. W. Wright, A. M. Stooke, C. Khurmi, J. van Tilborg, Y. Liu, R. W. Falcone, A. Belkacem and T. J. Martínéz, *J. Chem. Phys.* **134**, 244306 (2011).
- [47] Y. Furmansky, H. Sasson, P. Liddell, D. Gust, N. Ashkenasy and I. Visoly-Fisher, *J. Mater. Chem.* **22**, 20334 (2012).
- [48] C. E. Crespo-Hernández, L. Martínez-Fernández, C. Rauer, C. Reichardt, S. Mai, M. Pollum, P. Marquetand, L. González and I. Corral, *J. Am. Chem. Soc.* **137**, 4368 (2015).
- [49] S. Olsen, *J. Phys. Chem. A* **120**, 10245 (2016).
- [50] C. Maglione, A. Carella, R. Centore, S. Fusco, A. Velardo, A. Peluso, D. Colonna and A. D. Carlo, *J. Photoch. Photobio. A: Chem.* **321**, 79 (2016).
- [51] T. Cordes, D. Weinrich, S. Kempa, K. Riesselmann, S. Herre, C. Hoppmann, K. Rck-Braun and W. Zinth, *Chem. Phys. Lett.* **428**, 167 (2006).
- [52] S. Kitzig, M. Thilemann, T. Cordes and K. Rck-Braun, *ChemPhysChem* **17**, 1252 (2016).
- [53] S. Wiedbrauk and H. Dube, *Tetrahedron Letters* **56**, 4266 (2015).
- [54] I. Iwakura, A. Yabushita and T. Kobayashi, *Chem. Phys. Lett.* **484**, 354 (2010).
- [55] A. Nenov and R. de Vivie-Riedle, *J. Chem. Phys.* **135**, 034304 (2011).
- [56] A. Nenov and R. de Vivie-Riedle, *J. Chem. Phys.* **137**, 074101 (2012).
- [57] A. A. Granovsky, *Firefly version 8*, <http://classic.chem.msu.su/gran/firefly/index.html>, Accessed: 24.04.2017.
- [58] E. Wells, C. E. Rallis, M. Zohrabi, R. Siemering, B. Jochim, P. R. Andrews, U. Ablikim, B. Gaire, S. De, K. D. Carnes, B. Bergues, R. de Vivie-Riedle, M. F. Kling and I. Ben-Itzhak, *Nt. Commun.* **4**, 2895 (2013).
- [59] I. Tavernelli, B. F. E. Curchod and U. Rothlisberger, *Phys. Rev. A* **81**, 052508 (2010).





# Danksagung

In erster Linie möchte ich hier Frau de Vivie-Riedle und dem Rest des Arbeitskreises danken. Es war eine schöne Zeit, und Patrick und ich haben vor ein paar Monaten schon etwas schwermütig festgestellt, dass man leider wohl nicht erwarten kann, im Beruf selbstverständlich wieder in eine Gruppe zu geraten, in der ein ähnliches, größtenteils fröhliches und freundschaftliches Miteinander herrscht. In meinen Augen ist das das wichtigere, zusätzlich (und dafür ist es wohl auch Grundlage) ist es in Bezug auf die Arbeit dann auch noch so, dass man bei fast jedem Problem jemanden finden kann, der bereitwillig mitüberlegt und -diskutiert (manchmal gleich in ganzen Trauben, die sich nach dem Mittagessen um einen Rechner versammeln), was mehr als einmal hilfreich war. Neben Frau de Vivie-Riedle also auch den Betreuern meiner Bachelor- und Masterarbeiten, Artur und Benni (auf die letzteres für mich natürlich im Besonderen zugetroffen hat, auch lange nach den jeweiligen Arbeiten), den anderen etwas älteren, Markus (bezogen auf die Administration auch soetwas wie mein Betreuer) und Philipp, Patrick, dem Thali (mein alter Klassenkamerad (in der Grundschule waren es noch Parallelklassen, oder?), der mir im Gegenzug dafür, dass ich ihm durchs Computerpraktikum geholfen hab, schon unser gesamtes Studium mit seinen Unterlagen und bei allen möglichen organisatorischen Dingen viel Arbeit abgenommen hat ;), meinen eigenen Praktikanten, Daniel und Flo, die inzwischen bei uns sind, sowie Claudia, Leonhard, Marius, Maurus und Bastien, und natürlich den ganzen übrigen, Robert, Matthias, Julius, Thomas, Franziska und Martin.

Ein paar andere Praktikanten und alljährliche Weihnachtsfeierbesucher gehören eigentlich auch dazu, stellvertretend nenn ich mal den Travis, der mir an zwei, drei Stellen beim Übersetzen geholfen hat.

Bei meinen Kooperationspartnern sind vor allem Herr Zinth und Henry Dube hervorzuheben, mit denen wir in verschiedenen Kombinationen v.a. das HTI in allen erdenklichen Aspekten über Stunden diskutiert haben. Aber auch allen anderen, stellvertretend Herrn Carell, Sandra, Franziska, Benjamin, Oliver und Weijie möchte ich für die gute Zusammenarbeit danken.

Ich bin sehr dankbar für meine Familie und Freunde, aber das hier in wirklich passender Weise auszuführen ist komplizierter als manch anderes, was weiter vorne steht, und am Ende wäre das wohl auch die falsche Stelle. Ich belass es also mal bei dem.